Ask Halse

Trawl interference loads for offshore power cables

Master's thesis in Marine Technology

Supervisor: Prof. Svein Sævik

July 2020

Master's thesis

NTNU
Norwegian University of Science and Technology
Faculty of Engineering
Department of Marine Technology

NTNU
Norwegian University of
Science and Technology

Ask Halse

Trawl interference loads for offshore power cables

Master's thesis in Marine Technology
Supervisor: Prof. Svein Sævik
July 2020

Norwegian University of Science and Technology
Faculty of Engineering
Department of Marine Technology

NTNU

Kunnskap for en bedre verden

NTNU Trondheim
Norwegian University of Science and Technology *Faculty of Engineering*
Department of Marine Technology

THESIS WORK SPRING 2020

for

Stud. Tech. Ask Ivar Halse

Trawl interference loads for offshore power cables

Trållaster på undersjøiske kraftkabler

Floating wind farms is a key enabling technology for future renewable energy. This will include development of power cable networks resting on the seabed to collect and export the power to the market. In the Norwegian Seas there is a lot of fishing activity including use of trawl boards and clump weights that are pulled along the seabed. A standard way of protecting the cables is by means of trenching and backfilling or rock dumping. However, this will cause a significant cost increase. For pipelines that are left exposed on the seabed, the design requirements includes consideration of trawl loads, which are normally based on DNVGL-RP-F111. This RP is based on model tests of steel pipelines which have a bending stiffness several order of magnitudes larger than relevant for cables. Hence, the task in this thesis is to investigate the realistic load and response for different trawl boards/clump weights interacting with a cable versus the load and response established from applying DNVGL-RP-F111. The thesis work will be based on continuing the project work carried out during Fall 2019 and is to be carried out as follows:

1. Literature study related to methods for global response analysis with focus on trawl/pipeline interaction including, relevant rules, standards and RPs, analytical models for cable capacity and soil models.
2. Learn the FE tool SIMLA.
3. Define case scenarios including mechanical properties, geometry and environmental conditions.
4. Establish SIMLA models based on DNVGL-RP-F111 and perform response analysis
5. Establish models for the trawl board and/or clump weight and seabed intervention profile in SIMLA and perform response analysis
6. Compare the results between the two approaches and give recommendations
7. Conclusions and recommendations for further work.

The work scope may prove to be larger than initially anticipated. Subject to approval from the supervisors, topics may be deleted from the list above or reduced in extent.

In the thesis report, the candidate shall present her personal contribution to the resolution of problems within the scope of the thesis work

Theories and conclusions should be based on mathematical derivations and/or logic reasoning identifying the various steps in the deduction.

The candidate should utilise the existing possibilities for obtaining relevant literature.

Thesis report format
The thesis report should be organised in a rational manner to give a clear exposition of results, assessments, and conclusions. The text should be brief and to the point, with a clear language. Telegraphic language should be avoided.

The report shall contain the following elements: A text defining the scope, preface, list of contents, summary, main body of thesis, conclusions with recommendations for further work, list of symbols and acronyms, references and (optional) appendices. All figures, tables and equations shall be numerated.

The supervisors may require that the candidate, in an early stage of the work, presents a written plan for the completion of the work.

The original contribution of the candidate and material taken from other sources shall be clearly defined. Work from other sources shall be properly referenced using an acknowledged referencing system.

The report shall be submitted in electronic format (.pdf):
- Signed by the candidate
- The text defining the scope shall be included (this document)
- Drawings and/or computer models that are not suited to be part of the report in terms of appendices shall be provided on separate (.zip) files.

Ownership
NTNU has according to the present rules the ownership of the thesis reports. Any use of the report has to be approved by NTNU (or external partner when this applies). The department has the right to use the report as if the work was carried out by a NTNU employee, if nothing else has been agreed in advance.

Thesis supervisors:

Prof. Svein Sævik, NTNU, Dr. Erik Levold, Equinor and Dr. Vegard Longva, SINTEF Ocean

Deadline: June 10th, 2020

Trondheim, January 7, 2020

Svein Sævik

Preface

This report present the work conducted in my master thesis in Marine Technology with specialisation within Marine Structures. The research were preformed at the Department of Marine Technology, NTNU, during the spring semester 2020 and is a continuation of the work carried out in my specialization project during the fall semester 2019.

The main objective of the thesis were to determine trawl loads on offshore power cables with focus on the clump weight trawl gear. The scope has been altered somewhat over the course of the work period to finally include a comparison with DNVGL-RP-F111, design check and sensitivity studies of hit angles, relative penetration between the clump weight and cable, and pre-tension in the cable.

Along with this report there is included SIMLA input files used for the simulations, script that is used to produce the input files, and scripts used for post-processing and plotting.

I would like to thank my Supervisor Svein Sævik for excellent guidance and help with understanding the SIMLA program. In addition, I would like to thank Vegard Longva for for providing me with his personal codes and using several hours going through them with me. Furthermore, I would like to thank Erik Levold in Equinor for providing me with cable specifications and advice on choosing parameter studies. Finally, an acknowledgement goes out to Sintef Ocean for providing license to SIMLA

Ask Halse
Trondheim, June 2020

Abstract

The objective of this thesis was to investigate trawling loads from the interaction between roller clump weights and subsea power cables with focus on the pull-over phase. In addition, a sensitivity study of the effect of hit angle, relative penetration between the clump weight roller and the pre-tension in the cable were to be conducted. Finally, the load levels were to be compared to DNVGL-RP-F111 and further checked against design limits for relevant rules.

All simulations were preformed in the SIMLA software, a special purpose on-linear finite element program developed for slender structures. A brief description of the applied finite element formulations and solution procedures is included in a separate chapter. Furthermore, background containing build up and mechanical properties of subsea power cables, trawling gear concepts, relevant rules and regulations as well as previous research on trawl gear interference loads is included.

The clump weight model were based on a physical model previously used by Sintef Ocean. The clump weight model were accelerated to a velocity of 2.4 m/s before the interaction occurred, and had a dry mass of 5925 kg. In order to allow for a sliding motion in the model, the translation constraints of the trawl board nodes transverse to the trawl direction were released T = 50.0 s. As a result, the trawl boards were dragged in towards the clump weight closing the trawl net. The interaction forces are therefore likely to be on the conservative side.

The results showed that the DNVGL-RP-F111 overpredicted the maximum horizontal pull-over with up to four times the force that was found in the SIMLA model. The duration of the interaction was also found to be significantly shorter than predicted. DNVGL-RP-F111 can therefore not be used to predict trawl loads from the interaction between subsea power cables and clump weights. The finding were expected as the offshore power cables are flexible where steel pipelines are rigid.

Sensitivity of pull-over force, axial force, maximum global displacement and maximum curvature were studied for hit angles 90°, 80°, 40°, and 20°. Where 90° correspond to a perpendicular angle between the trawl direction and the power direction and 0° correspond to a parallel one. The clump weight started to slide along the cable or hit angles 40° and 20°, and the results indicated that the duration of the sliding motion will increase with a reduced hit angle. In combination with a 63 mm relative penetration, the largest maximum pull-over load, maximum axial force, maximum global displacement and maximum curvature occurred for a perpendicular hit angle. In the vertical direction, the maximum pull-over force were found to not be significant affected by the hit angle. The maximum horizontal pull-over force and maximum axial pull over force were at its lowest for moderate hit angles, while the maximum displacement and maximum curvature were found to decrease with the hit angle.

The case with a 80° hit angle had a considerable lower pull-over time compared to the other cases. As a consequence, the quick tilting motion occurring after contact between the clump weight and the power cable had been established led to convergence problems. The time step had to be divided by ten and the convergence radius increased from fra 10^{-8} to $5 \cdot 10^{-4}$ drastically reducing the accuracy. As a countermeasure, amount of steps used in pull-over force averaging were raised from 100 to 500 for this hit angle. Nevertheless, large spikes could be observed in some of the pull-over history plots. The maximums found from these plots were therefore not taken into consideration when the sensitivity studies were preformed.

The sensitivity study of relative penetration were preformed with values of 13 mm, 63 mm and 113 mm. Generally it were found that the maximum pull-over force, maximum axial force, maximum global displacement and maximum curvature increased with the relative penetration. The effect varied greatly with the hit angle, and the relative penetration were found to be especially important for the 20° hit angle.

The clump weight were not able to cross the power cable when a 20° hit angle and a 113 mm relative penetration were combined. The interaction ended up in a continuous sliding motion, which lasted to the end of the simulation up, 40 seconds after contact between the clump weight and the cable were established. While sliding, the horizontal pull-over force, axial force, displacement and curvature were gradually increasing, at some point surpassing the maximum values found for a perpendicular case. However, due to the long duration of the simulation, the trawl net configuration was significantly deformed and the clump weight were able to slide out of the cable section with a refined mesh size. The validity of the results for his case are therefore questionable.

Finally, the simulation results demonstrated that the pre-tension had a minor to none effect on the response. By reducing the pre-tension from 10 kN to 1 kN it were found that the maximum pull-over force and maximum axial force had a slight decrease while the maximum displacement and maximum curvature had a slight increase.

The design limits, used to check the load levels up against capacity, were based on rules for flexible risers. Comparing with the design limit, the maximum axial forces and maximum curvatures for the most critical case combination were found to be 9.5 % and 80 % of the design limit respectively. The load levels resulting from the interaction with the clump weight were hence found to be within safe bounds. It is nevertheless probable that the cable have to be protected as the continuous sliding motion that can occur for small hit angle may threaten the integrity of the outer sheath.

Sammendrag

Målet med denne avhandlingen var å undersøke hvilke trållaster som oppstår som en følge av interaksjon mellom klumpvekter og offshore kraftkabler med fokus på pull-over stadiet. I tillegg skulle sensitivitet av treffvinkel, relativ penetrasjon mellom klumpvekt og kabel samt førspenning i kabelen undersøkes. Til slutt skulle pull-overlastene sammenlignes med DNVGL-RP-F111 og responsen til kabelen sjekkes opp mot relecante regelverk.

Alle simulasjoner ble gjort det ikke-lineære finite element programmet SIMLA, som er skreddersydd for slanke strukturer. Finite element formulasjonen og løsningsprosedyrer for programmet er beskrevet i et separat kapittel. Videre er også bakgrunn for undersjøiske kabler, teori om trålutsyr, relevante regler og regulasjoner samt tidligere forskning på trållaster inkludert.

Klumpvektsmodellen er basert på en fysisk modell som tidligere har blitt brukt av Sintef Ocean. Klumpvekten blir i analysen aksellerert opp til en hastighet på 2.4 m/s før interaksjonen intreffer og har en tørr vekt på 5924 kg. Trålbord-nodene er holdt fast på tvers av trålretningen mellom start av analysen til T = 50.0 s. Etter dette ble frihetsgraden sluppet opp for å muiliggjøre glidning mellom klumpvekt og kabel. Dette førte til at sveipelinene lukket seg og trålbordene ble trukket innover mot klumpvekten. Interaksjonskreftene vil derfor sannsynligvis være på den konservative siden

Resultatene viste at DNVGL-RP-F111 predikerte en maksimal horisontal pull-over last som var opp til fire ganger den som ble funnet i SIMLA modellen. Varigheten på interaksjonen var også betydelig lengre enn den faktiske varigheten funnet i simulasjonene. Man kan derfor konkludere med at DNVGL-RP-F111 ikke kan brukes til å estimere laster fra interaksjon mellom klumpvekter og kraftkabler. Funnet var ikke overraskende da bøyestivheten til kraftkabler er mye lavere en den for til stålrør.

Sensitivitet av maksimal pull-overkraft, maksimal aksialkraft, maksimum kurvatur og maksimum global forflyttning av kabelen for treffvinkler 90°, 80°, 40° og 20°. Her tilsvarer 90° en perpendikulær treffvinkel og 0° tilsvarer en paralell treffvinkel. For treffvinkelene 40° og 20° startet klumpvekten å skli langs kabelen etter kontakt var opprettet, og varigheten så ut til å øke når treffvinkelen ble redusert. I kombinasjon med en relativ penetrasjon på 63 mm ble den maksimale pull-over lasten, maksimale aksialkraften, maksimale kurvaturen og den maksimale globale forflyttningen størst ved en perpendikulær treffvinkel. Den maksimale vertikale pull-over kraften viste seg å ikke bli betydelig påvirket av treffvinkelen. Resultatene viste også at den maksimale horisontale pull-over kraften og den maksimale aksialkraften var lavest for moderate treffvinkler, og den maksimale globale forflyttningen var høyere for lavere treffvinkeler.

Konfigurasjonene med 80° treffvinkel hadde en betydelig kortere pull-over varighet enn for de andre treffvinklene. Dette førte til at hellingsvinkelen på klumpvekten endret seg raskt under interaksjonen og det oppstod konvergensproblemer. Tidssteget måtte deles på ti og konvergensradiusen måtte økes fra 10^{-8} til $5 \cdot 10^{-4}$, hvilket betydde en drastisk reduksjon i løsningspåliteligheten. For å motvirke store fluktuasjoner i pull-over lasten, ble gjennomsnittsverdien tatt over 500 steg i stedet for over 100 steg for bruk i plottings. Likevel var det mulig å observere store fluktuasjoner i pull-over kraften for disse simulasjonene. De maximale pull-over kreften fra lokale topper i konfigurasjoner med 80° treffvinkel ble derfor ikke tatt med i betraktningen når sensitivitetsstudiene ble utført.

Sensitivitetsstudiet for relative penetetrasjoner ble gjort for verdiene: 13 mm, 63 mm og 113 mm. Resultatene viste at maksimum pull-over kraft, maksimal aksialkraft, maksimal kurvatur og maksimal global forflyttning øker når den relative penetrasjonen øker. Størrelsesorden på effekten var i stor grad påvirket av treffvinkelen, spesielt for for lave treffvinkler.

Klumpvekten klarte ikke å krysse kraftkabelen når en treffvinkel på 20° ble kobinert med en relativ penetrasjon på 113 mm. Interaksjonen endte med kontinuerlig glidning langs kabelen som varte fram til analysen ble avsluttet rundt 40 sekunder etter kontakt mellom klumpvekten og kabelen intraff. Den maksimale horisontale pull-over kraften og den maksimale kurvaturen økte gradvis under interaksjonen og forbipasserte de største verdiene for en perpendikulær treffvinkel. Gyldigheten av disse resultatene er likevel usikker, da klumpvekten gled inn i soner med større mesh størrelser. Videre var også løftkreftene fra trålbordene ikke var modellert, noe som førte til store bevegelser på tvers av trålretninge. Det er derfor usikkert om forfyttningen av trålposene og trålbordne for disse simulasjonene er korrekt.

Til slutt demonstrerte resultatene at førspenningen hadde en liten til ingen effekt på trålinteraksjonen. Ved å redusere førspenningen fra 10 kN til 1 kN ble det funnet at den maksimale pull-overkraften og den maksimale aksialkraften hadde en marginal reduksjon og den maksimale forflyttningen og den maksimale kurvaturen hadde en marginal økning.

Design-begrensningene på kurvatur og aksialkraft var basert på regler for fleksible risere. Ved å sammenligne verdiene fra simulasjonene ble det funnet at opp til 9.5 % og 80 % av kapasiteten ble brukt for henholdsvis aksialkraft og kurvatur. Man kan derfor konkludere med at lastnivåene som oppstår i kabelen fra interaksjonen med klumpvekten ikke overskrider tillatte nivåer. Det er likevel mulig at kabelen må beskyttes da glidningen langs kabelen for små treffvinkler kan true integriteten til ytterkappa.

Contents

List of Figures

List of Tables

List of Abbreviations

COG	Centre of gravity
DOF	Degree of freedom
HCP	Hydrodynamic centre point
MAF	Maximum axial force
MC	Maximum curvature
MHF	Maximum horizontal force
MVF	Maximum vertical force
ROV	Remotely operated Vehicle
TDP	Touchdown point

List of Symbols

A_t	Cross section are of a tensile armour wire
E	Modulus of elasticity
EA	Axial stiffness
EI	Bending stiffness
f	Yield criterion
F_f	Fill factor
F_p	Maximum horizontal pull-over force
F^t_{crit}	Critical tensile force
F_z	Maximum vertical pull-over force
V	Vertical contact force
V_{trawl}	Trawling velocity
g	Gravitational acceleration
g^*	Contact element gap
G	Shear modulus
H_sp	Height of free span
J	Second polar moment of inertia
J_s	2^{nd} deviatoric stress invariant
L_{clump}	Distance from reaction point to center of gravity of clump weight
m	Element consistent mass matrix
m_t	Steel mass of clump weight
n	number of wires in the cross section
OD	Outer diameter of power cable
R	Outer radius of power cable
$\bar{S}$	Hardening dependent material parameter
R^i	Internal radius
R^o	Outer radius
R_{tot}	Total thickness of all armour layers
T_p	Pull-over load duration
u, v, w	Displacements in relation to the local neutral axis
w_s	Submerged weight
y_brk	Lateral displacement leading to cable breaking free of the berm
y_{brk}	Lateral displacement where the the lateral scaling factor is reduced to its residual value
z_{pi}	Initial sea bed penetration
$\boldsymbol{a}$	Transformation matrix between local and global displacements
$\boldsymbol{C}$	Damping matrix

$\boldsymbol{C_0}$	Lumped damping matrix
$\boldsymbol{C^m}$	Elasticity tensor
$\boldsymbol{E}$	Green strain tensor
$\dot{\boldsymbol{E}}^{(p)}$	Plastic component increment of the green strain tensor
$\boldsymbol{f}$	Body force
$\boldsymbol{k}_m$	Element material stiffness matrix
$\bar{\boldsymbol{K}}_k$	Effective stiffness matrix
$\boldsymbol{k}_T$	Element tangential stiffness matrix
$\boldsymbol{K}_T$	Tangential stiffness matrix
$\boldsymbol{k}_\sigma$	Element initial stress stiffness matrix
$\boldsymbol{M}$	Stiffness matrix
$\boldsymbol{N}$	Interpolation function matrix
$\boldsymbol{r}$	Displacement vector
$\boldsymbol{R}_E$	External load vector
$\boldsymbol{R}_I$	Internal load vector
$\Delta\bar{\boldsymbol{R}}_k$	Effective load increment
$\Delta\boldsymbol{R}$	Load vector increment
$\boldsymbol{S}$	2^{nd} Piola Kirchoff stress tensor
$\boldsymbol{S}_{eq}$	Equivalent stress vector
$\boldsymbol{t}$	Surface traction
$\boldsymbol{T}$	Transformation matrix
$\boldsymbol{u}$	Displacement vector
$\ddot{\boldsymbol{u}}$	Acceleration field
α_l	lay angle
α_1, α_2	Rayleigh damping scaling parameters
α, β, γ	Parameters used in the HHT-α method
γ_s	Dry unit soil weight
δ	Virtual displacement
ϵ_D	Tolerance level
θ	Torsional rotation of local neutral axis
κ	Hardening parameters
$\dot{\lambda}$	Scalar dependent on current stress
μ_{axial}	Friction factor in the axial cable direction
ξ	Damping ratio
ρ_l	Locking radius
ρ_ϵ	Plastic yielding radius
ρ_{crit}	Critical bending radius
ρ	Material density
σ_y	Yield stress

1 Introduction

1.1 Motivation

The energy industry today is heavily dependent on fossil fuels to meet the demand of energy in the world, however the growing threat of global warming is to a large extent driven by emissions from such fuels. The Paris agreement, signed by most of the worlds countries, require that these emissions of greenhouse gases need to be cut drastically in the near future (Nations 2015). To replace fossil fuels, renewable power sources like solar and wind power plants is planned and built in an increasing number the last couple of years.

The Norwegian industry sector has invested a considerable amount of resources to develop technology for floating wind turbines to be placed along the Norwegian coast as wind currents are strong and stable here (Equinor 2020b). Placing turbines offshore are preferable to onshore find farms as the dimensions can be larger, which lead to higher efficiency. Moreover, placing turbines on land are often unpopular among the local population, which is another argument for moving the wind farms offshore.
Norwegian authorities approved the 8^{th} of April 2020 the Hywind Tampen project which will place eleven floating turbines to supply the Snorre and Gullfaks field with clean energy (Equinor 2020a). This is a part of Equinor strategy to reduce greenhouse gas emissions by electrifying the Oil and gas production at the Norwegian continental shelf. Several other fields on the Norwegian continental shelf are already supplied with clean electrical energy through export cables from land. Gina Krog, Martin Linge and Johan Sverdrup, which started its production in 2017, 2018 and 2019 respectively, are supplied with power this way. Troll A was already connected to the power grid in 1996 and there are currently several other platforms that are under consideration for being connected, including Troll C and Sleipner (Equinor 2018).

In order to supply the platforms with electrical power, either from land or from local wind farms, an extensive infrastructure of power cables placed at the sea floor is needed. This adds to the total amount of cables that are installed in Norwegian waters which are rapidly increasing.
These cables are exposed to various environmental loads as well as accidental loads from interference with dropped objects, anchors and fishing equipment. Failures of such cables lead to extensive costs as there are needed a considerable amount of planning and resources to replace submerged cables. Based on experience from the UK sector, which is the worlds leading country in production of offshore wind power per 2018, failures of subsea cables are reported as an important issue for wind farm operators. 75-80 % of the insurance claims or about 9 % of the total cost of the overall cost of a wind farm are related to such issues (Mountassir and Strang-Moran 2018). Even though only 13 % of the reported cases were associated with external and environmental causes, the savings related to hindering such failures could be considerable. Failure of cables can have more than just economic consequences as well. A recent accident where a dropped anchor damaged a submerged cable in the Oslo fjord led to an oil leakage from a protective layer in the cable. Even though such leakages are relatively small, it can have an considerable impact on the local ecosystem. Common ways to protect these cables from external loads are trenching, burial or rock dumping. These methods are, however, all costly operations and can be deemed unnecessary if it can be proven that the cables can withstand expected loads.

Trawling is an efficient way of catching large amount of fish in a short span of time and have long traditions in Norwegian waters. Interaction between trawling equipment and power cables can lead to large loads and is one of the major threats to the integrity of submerged cables.
According to DNVGL-RP-F111 recommend practice, bottom based structures installed at Norwegian continental shelf should be kept away from fishing banks in order to avoid such loads (DNVGL 2017). Nevertheless, fishing activity may occur away from dedicated fishing zones, especially since subsea structures are known to attract fish.
Loads from interaction between marine pipelines and trawling equipment have already been subject to extensive research, as there are potential severe consequences on the environment resulting from damaging pipelines transporting hydrocarbons. However, the knowledge regarding the interaction

between trawling equipment and submerged power cable is scarce.
Power cables and pipelines have similarities with regard to shape and build structure but pipelines are generally stiffer than cables. One can therefore expect steel pipelines to have a larger load capacity and will have a better chance to withstand trawl loads. On the other hand, due to the compliance of the power cable it is possible that the load from the interaction with trawling equipment will be lower compared to that of the steel pipelines. Free spans will also be less of a concern, as the cable will to a greater extent follow the topography of the sea bottom.

1.2 Scope of the thesis

Steel pipelines installed at the Norwegian continental shelf are designed to withstand interaction with trawl gear following DNVGL-PR-F111. There does not exist similar rules for design of subsea power subjected to such loads. The goal of this master thesis is to investigate if a typical subsea export cable can withstand such loads, and if there are needed to take preventive actions such as rock dumping or trenching to hinder failure. Furthermore, the loads will be compared against predicted loads from DNVGL-RP-F111 to determine if can be used for predicting loads on offshore power cables. As there are several parameters that can effect the interaction between the trawl gear and the power cable, sensitivity studies of important parameters are included. The parameters that are to be studied are the relative sea bottom penetration between the clump weight and the power cable, the pretension of the cable and the hit angle.

The study will focus on export cables, which has larger dimensions than for instance the cables connecting the floating turbine to collecting point. The reason for this delimitation is because export cables extends far away from visible surface structures and spanning over larger distances, making them more prone to collisions from unaware fishermen. Nevertheless, local exchange cables has a lower load capacity and interaction with trawling equipment should also be investigated such cases, though it is not part of the scope of this thesis.

1.3 Thesis structure

Chapter 2 describes build-up and mechanical properties of offshore power cables, trawl gear concepts, relevant rules and regulations and previous research on trawl interference loads.

Chapter 3 describes the finite element formulation and solution method used in SIMLA.

Chapter 4 describes the properties and build up of the SIMLA model used in the simulations, a description of a cable length and mesh sensitivity study, and a description of the simulation cases.

Chapter 5 presents figures and tables with detailed results from the simulations alongside a discussion of the results.

2 Background

2.1 Subsea Power cables

Subsea power cables are used to transport electrical power subsea, often over longer distances. Some applications on the Norwegian continental shelf includes supplying platforms with power, export excess or import needed power from neighbouring countries and transporting power generated from offshore wind farms.
In the wind industry it is used various dimensions based on the application. The general layout of a wind farm with a transmission grid connected to land is shown in figure Figure 2.1. The power transmission system consist of several levels which have different cable dimensions and voltage in order to minimize losses. Locally, there are a collection grids, where clusters of turbines are connected together in a single cable and connected together in a connection point where the voltage and cable dimension is increased to be suitable for exportation (Georgios 2010).

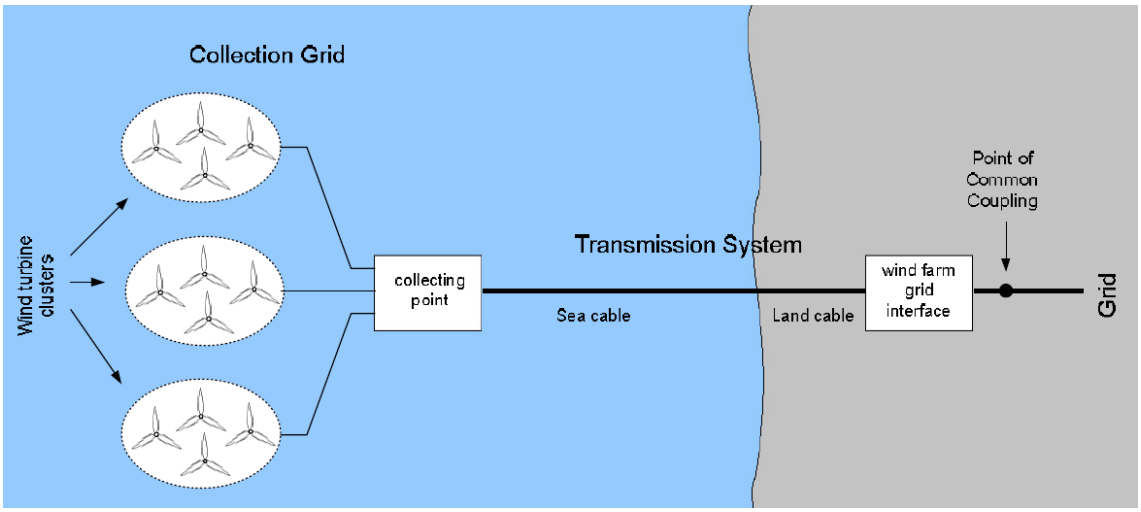

Figure 2.1: Typical layout for a wind farm with a transmission grid connected to land (Georgios 2010)

Figure Figure 2.2 show a typical build up of a export subsea power cable. It transport power through a direct current to limit losses over greater distances and therefore only uses a single core. The conductor is located at the core of the cable and often consist of stranded round wires made out of copper or aluminium. To hinder electrical leakage, an extruded polyethylene or a similar polymer is used to form a thick insulation layer around the conductor. The insulating capacity of the insulation layer is greatly affected by local stresses which can arise if the irregularities from other layers are in direct contact with it. Insulation screens of a semiconducting material are therefore placed on both sides of the insulation layer (Worzyk 2009).

The core and insulation layers should be protected against loads both during and after installation. This is done through two armour layers consisting of several strands of steel wires. Due to the helix configuration of the steel wires, the axial, bending and torsion action of the cable are coupled. The two separate armour layers have the same wire sizes and counteracting helixes in order make it torsion balanced(Sævik 2017a). The outermost layer of the cable is the protective sheath, often made out of polyethylene. It's task is to protect the rest of the cable from the environment, especially the water which can cause corrosion of the steel wires and wear down the insulation layer. Water absorbing swelling tapes are used between the outermost layers to absorb any humidity that mange to diffuse through the sheath over the lifetime of the cable. If the outer sheath become damaged and leaks in water, the swelling tapes will absorb some of the water and start to swell, stopping the water from spreading further in the process (Worzyk 2009).

Figure 2.2: Armoured single cored subsea export cable (Statnett 2014)

2.2 Trawl gear

Trawling is an important method of catching fish, both at world basis and in Norway. It's an active method where one or more nets, often called trawl bags, are dragged through the water with a greater speed than the fish such that it gets trapped inside. Trawling can be done at any depth, depending on which type of fish that is desired (Karlsen and Simonsen 1989). In this master thesis bottom trawling of interest, as it can interact with bottom structures. Trawling is often categorized by which method that is used to keep the net open, which include:

- Beam trawl
- Otter trawl
- Twin trawl

2.2.1 Beam trawl

The beam trawl keeps the net fixed open by the use of a transverse beam with trawl shoes at the ends. The advantage of this method is that the trawl bag kept open regardless of the vessel speed. The disadvantage is that the height of the opening is about 1 meter, which makes it unusable for most relevant species in Norwegian waters. Typically vessels using this method have two such trawls towed from a single vessel. (Karlsen and Simonsen 1989) A typical layout for a beam trawl is shown in Figure Figure 2.3.

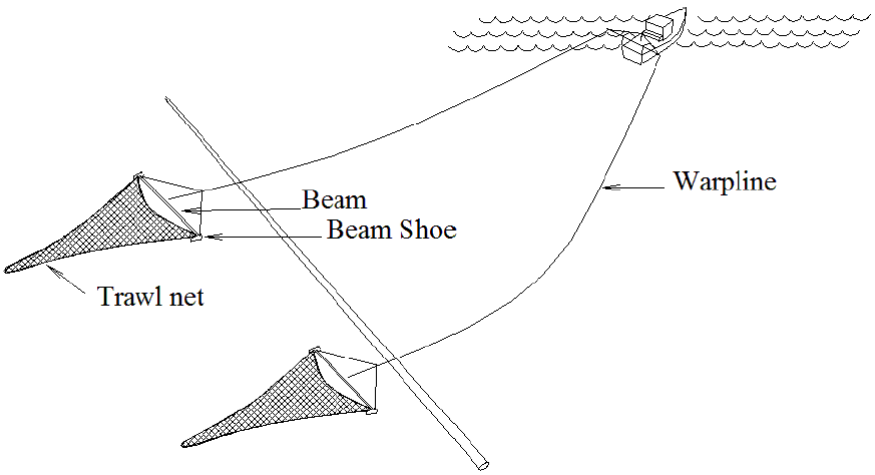

Figure 2.3: Beam trawl with two nets towed out from a single vessel (DNVGL 2017)

2.2.2 Otter trawl

The otter trawl keeps the net open by the use of otter boards, also called trawl boards. They are connected to the trawl bag through sweep lines and to the vessel with warp lines. When the trawl is dragged through the water, the otter boards will generate hydrodynamic lift forcing the trawl boards apart. Buoyancy elements are placed at the top of the net and weights at the bottom, which combined with the hydrodynamic lift from the trawl boards keep the trawl bag open (Karlsen and Simonsen 1989). A typical otter trawl configuration is shown in Figure Figure 2.4.

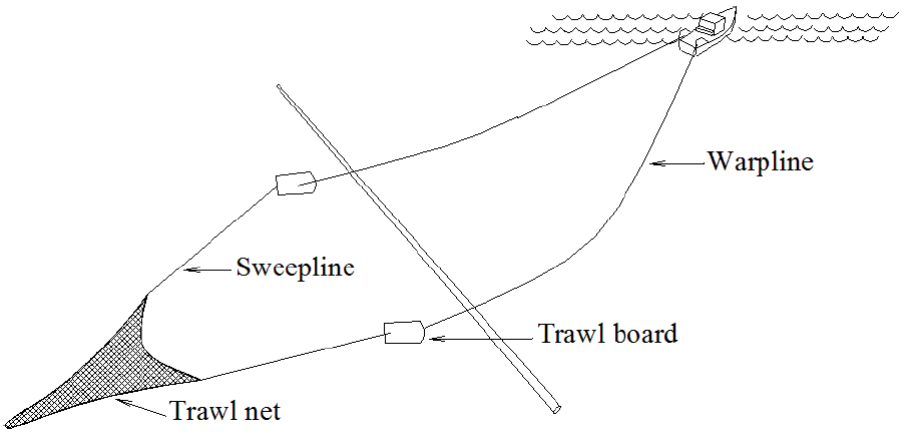

Figure 2.4: Typical otter trawl configuration (DNVGL 2017)

2.2.3 Twin trawl

The twin trawl is an extension of the otter trawl where a single vessel is towing two trawl bags side by side. They are separated by a clump wight, to which the warp lines are attached. The trawl bags are kept open by two trawl boards, similarly to the otter trawl, which again are attached to the vessel through two sweep lines. The configuration is shown in Figure Figure 2.5. The main advantage of this method is that most of the hydrodynamic resistances are transferred to the centre warp line. This enable a larger trawl bag opening which again increases the efficiency of the trawl. As most of the towing force is transferred to the warp line, the upward pull is significantly higher compared to that of the otter trawl. A clump weight is therefore added between the trawl bags to

counteract the increase in upward pull, and can have a mass up to 8000 tonnes (DNVGL 2017). This trawling method is commonly used in Norwegian waters today because of it's efficiency.

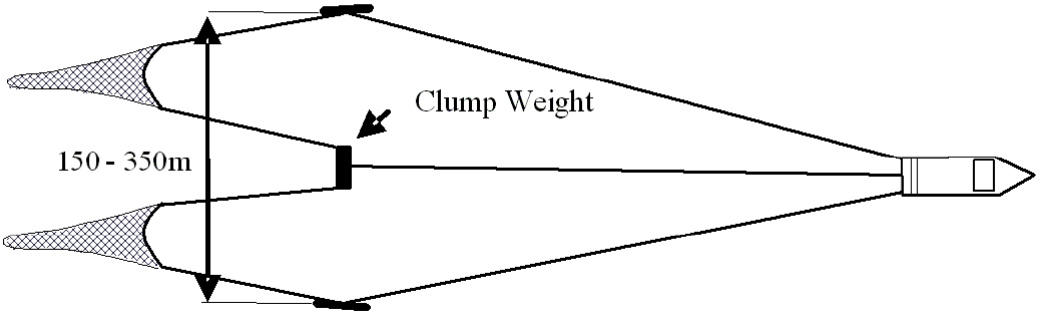

Figure 2.5: Typical twin trawl configuration (DNVGL 2017)

There exist several different clump weight designs that are used in the industry today. As the main goal of the clump weight is to add weight, it can be achieved by simply connecting heavy chains in between the two trawl nets. The resistance force from dragging it along the sea floor can be reduced by a more advanced design though. An example is the bobbin or roller, which rolls along the sea floor bu the use of two small roller balls. The bobbin type is shown in Figure Figure 2.6(a), which has a weight up to 3.5 tonnes and is often used by smaller trawl vessels (Fyrileiv et al. 2008). A typical roller clump weight is shown in Figure Figure 2.6(b) which can have a mass of up to 9 tonnes for the largest shrimp trawlers uses in the Barents Sea (DNVGL 2017). In this thesis, a twin trawl configuration with a roller clump weight is chosen because of it's typically large mass and therefore potential to inflict large loads.

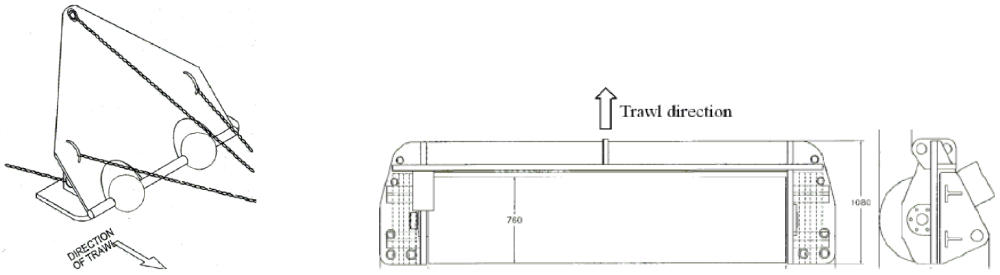

(a) Bobbin type

(b) Roller type

Figure 2.6: Special designed clump weights for reduced resistance (DNVGL 2017)

2.3 Rules and regulations

DNVGL-ST-0359 describes the requirement for designing subsea power cables for wind power plants. According to the standard, the cable protection design include protection against a number of hazards including "penetration of fishing gear, e.g. during bottom-trawling activities" (DNVGL 2016). There exist no detailed guidelines on how to model these loads like there exist for steel pipelines in DNVGL-RP-F111. Consequently, the loads must either be modelled using a structural analysis program like SIMLA or through physical model tests. Normally both computer simulations and model tests are used in combination to validate the results. To decide if the design is safe, the capacity need to exceed the expected loads multiplied by a safety margin which is often set by the Class Societies. The American Petrolium Institute have issued a range of such standards, including one for Unbonded Flexible Pipes that can be used for determining safety factors for subsea cables.

2.3.1 DNVGL-RP-F111

DNVGL-RP-F111 is a recommended practice (RP) that provides criteria and guidance for designing pipelines subjected to interference from trawl gear. The document contain empirical design loads based on trawl gear data from the Norwegian Sea and the North Sea. It is valid for interaction between otter, beam or twin trawl equipment with rigid steel pipelines with outer diameter of 10" or above. The RP divides the interaction into three separate phases: Impact, Pull-over and possibly a hooking phase. The impact phase is very short so that the kinetic energy transferred from the trawl gear is mostly absorbed through local deformation. This phase is relevant for evaluating the integrity of the outer protective sheath and indentation or fracture of the pipe shell. The pull-over phase deals with the global response of the pipeline as the trawl gear travels across it, leading to large displacements. Local deformations and indentations caused by the initial impact are not taken into consideration in this phase. Hookling occurs if the trawl gear get stuck beneath the pipeline during the pull-over phase leading to large loads which in the most extreme cases can be as large as the break strength of the warp line. The scope of this thesis is limited to the pull-over phase.

It is specified in the RP that the response of the pipelines should be done in a dynamic analysis, as a static analysis is most likely going to be non-conservative. Non-linear effects from non-linear material behaviour, large displacements and geometrical effects, soil resistance and potential buckling effects should be included. The length of the power cable model should be sufficiently long to model the complete soil-pipeline interaction without the interference of the boundary conditions.

The pull-over load is represented by a point load at the center of the impact. The load is applied in terms of a maximum load parallel to the sea floor and a maximum load vertically. These two loads are scaled over a time history as shown in Figure Figure 2.7.

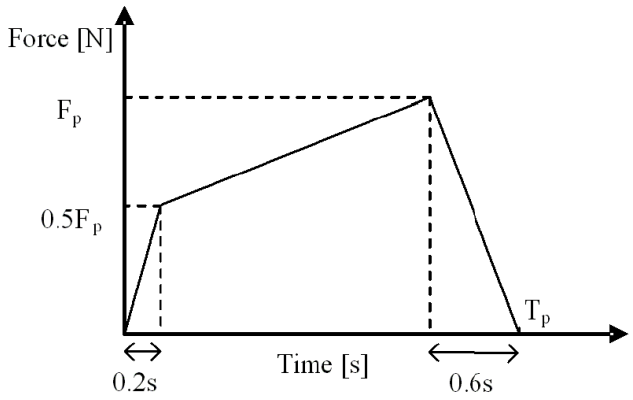

Figure 2.7: Force-time history applied to simulate the interaction between a pipeline and a clump wight (DNVGL 2017)

The duration of the force-time history can be estimated by combining the time it takes to stretch out the warp line and the time it takes to displace the pipelines which is described by the formula:

$$T_p = \frac{F_p}{k_w \cdot V_{trawl}} + \frac{\delta_p}{V} \tag{2.1}$$

Where k_w is the warp line stiffness, V_{trawl} is the trawling velocity and δ_p is the pipeline displacement at the point of interaction. Since the displacement is unknown prior to the simulation it has to be assumed and corrected afterwards.

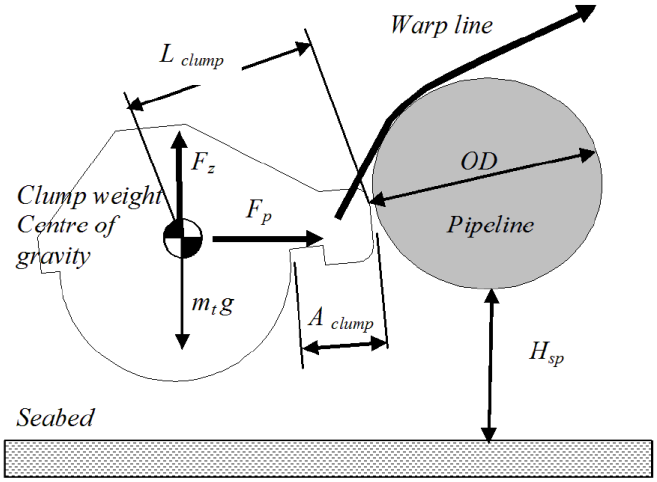

Figure 2.8: Interaction between a pipeline and clump weight (DNVGL 2017)

The maximum magnitude of the loads, the properties shown in Figure Figure 2.8 has to be known. The maximum parallel directed force is found by the use of the empirical formula:

$$F_p = 3.9 \cdot m_t \cdot g \cdot (1 - e^{-1.8 \cdot h'}) \cdot (\frac{OD}{L_{clump}})^{-0.65} \tag{2.2}$$

$$h' = \frac{H_{sp} + OD}{L_{clump}} \tag{2.3}$$

Where m_t is the steel mass, g is the gravitational acceleration, OD is the outer diameter of the pipeline, L_{clump} is the distance from the interaction point to the center of gravity of the clump weight and H_{sp} is the span height.

And the maximum vertical force can either be directed upward or downwards. The most critical then need to be selected to govern the design. The maximum upward vertical directed force is expressed as:

$$F_z = 0.3F_p - 0.4 \cdot m_t \cdot g \tag{2.4}$$

And the maximum downwards directed force is expressed as:

$$F_z = 0.1F_p - 1.1 \cdot m_t \cdot g \tag{2.5}$$

2.3.2 API 17J - Specification for Unbonded Flexible Pipe

API Specification 17J, Specification for Unbonded Flexible Pipe describe the requirements for design of flexible pipelines issued by the American Petroleum Institute (API). Flexible pipelines are very similar to subsea export cables, more so than the steel pipelines that DNVGL-PR-F111 is based upon. The design requirements in this standard can therefore be used to check if the structural response is within allowable bounds.
The main difference between the export cable and the flexible pipeline lies in the bore, located in the centre of the pipeline and which enable the flow of oil and gas. This is replaced by a copper core in which the electrical power is transmitted. As the stiffness of copper is much lower than that of the tensile armour made out of steel, then one can assume that mainly the tensile armour that will govern the strength in the axial direction. In bending, the outermost layers like the steel armour and the polymer sheaths will be governing the strength of the cable. Table Table 2.1 show the safety factors that are to be used in design. (API 2014)

Table 2.1: Safety factor used for design of flexible risers (API 2014)

Component	Failure modes	Design criteria	Factor
Tensile armour	Breakage	Stress	0.85
Tensile armour	Locking	Bending radius	1.1 x LR
Outer sheath	Rapture	Strain	7.7%

The API standard operate with a single safety factor that take into consideration uncertainties in both load and capacity. The intermediate sheaths are not listed here as they will have lower strain levels than the outermost sheath and will not be governing. The thinning of the intermediate sheaths are also disregarded as the effect will be small over the short time-span of the trawling load. For the locking radius, LR, the power cable is assumed to be within the category "Dynamic supported" as it is supported by the sea bottom during the entire interaction with the trawl gear.

2.3.3 Design limits

The design limit set the bounds for how large loads the structure can be subjected to while the integrity of the structure is not threatened. The assumptions that have been used for estimating these forces may also have bounds that need to be taken into consideration. Safety factors should also be included to handle any uncertainties in the loads and mechanical properties of the structure.

Because of the low bending stiffness of the cable, most of the load capacity of the power cable lies in the axial direction. The tensile armour tethers are the stiffest component of the cable, and will therefore experience the highest loads when subjected to axial tension. The design check for axial capacity will therefore focus the tensile armour capacity. For the cases selected in this thesis, the axial force will always be tensile, by assuming that locking does not occur then buckling of the cable can be disregarded. Based on API 17J, the axial capacity should be selected as either 0.9 times the ultimate tensile strength or the yield strength. The stress level can be calculated based on the assumption that the total layer load uniformly over all the the wires in the layer. (API 2014). Fracture is disregarded and fatigue considerations are not taken into consideration here, as the material tolerances and the cumulative damage at the present point in the life cycle of the cable is not known.

The stress level in the tensile armour can be estimated as (Sævik 2017a):

$$\sigma = \frac{T_{eff}}{2\pi \cdot R \cdot t_{tot} \cdot F_f \cdot cos^2(\alpha_l)} \tag{2.6}$$

Where T_{eff} is the effective tension, R is the mean radius of the steel tensile armour layer, t_{tot} is the total thickness of the the steel layers combined, F_f is the fill factor and α_l is the lay angle of the tensile armour.
By using the safety factor for breakage in Table Table 2.1, $\gamma_T = 0.85$ and assume a steel yield σ_y = 350 MPa, the allowed axial force in the cable, T_{lim}, can be determined as:

$$\begin{aligned} T_{lim} &= \gamma_T \cdot \sigma_y \cdot 2\pi \cdot R \cdot t_{tot} \cdot F_f \cdot cos^2(\alpha_l) \\ &= 0.85 \cdot 350\ MPa \cdot 2\pi \cdot 0.127\ m \cdot 0.01\ m \cdot 0.9 \cdot cos^2(20^\circ) = 1.89\ MN \end{aligned} \tag{2.7}$$

The bending limit is governed by the most critical of the allowed strain level in the outer sheath of the cable and the bending radius leading to locking of the tensile armours. Locking occur when the steel tendons are coming into contact under excessive bending. The consequence of locking can be local buckling destruction and plastic layer overstraining (API 2014) and the assumption of linear properties are no longer valid. The locking curvature, κ_l, of the tensile armours at the compressive side can then be found to be (Sævik 2017a):

$$\kappa_l = \frac{1 - F_f}{R} \tag{2.8}$$

Using the design criterion for locking in Table Table 2.1, the maximum curvature that is allowed accounting for locking is determined as $\gamma_{locking} = 1.1 \cdot LR$. The design limit can then be found to be:

$$\kappa_{l,lim} = \frac{1}{\gamma_{locking}} \cdot \frac{1 - F_f}{R} = \frac{1}{1.1} \cdot \frac{1 - 0.9}{0.152\ m} = 0.60\ m^{-1} \tag{2.9}$$

The outer sheath may also be governing the maximum allowed curvature of the cable. The curvature leading to critical strain in the outer sheath can found by the relation (Sævik 2017a):

$$\kappa_\epsilon = \frac{\epsilon_{lim}}{R} \tag{2.10}$$

API 17J states that the strain in the plastic layers should not exceed 7.7% (API 2014). The curvature leading to this amount of strain in the outer fibres of the cable sheath is:

$$\kappa_{\epsilon,lim} = \frac{0.077}{0.172\ m} = 0.45\ m^{-1} \tag{2.11}$$

The strain in the outer sheath is therefore governing and the total curvature limit is equal to κ_{lim} = 0.45 m^{-1}.

2.4 Previous research on trawl gear interactions

This subsection is a continuation of a literature study conducted during the project thesis work fall 2019.
There exist several reports of studies addressing trawling loads on subsea pipelines with use of the simulation tool SIMLA. Studying existing publications on trawl-pipeline interactions are relevant for this thesis as both pipelines and cables are slender structures and may behave similarly when subjected to trawling loads. The relevant research is described in the remainder of this chapter, which contains studies with both clump weights and trawl boards in interaction with steel pipelines.

Generally it has been shown that the DNVGL-RP-F111 code generally overpredicts the pull-over loads for most cases. Furthermore, it has been shown that parameters like diameter of the pipeline, free-spans, direction of trawling, length of warp line and centre of gravity of the clump weight has an impact on the pull-over load. Effects of the relative penetration between the trawl gear and the pipeline has not been studied, probably because free spans are more important for steel pipelines. Furthermore, the effect of pre-tension on the interaction have not been studied.

Møller (2009) investigated in his master thesis interference between trawl boards and a pipelines. The main finding were that the DNV-RP-F111 code overestimated the lateral displacements for free spans of 2 meters and less.

In his master thesis, Longva (2010) investigated the effect of including the effect of seabed proximity on the trawl board added mass, the implication of a rectangular trawl board geometry, as well as modifying the hydrodynamic model to better take into consideration seabed proximity and forward speed. His findings showed that the inclusion of seabed proximity of the trawl board added mass had no influence on the pipeline response during pull-over. The effect of rectangular trawl board geometry slightly increased the pull over time for no span height and the load for 1 m span height. He also discovered that the maximum trawl load did not occur for a perpendicular crossing. Finally, the new hydrodynamic model indicated that DNV-RP-F111 underpredicts the pull-over load when the span height was set to zero.

Maalø (2011) compared in his master thesis simulations of a clump weight interacting with a pipeline with small scale model tests. He found that there was a good agreement between the simulations in SIMLA and the model test results. Furthermore it was found that higher flexibility in the pipeline and a forward placed center of gravity led to lower trawl loads, and a longer warp line led to higher trawl loads.

Berg Johansen (2012) further investigated the effect of different parameters in simulations of clump weight and pipeline simulations with the SIMLA software. She found that reduction of pipeline diameter, and therefore also the bending stiffness, reduced the trawl load for low free spans. On the other hand, for high free spans the pull-over force increased for smaller pipe diameters. Finally, clump weight wobbling and extending the warp line bracket were both found to reduce the pull-over force.

Longva et. al (2013) carried out a validation study where 34 model test runs were carried out with pull-over interaction of trawl boards and pipelines. The results were compared to numerical studies in SIMLA, and the results were predicted with a 10% margin of the test results. The interaction was found to be greatly influenced by the board-pipe friction coefficient, the tension in the wire between board and trawling net, the towing line drag properties, and the direction of over-trawling.

Krogstadmo (2019) investigated the effect of rock dumping on subsea pipelines in interaction with a clump weight through simulations in SIMLA. He found that the largest load effects occur through interaction between the pipeline and the clump weight roller and are worst for wide rock dumps. Low rock dump heights were found to be most optimal for narrow widths and the slope of the rock dump were the most important for reduction of loads for wide rock dumps. The diameter of the pipeline was found to also be an important parameter to determine the reduction of pull-over load due to rock dumping.

3 Finite element analysis

This section is a continuation of a literature study on finite element analysis in the project thesis from the fall 2019. It covers the theory behind the finite element program SIMLA, which is used for structural analysis in this thesis. The program is tailor-made for pipeline analysis and is developed bottom-up with focus on data structure (Sævik 2019). The data handling makes the program of choice when working with capacity and local response for slender structures like interaction between trawl gear and power cables. The SIMLA program structure is described in sub-chapter 3.1, while the solution procure of the finite element code is described in sub-chapters 3.2 - 3.8.

3.1 Program structure

Figure 3.1 show the structure of SIMLA. The script used as input to the SIMLA solver is edited in the FLEXEDIT program, which also can be used as a control unit for running the solver and post processing directly from the Graphical user interface. However, when running several simulations consecutively it is more efficient to execute several run commands in the terminal using a batch file.
The result database contain specified nodal positions, element forces, strains and stresses which are stored in .RAF-file, while detailed time-series results are stored in a .DYN-file. Xpost is a tool that can be used to quickly visualize the time series stored in the .dyn-file, which is useful for validating the simulations before the post-processing. Text files with specific results can be generated using the SIMPOST post-processor for .RAF-files and DYNPOST for .DYN-files. Finally, the MATRIXPLOT software can be used to generate plots from text files generated by SIMPOST and DYNPOST.

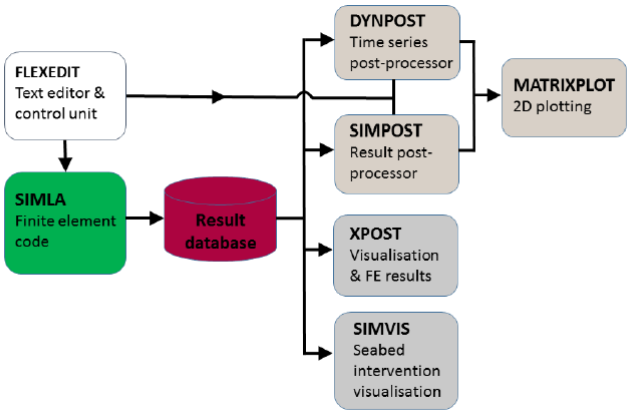

Figure 3.1: SIMLA program structure (Sævik 2019)

3.2 Basis for finite element analysis

A finite element program solves a differential equation by dividing it into a finite number of elements. This is a powerful tool when dealing with complex problems that are impossible to solve by the use of analytical methods and it can be used for various problems like diffusion, heat transfer, fluid flow and elasticity. In this chapter the method for solving structural problems in SIMLA with the use of this method is described.

In order to solve the differential equation of the structure, it is split up in several smaller parts, and an approximation of the solution is found numerically based on the principles described later on in this section. In order to solve the differential equation, it is necessary to introduce the following relations:

- Equilibrium

- Kinematic relation
- Constitutive relation

These relations are described in the following sub-chapters.

3.2.1 Equilibrium

Equilibrium is determined by the principle of virtual displacements. Here one assume a balance between external and internal work due to a virtual displacement $\delta\mathbf{u}$. As the shape functions used to describe the displacements are only exact where the boundary conditions are imposed, and the integration is done to be exact when integrated over the average of the whole body, the solution is only an approximation at an arbitrary point in the volume. By default the weak formulation used to describe this equilibrium is as follows (Sævik 2017b):

$$\int_V \rho \cdot (\ddot{\mathbf{u}}\text{-}\mathbf{f}) \cdot \delta\mathbf{u}\ dV + \int_{V_0} (\boldsymbol{S} - \boldsymbol{S_0}) \cdot \delta\boldsymbol{E}\ dV - \int_S \mathbf{t} \cdot \delta\mathbf{u}\ dS = 0 \tag{3.1}$$

Where ρ is the density of the material, $\ddot{\mathbf{u}}$ is the acceleration field, $\mathbf{f}$ is the body force vector, $\boldsymbol{S}$ is the 2^{nd} Piola Kirchoff stress tensor, $\boldsymbol{E}$ is the green strain tensor, $\mathbf{t}$ is the surface traction and $\mathbf{u}$ is the displacement vector. The subscript with 0 means that one refer to the initial state.

If the true strain and Cauchy stress was used instead of 2^{nd} Piola Kirchoff stress and Green strain, the solution would be more exact, but at a higher computational cost. However, if the displacements are small compared to the length of the element this error will be small.

3.2.2 Kinematic relation

The kinematic relation for a linear-elastic beam element follow the assumption that Euler-Bernoulli beam theory is applicable. Shear deformations are therefore neglected, while coupling between longitudinal strain and torsion are important to describe the helix structure in the armour of the cable, and are therefore included. The longitudinal Green strain can therefore be expressed as:

$$E_{xx} = u_{x0,x} - yv_{y0,xx} - zw_{z0,xx} + \frac{1}{2}(u_{y0,x}^2 + u_{z0,x}^2) \tag{3.2}$$

Where u,v and w are the displacements in relation to the local neutral axis (Sævik 2017b). A non-linear element would also have a term coupling the axial with torsional action. The terms are not included here as there are only used linear elements the models used in this thesis.

3.2.3 Material law

The material law describe the relation between stress and strains, and is simply expressed by the Young modulus and the Poisson ratio for a linear elastic material model. The elastic formulation of the stress-strain relationship can be expressed as follows:

$$\begin{bmatrix} \sigma_{11} \\ \sigma_{22} \\ \tau \end{bmatrix} = \frac{E}{1-\nu^2} \begin{bmatrix} 1 & \nu & 0 \\ \nu & 1 & 0 \\ 0 & 0 & \frac{1-\nu^2}{2(1+\nu)} \end{bmatrix} \begin{bmatrix} \epsilon_{11} \\ \epsilon_{22} \\ \gamma \end{bmatrix} \tag{3.3}$$

In this thesis, the material behaviour is assumed to be purely linear elastic. However, if one were to include non-linear material model, there would be a non-linear relation between the stress and strains. The following rules had to be defined to have sufficient information to solve equilibrium equation:

- **Yield condition** - Describes the combination of principal stresses that cause the stress to exceed the yield stress and cause the material to be plastic. For metallic materials experiments have shown that the Von Mises initial yeild criterion best describe the yielding behaviour. Though this model require the use of Cauchy stress, and the assumed stress is described by the the 2nd Piola circhoff stress, the strains in metallic materials are usually so small that

the 2^{nd} Piola stress tensor coincided with the Cauchy stress tensor (Moan 2003). In the two dimensional case the yield criterion can therefore be expressed as:

$$f = \sqrt{\sigma_1^2 + \sigma_2^2 - \sigma_1\sigma_2} - \sigma_Y = 0 \tag{3.4}$$

In the SIMLA software the yield surface is expressed by the 2^{nd} deviatoric stress invariant, J_2, and the hardening parameter κ. Here it is assumed that yielding is independent on the the first and third deviatoric stress invariant, and the yielding condition is therefor given as:(Sævik 2017b)

$$f(J_s, \kappa) = \sqrt{3J_2} - \bar{S}_\kappa \tag{3.5}$$

- **Flow rule** The flow rule relates the increment plastic strain increment at each step of the load history. Further, the material is assumed to follow Ducker's postulate for a stable material, which yields the normality condition given as:

$$\dot{E}^{(p)} = \dot{\lambda}\frac{\partial f}{\partial \boldsymbol{S}} \tag{3.6}$$

Where $\dot{E}^{(p)}$ is the plastic component of the Green strain tensor and $\dot{\lambda}$ is a scalar dependent of the current stress, strain and stress rate.(Sævik 2017b)

- **Hardening rule** - Describes how the yield surface changes as the plastic zone grows. The hardening parameter, κ, can be expressed by the total amount of plastic work done. This is found by integrating the equivalent stress times the plastic strain increment

$$\kappa = \int S_{eq}\dot{E}_{eq}^{(p)} \tag{3.7}$$

3.3 Element formulations

This section contains a description of the element types used to form the SIMLA model described in section 4. The majority of the elements used are pipe31 and body502, later refereed to as linear pipe elements and body elements respectively.

3.3.1 Pipe31

Pipe31 is a linear pipe element defined between two nodes. Each of the two nodes have six degrees of freedom (DOF) as shown in Figure 3.2 and the displacement over the element is described by the use of interpolation functions as described in Equation 3.8 (Sævik 2017b).

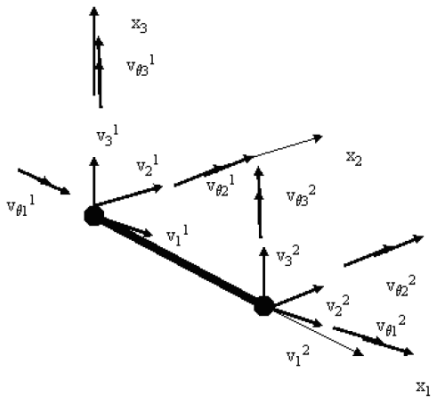

Figure 3.2: Pipe31 degrees of freedom (Sævik 2017b)

$$\begin{bmatrix} u_1 \\ u_2 \\ u_3 \\ \theta_1 \end{bmatrix} = \boldsymbol{N} \begin{bmatrix} v_1^1 \\ v_2^1 \\ v_3^1 \\ v_{\theta 1}^1 \\ v_{\theta 2}^1 \\ v_{\theta 3}^1 \\ v_1^2 \\ v_1^2 \\ v_1^2 \\ v_{\theta 1}^2 \\ v_{\theta 2}^2 \\ v_{\theta 3}^2 \end{bmatrix} \tag{3.8}$$

where $\boldsymbol{N}$ is:

$$\begin{bmatrix} 1-\xi & 0 & 0 & 0 & 0 & 0 & \xi & 0 & 0 & 0 & 0 & 0 \\ 0 & 1-3\xi^2+2\xi^3 & 0 & 0 & 0 & l\xi(\xi-1)^2 & 0 & 3\xi^2-2\xi^3 & 0 & 0 & 0 & -l\xi^2(\xi-1) \\ 0 & 0 & 1-3\xi^2+2\xi^3 & 0 & -l\xi(\xi-1)^2 & 0 & 0 & 0 & 3\xi^2-2\xi^3 & 0 & l\xi^2(\xi-1) & 0 \\ 0 & 0 & 0 & 1-\xi & 0 & 0 & 0 & 0 & 0 & \xi & 0 & 0 \end{bmatrix}$$

The material law is also assumed to be within the elastic domain. And Equation 3.3 can therefore be applied. Using the interpolation function described in Equation 3.8 the distributed loads, mass and damping over the element can be defined. Damping consist of both lumped and Raleigh damping on element level, and element loads are linearly interpolated over the length of the element. Hydrodynamic loads specifically are based on Morrison's equation, which are formulated as:

$$\rho \frac{\pi}{4} D^2 C_{m,t} \ddot{u}_y = \frac{1}{2} \rho C_{d,t} \sqrt{(\dot{w}_x - \dot{u}_x)^2} (\dot{w}_x - \dot{u}_x) \tag{3.9}$$

$$\rho \frac{\pi}{4} D^2 (C_{m,n} - 1) \ddot{u}_y = \rho \frac{\pi}{4} D^2 \ddot{w}_y + \frac{1}{2} \rho C_{d,n} \sqrt{(\dot{w}_y - \dot{u}_y)^2 + (\dot{w}_z - \dot{u}_z)^2} (\dot{w}_y - \dot{u}_y) \tag{3.10}$$

$$\rho \frac{\pi}{4} D^2 (C_{m,n} - 1) \ddot{u}_z = \rho \frac{\pi}{4} D^2 \ddot{w}_z + \frac{1}{2} \rho C_{d,n} \sqrt{(\dot{w}_y - \dot{u}_y)^2 + (\dot{w}_z - \dot{u}_z)^2} (\dot{w}_z - \dot{u}_z) \tag{3.11}$$

Where $C_{m,t}$ and $C_{m,n}$ are the added mass coefficient in the tangential and normal direction respectively, $C_{d,t}$ and $C_{d,n}$ are the drag coefficient in the tangential and normal direction respectively, $u_x - u_z$ are the body displacements in the respective DOFs and $w_x - w_z$ are the water particle displacements in the respective DOFs (Sævik 2017b).

3.3.2 Body502

Body502 is a single-noded rigid body element with 6 degrees of freedom. The element has only mass and hydrodynamic forces, which are described in Equation 3.12, and is often used to be able to define hydrodynamic coefficients that take into account boundary effects from the seabed. The position of the body is defined by the elemental coordinate system located at the centre of gravity (COG) where the gravity load is applied and local velocities and accelerations are measured. The hydrodynamic centre point (HCP) can be eccentric relative to the COG, where the hydrodynamic forces are applied. The contribution of the element to the system mass matrix and hydrodynamic load vector is defined as shown in Equation 3.3.

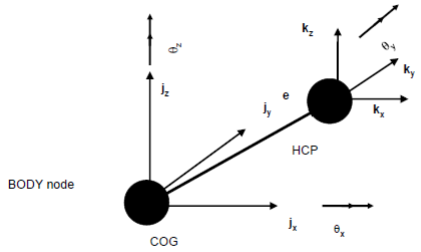

Figure 3.3: Body502 coordinate system (Sævik 2017b)

$$\begin{bmatrix} m_{11}+\rho m_{a11} & . & . & . & . & \rho m_{a16} \\ & m_{22}+\rho m_{a22} & . & . & . & . \\ & & m_{33}+\rho m_{a33} & . & . & . \\ & & & m_{44}+\rho m_{a44} & . & . \\ & Sym. & & & m_{55}+\rho m_{a55} & . \\ & & & & & m_{66}+\rho m_{a66} \end{bmatrix} \begin{bmatrix} \ddot{u}_x \\ \ddot{u}_y \\ \ddot{u}_z \\ \ddot{\theta}_x \\ \ddot{\theta}_y \\ \ddot{\theta}_z \end{bmatrix} =$$

$$\frac{1}{2}\rho \begin{bmatrix} C_{11} & . & . & . & . & C_{16} \\ . & C_{22} & . & . & . & . \\ . & . & C_{33} & . & . & . \\ . & . & . & C_{44} & . & . \\ . & . & . & . & c_{55} & . \\ C_{61} & & & & & C_{66} \end{bmatrix} \begin{bmatrix} |\dot{w}_x - \dot{w}_x|(\dot{w}_x - \dot{w}_x) \\ |\dot{w}_y - \dot{w}_y|(\dot{w}_y - \dot{w}_y) \\ |\dot{w}_z - \dot{w}_z|(\dot{w}_z - \dot{w}_z) \\ |\dot{\theta}_x - \dot{\theta}_x|(\dot{\theta}_x - \dot{\theta}_x) \\ |\dot{\theta}_y - \dot{\theta}_y|(\dot{\theta}_y - \dot{\theta}_y) \\ |\dot{\theta}_z - \dot{\theta}_z|(\dot{\theta}_z - \dot{\theta}_z) \end{bmatrix} + \begin{bmatrix} \rho m^*_{a11} & 0 & 0 \\ 0 & \rho m^*_{a11} & 0 \\ 0 & 0 & \rho m^*_{a11} \end{bmatrix} \begin{bmatrix} \ddot{w}_x \\ \ddot{w}_y \\ \ddot{w}_z \end{bmatrix} \quad (3.12)$$

Where subscripts i =1-3 refers to translational degrees of freedom and i = 4-6 refers to rotational degrees of freedom, m_{ii} is the dry mass, m_{aii} is added mass, C_{ii} is hydrodynamic drag coefficients, m^*_{ii} is inertial load coefficients containing the effect from the displaced water volume, u_x-u_z are the body displacements in the respective DOFs, θ_x-θ_z are the body rotations around the respective DOFs and w_x-w_z are the hydrodynamic particle displacements in the respective DOFs.
If the HCP is eccentric relative to the COG, the body motions need to be postulated with regards to the motion of HCP as shown in Equation (3.13).

$$\begin{bmatrix} u_x \\ u_y \\ u_z \end{bmatrix} = \begin{bmatrix} 1 & 0 & 0 & e_x & -e_y & \\ 0 & 1 & 0 & -e_z & 0 & e_x \\ 0 & 0 & 1 & e_y & -e_x & 0 \end{bmatrix} \begin{bmatrix} u^0_x \\ u^0_y \\ u^0_z \\ \theta_x \\ \theta_y \\ \theta_z \end{bmatrix} \quad (3.13)$$

Where u_x - u_z the motions of the HCP, Where u^0_x - u^0_z the motions of the COG and e_x - e_z are the the distance between the two in the respective axial directions (Sævik 2017b).

3.3.3 Sea150

Sea150 is an element used to simulate sea properties, represented by an arbitrary set of 4-nodes forming a shell element. All elements connected to such an element are subjected to buoyancy, current and wave forces if defined. The current is described with a velocity and direction for a range of depths forming a profile by the use of interpolation between the points. Both regular waves with a specified direction, heights period and phase as well as irregular waves based on a spectrum can be applied. Corresponding loading can then be applied for cylindrical shapes calculated by the use of Morrison's equation. Current and wave loading can be scaled over time by the use of a time history.

3.3.4 Spring137

Spring137 is a 12 DOF element connecting two nodes. Material characteristics can be described in all 6 DOFs to determine forces and moments relating to the relative motion of the two nodes (Sævik 2017b).

3.4 Incremental solution procedures for virtual displacements

To solve Equation 3.18 one need to use iterations. The two most widely used procedures are the total Lagrange and the updated Lagrange formulation. The difference between these two formulations is the fact that the total Lagrange uses the initial configuration (C_0) variables while the updated Lagrange uses the latest equilibrium condition (C_n). This is shown in Figure 3.4.

In the SIMLA software a further developed version of the updated Lagrange solution procedure called a co-rotational formulation is used. Here a local coordinate system is attached to each element, following the motions of the element as it deforms. This makes it possible to separate nonlinearities arising from large displacement from nonlinearities within the elements (Sævik 2017b).

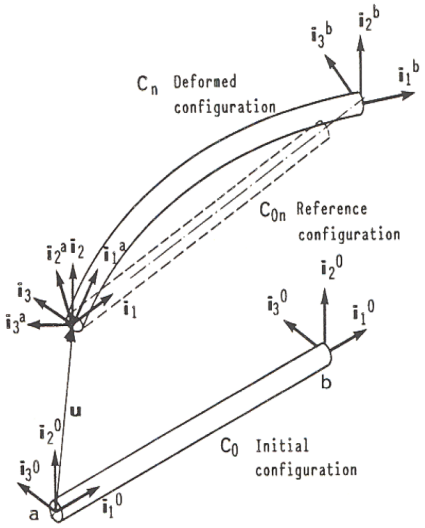

Figure 3.4: Reference frames (Sævik 2017b)

3.5 Contact kinematics

Contact kinematics is an essential non-linear effect for trawling simulations, which is applied to the SIMLA model through contact elements.

Let a contact element be defined between two bodies A and B, which occupies a region V^l with a boundary S^l where l = A,B. Contact occur if the displacement field $\boldsymbol{u}^l = \boldsymbol{u}^l(x^l)$ within a time interval $[t, t + \Delta t]$ lead to the two surfaces meeting. This surfaces meet if $S_c = v^A \cap v^B$ and $S^l = S^l_\sigma + S^l_u + S^l_c$, where S^l_σ denotes the part of the surface with prescribed surface tractions $\boldsymbol{T}^l$ and S^l_u denotes the part of the surface with prescribed displacements. $\boldsymbol{n}$ is the normal vector facing outwards of the body A at $\boldsymbol{X} \in \boldsymbol{S}^l_c$ and $\boldsymbol{t}$ are the corresponding tangent vector. At the beginning of a time increment Δt, the initial gap g^*_0 at $\boldsymbol{n} \in \boldsymbol{S}^l_c$ in the direction of $\boldsymbol{n}$ is defined as:

$$g^*_0 = (\boldsymbol{x}^B - \boldsymbol{x}^A) \cdot \boldsymbol{n} \tag{3.14}$$

Where $\boldsymbol{x}^A$ and $\boldsymbol{x}^B$ are the updated coordinates of a point at time t. After a time increment Δt, there may still be a gap opening if the criterion in Equation 3.15 is satisfied, or contact is established if the following is fulfilled:

$$g^* = (\delta \boldsymbol{u}_B - \Delta \boldsymbol{u}_A) \cdot \boldsymbol{n} + g_0 > 0 \tag{3.15}$$

$$g^* = (\delta \boldsymbol{u}_B - \Delta \boldsymbol{u}_A) \cdot \boldsymbol{n} + g_0^* = 0 \tag{3.16}$$

Where g^* is the gap at time t + Δt in the direction of $\boldsymbol{n}$. Further, if contact has been established there may occur slipping and therefore also friction work if the following is fulfilled:

$$\gamma = (\delta \boldsymbol{u}_B - \Delta \boldsymbol{u}_A) \cdot \boldsymbol{t} + \gamma_0 \neq 0 \tag{3.17}$$

Where $\boldsymbol{t}$ is the tangent vector pointing towards the Body B.
The contact force is defined by applies a stiffness penalty using interaction curves which can be defined in normally and tangentially to the contact point.

Specific kinematic properties between elements may be applied through various contact elements. The various contact elements used in the SIMLA model described in section 4 is described below.

3.5.1 Cont153

Cont 153 is a three-noded contact elements with 18 DOFs used to describe contact between pipe elements and three-dimensional body elements. The three nodes defining the element consist of the body element node and two nodes of the pipe element. The geometry connected to the body node is based on a triangle as shown in Figure 3.5(a), where the contact surface is indicated in green. A continuous description of the contact geometry is achieved by an applied corner edge radius RB. Therefore, the contact surface is only defined along this radius from the the triangle sides and corners, and consequently there exist no contact surface at the top and bottom of the triangle.

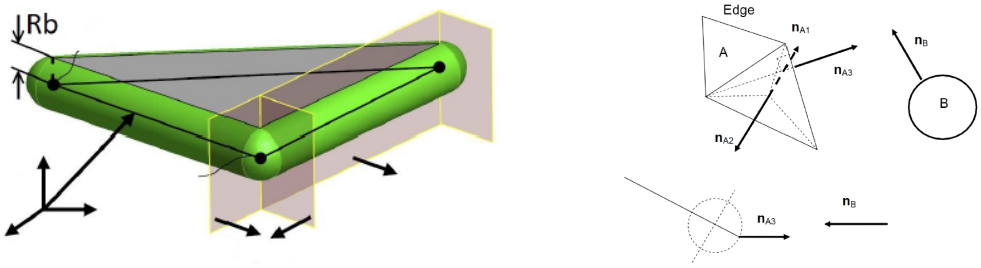

(a) (b)

Figure 3.5: Clump weight model

For a general body geometry, the master body A can come into contact with body B in three possible ways:

- In the plane of the plate at side 1, with it's surface normal $\boldsymbol{n}_{A1}$
- The the plane of the plate at side 2, with it's surface normal $\boldsymbol{n}_{A2}$
- At the edge of the plate, with it's surface normal $\boldsymbol{n}_{A3}$

The normal vectors are shown in Figure 3.5b, where the $\boldsymbol{n}_{13}$ is determined by rotating it along the circumference of a virtual circle marked in the figure.

3.5.2 Cont126

Cont126 is a one-noded contact element which used to describe contact with the sea bottom in this thesis. When the gap g^* is negative, contact forces are established by combining friction factors and soil material curves as described in Chapter 4.3. The element also include torsion moment due to axial rotation and transverse displacement.

3.6 Static analysis

For a linear static problem, the stiffness contributions from all elements can be assembled into a global stiffness matrix, which can be used to solve for the displacements directly. This is not possible for a geometrical non-linear analysis this is not possible though, as the stiffness of an element depends on the deformed shape. Therefore it is necessary to implement a incremental method to find the stiffness matrix. The goal is to fulfill equilibrium between internal and external energy. As it is impossible to find the exact solution by means of numerical iterative procedure, one need to set a tolerance level where the difference between internal and external energy is sufficiently small. Energy equilibrium is expressed in terms of the Principle of virtual displacements.

$$\int_{V_{0n}} (\boldsymbol{C}^m : \Delta \boldsymbol{E}) : \delta \boldsymbol{E} dV + \int_{V_{0n}} \boldsymbol{S} : \delta \Delta \boldsymbol{E} dV - \int_{\partial V_{0n}} \Delta \boldsymbol{t} \cdot \delta \boldsymbol{u} dS - \int t \cdot \delta \boldsymbol{u} (\Delta dS) = 0 \tag{3.18}$$

Where C^m is the elasticity tensor, S is the 2^{nd} Piola-Kirchoff stress tensor, E is the Green strain tensor, δ virtual displacement and Δ is the increment between two configurations.

The two first term in equation 3.18 express the internal energy and consist of a initial and a incremental stiffness term. The two following terms represent the energy from an external load. The strain increment is found through the equilibrium condition, which can be solve if combine with the kinematic relation and material law. From the resulting expression the tangential stiffness can be derived as:

$$\boldsymbol{k}_T = \boldsymbol{k}_m + \boldsymbol{k}_\sigma \tag{3.19}$$

As SIMLA uses a co-rotated formulation, the stiffness of each element need to be transformed from the local coordinate system to the global system. This is done by multiplying with the transformation matrix $\boldsymbol{T}$:

$$\bar{\boldsymbol{k}}_I = \boldsymbol{T}^T \boldsymbol{k}_I \boldsymbol{T} \tag{3.20}$$

where $\bar{\boldsymbol{k}}_I$ and $\boldsymbol{k}_I$ are the global and local element stiffness respectively.

Assembling the global stiffness matrix, $\boldsymbol{K_T}$ then can be used to relate the increment in forces, $\Delta \boldsymbol{R}$ to the increment in displacements $\Delta \boldsymbol{r}$

$$\boldsymbol{K}_T \Delta \boldsymbol{r} = \Delta \boldsymbol{R} \tag{3.21}$$

Based on the general properties in the system, either incrimination of displacements, forces or a combination can be used to find the next equilibrium step.

3.7 Dynamic analysis

In a dynamic analysis motions and accelerations are enabled such that inertia forces need to be added into the equilibrium equation. The total equilibrium equation can then be written as:

$$\boldsymbol{M}\ddot{\boldsymbol{r}} + \boldsymbol{C}\dot{\boldsymbol{r}} + \boldsymbol{R}_I = \boldsymbol{R}_E \tag{3.22}$$

Where the $\boldsymbol{M}$ is the global mass matrix, $\boldsymbol{K}$ is the global stiffness matrix, $\boldsymbol{C}$ is the damping matrix, $\boldsymbol{R}_I$ is the internal loads and $\boldsymbol{R}_E$ are the external loads.

The mass local consistent mass matrix can be found as:

$$m = \int_{V_0} \rho_s \boldsymbol{N}^T \boldsymbol{N} dV \tag{3.23}$$

Where ρ_s is the structural density, $\boldsymbol{N}$ is the shape functions used to describe the displacements within the element. The global mass matrix can then be assembled as:

$$\boldsymbol{M} = \sum_i \boldsymbol{a}_i^T \boldsymbol{m}_i \boldsymbol{a}_i \tag{3.24}$$

Where $\boldsymbol{a}$ is the transformation matrix between local and global displacements(**langen˙dynamisk˙1999**).

For a linear dynamic problem modal superposition can be used to solve the response problem. This also allow for the use of Reyleigh damping, where the damping matrix can be expressed by a linear relation with the mass matrix and stiffness matrix. In SIMLA there is also added an independent diagonal stiffness matrix, $\boldsymbol{C}_0$.

$$\boldsymbol{C} = \boldsymbol{C}_0 + \alpha_1 \boldsymbol{M} + \alpha_2 \boldsymbol{K} \tag{3.25}$$

For a non-linear analysis the superposition principle is not applicable, but it can be shown that the Rayleigh damping still can be introduced to damp out high frequency modes by the means of the stiffness proportional damping term. In addition on can include a lumped damping expressed by the C_0 (Sævik 2017b). The damping model the is applied to the SIMLA model is further explained in Chapter 4.4.

3.8 incremental time integration scheme

For a dynamic analysis there will be variations in time, which can be discretized into time steps. As it is not possible to use modal superposition in a nonlinear analysis, it is necessary to apply time integration of the equations of motion. This can either be done by explicit methods or implicit methods.

Explicit methods uses information of the current time step to determine the deformation at the next time step. This method is only conditionally stable and therefore very small time steps are needed to ensure good results. It is therefore most used for explosion- and collision simulations. The advantage of such a method is that the computation time for each time step is low in comparison to implicit methods.

Implicit methods uses both unknowns in the next step and information in the current time step to determine the successive displacement. This makes the method more numerical stable, but at the cost of computation power as the next time step need to be found by iterative methods.

In SIMLA the HHT-α method is used in the time integration scheme (Sævik 2017b). The method presented in this section is based on the PhD thesis of Kjell Mange Mathisen (Mathisen 1990). The HHT-α method the modified equation for the system given as:

$$\boldsymbol{M}\ddot{\boldsymbol{r}} + (1+\alpha)\boldsymbol{C}\dot{\boldsymbol{r}}_{k+1} - \alpha\boldsymbol{C}\dot{\boldsymbol{r}}_k + (1+\alpha)\boldsymbol{R}^I_{k+1} - \alpha\boldsymbol{R}^I_k = (1+\alpha)\boldsymbol{R}^E_{k+1} - \alpha\boldsymbol{R}^E_k \tag{3.26}$$

The acceleration and velocity at the time step k+1 is found using the same formulas as in the Newman-β method:

$$\Delta\ddot{\boldsymbol{r}}_{k+1} = \ddot{\boldsymbol{r}}_{k+1} - \ddot{\boldsymbol{r}}_{k+} = \frac{1}{\Delta t^2\beta}\Delta\boldsymbol{r}_{k+1} - \frac{1}{\boldsymbol{\Delta t}\beta}\dot{\boldsymbol{r}}_k - \frac{1}{2\beta}\ddot{\boldsymbol{r}}_k \tag{3.27}$$

$$\Delta\dot{\boldsymbol{r}}_{k+1} = \dot{\boldsymbol{r}}_{k+1} - \dot{\boldsymbol{r}}_{k+} = \frac{\gamma}{\Delta t\beta}\Delta\boldsymbol{r}_{k+1} - \frac{\gamma}{\beta}\dot{\boldsymbol{r}}_k - \boldsymbol{\Delta t}(\frac{\gamma}{2\beta} - 1)\ddot{\boldsymbol{r}}_k \tag{3.28}$$

By subtracting the equilibrium equation at time step k from equation 3.26 the following relation can be found:

$$\hat{\boldsymbol{K}}_k\Delta\boldsymbol{r}_{k+1} = \boldsymbol{\Delta}\hat{\boldsymbol{R}}_{k+1} \tag{3.29}$$

Here the effective stiffness matrix $\hat{\boldsymbol{K}}_k$ is:

$$\hat{\boldsymbol{K}}_k = a_0\boldsymbol{M} + \boldsymbol{c}_0\boldsymbol{C} + \boldsymbol{b}_0\boldsymbol{K}_{T,k} \tag{3.30}$$

$$a_0 = \frac{1}{\Delta t^2\beta} + (1+\alpha)\frac{\alpha_1\gamma}{\Delta t\beta} \tag{3.31}$$

$$c_0 = (1+\alpha)\frac{\gamma}{\delta t\beta} \tag{3.32}$$

$$b_0 = (1+\alpha)\frac{\alpha_2\gamma}{\Delta t\beta} \tag{3.33}$$

The effective load vector $\Delta\hat{\boldsymbol{R}}_{k+1}$ it given as:

$$\Delta\hat{\boldsymbol{R}}_{k+1} = (1+\alpha)[\boldsymbol{R}^E_{k+1} - \boldsymbol{R}^E_k + \boldsymbol{C}\boldsymbol{b}^E_k] + \boldsymbol{M}\boldsymbol{a}_k + \boldsymbol{R}^E_k - \boldsymbol{R}^I_k - \boldsymbol{C}_k\dot{\boldsymbol{r}}_k \tag{3.34}$$

$$\boldsymbol{a}_k = \frac{1}{\boldsymbol{\Delta t\beta}}\dot{\boldsymbol{r}}_k + (\frac{1}{2\beta} - 1)\ddot{\boldsymbol{r}}_k \tag{3.35}$$

The displacement at the next time step can be found by solving equation 3.29 and further the acceleration and velocity can be found from equation 3.27 and 3.28. Equation 3.34 accounts for unbalanced forces at time step k, such that the unbalance in forces in equation 3.26 will not be accumulated. The method will coincide with the Newman-β method if $\alpha = 0$. When the the HHY-α method is formulated for a linear undamped system in free oscillations, it will be unconditional stable for the given values of α, β and γ (Sævik 2017b):

$$-\frac{1}{3} < \alpha < 0 \quad , \quad \gamma = \frac{1}{2}(1-\alpha) \quad , \quad \beta = \frac{1}{4}(1-\alpha)^2 \tag{3.36}$$

3.9 Equilibrium iteration scheme

For each step it is necessary that the equilibrium in equation 3.26 is fulfilled. This is done through an iterative procedure as follows:

$$\hat{\boldsymbol{K}}^i_k\delta\boldsymbol{r}^{i+1}_{k+1} = (1+\alpha)(\boldsymbol{R}^E_{k+1} - \boldsymbol{R}^{I,i}_{k+1} - \boldsymbol{C}\dot{\boldsymbol{r}}^i_{k+1}) - \boldsymbol{M}\ddot{\boldsymbol{r}}^i + \alpha(\boldsymbol{R}^E_k - \boldsymbol{R}^I_k - \boldsymbol{C}\dot{\boldsymbol{r}}^i_k) \tag{3.37}$$

Where $\hat{\boldsymbol{K}}$ is the effective stiffness matrix given in equation 3.30, and the right hand side of the equation account for the unbalance in inertia, damping internal forces.
The increment in the acceleration and velocity vectors is found through the contribution terms in equation 3.27 and equation 3.28. The updating process can be summarized as:

$$\Delta\boldsymbol{r}^{i+1}_{k+1} = \Delta\boldsymbol{r}^i_{k+1} + \delta\boldsymbol{r}^{i+1}_{k+1} \tag{3.38}$$

$$\Delta\dot{\boldsymbol{r}}^{i+1}_{k+1} = \Delta\dot{\boldsymbol{r}}^i_{k+1} + \frac{\gamma}{\boldsymbol{\Delta t}\beta}\delta\dot{\boldsymbol{r}}^{i+1}_{k+1} \tag{3.39}$$

$$\Delta\ddot{\boldsymbol{r}}^{i+1}_{k+1} = \Delta\ddot{\boldsymbol{r}}^i_{k+1} + \frac{\gamma}{\boldsymbol{\Delta t^2}\beta}\delta\ddot{\boldsymbol{r}}^{i+1}_{k+1} \tag{3.40}$$

To improve the convergence rate, the tangent stiffness matrix $\hat{\boldsymbol{K}}$ should also be updated for each iteration cycle. If this is kept constant, then the procedure is called modified Newton-Rapson.
When the the right hand side of equation 3.37 falls below a certain tolerance level, then one can decide that equilibrium is achieved. The norm can for instance be based on total displacements:

$$||\delta\boldsymbol{r}^{i+1}_{k+1}|| < \epsilon_D||\boldsymbol{r}^{i+1}_{k+1}|| \iff ||\boldsymbol{r}^{i+1}_{k+1}|| - ||\boldsymbol{r}^i_{k+1}|| = \frac{1}{N}\sqrt{\sum_{j=1}^{N}(\boldsymbol{r}^{i+1}_j)^2} \tag{3.41}$$

The tolerance ϵ_D need to be specified by the user and will govern the accuracy of the solution. If SIMLA cannot reach equilibrium within a preset amount of iterations, it will divide the time step and start over.
Although the norm in equation 3.41 is based on displacements, it is also possible to to use norms governed by forces, energy or all combined (Sævik 2017b).

4 Modelling

This chapter goes through the modelling choices of the SIMLA model used to produce the results presented in Chapter 5. The scripts used to generate the SIMLA input files and post-processing of the simulation results used are based on ones provided by Vegard Longva. The provided scripts have been further developed to fit the cases addressed by this thesis.

4.1 Trawl gear configuration

Figure 4.1 shows an overview of the trawl configuration from the side, while Figure 4.2 show the trawl configuration from the top.
The clump weight is connected to a towing node, located at the surface, through a warp line. The two trawl bags at each side of the clump weight are modelled by a trawl net node, each connected to the clump weight and to a trawl board node through sweep lines.

The dimensions and mass properties are based on a previous experimental tests done by SINTEF Ocean and the hydrodynamic properties of all components of the trawl gear are based on estimates from DNV-RP-H103 (DNV 2011). These properties have been left unchanged from the original model provided by Vegard Longva.

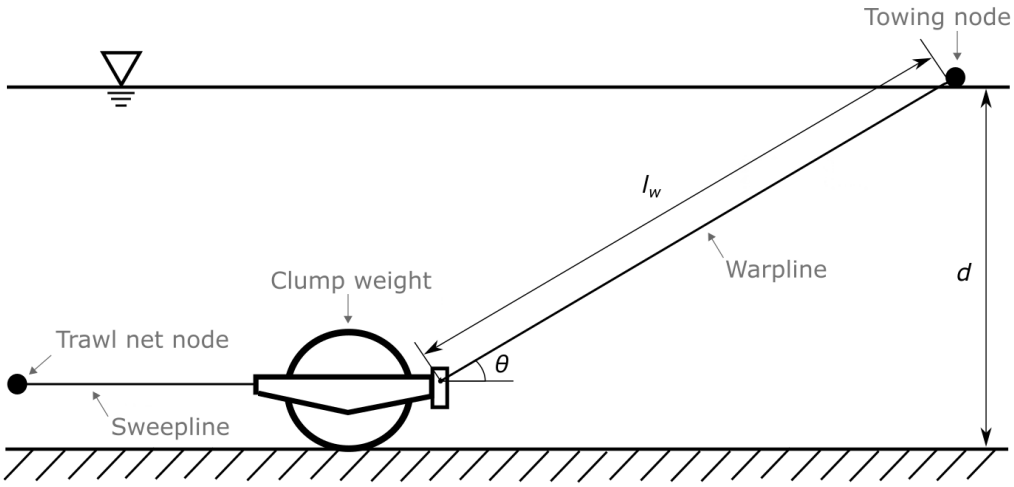

Figure 4.1: Model of clumpweight from the side

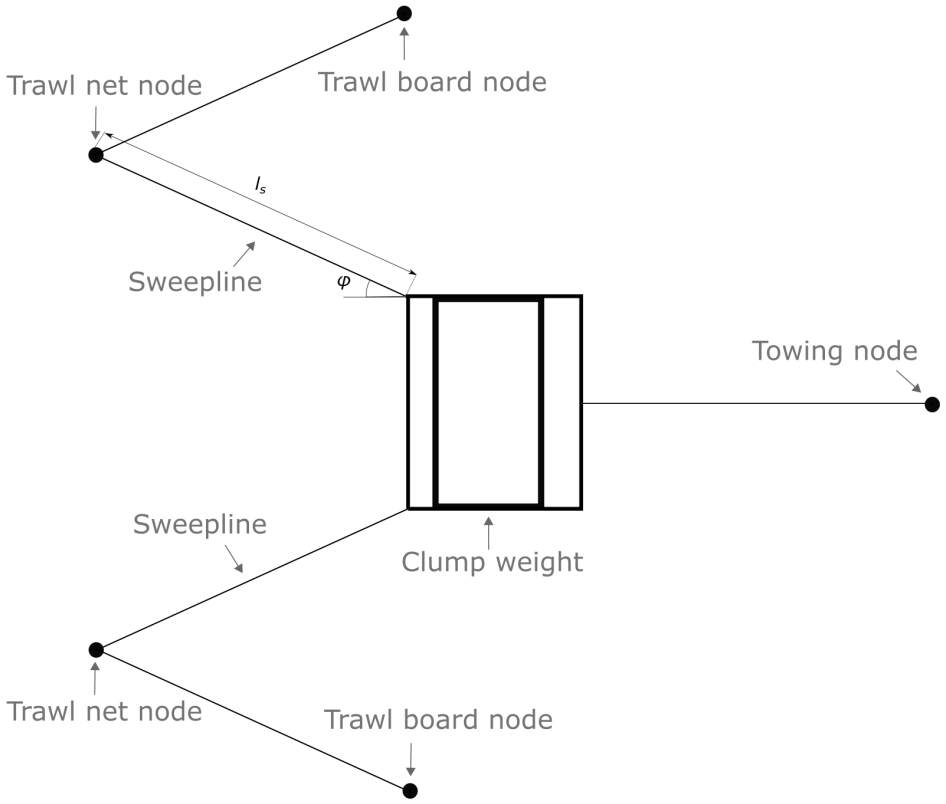

Figure 4.2: Model of clumpweight from the top

4.1.1 Towing node

The towing node represents the connection to the trawling vessel, which drives the trawl gear forward. In order to limit disturbances, rather than using prescribed displacements, the towing node is driven foreword through a point load acting on the towing node in the direction of trawling. The force is scaled over time so that there is:

1. No trawl velocity from T = 0.0 s to T = 1.0 s
2. Constant acceleration form 0 m/s to 2.4 m/s between T = 1.0 s to T = 30.0 s
3. Constant velocity from T = 30.0 s to impact with the power cable

The trawling node is constrained against translation transverse to the direction of trawling (the global x-direction) and is also connected to a fixed node with the same original coordinates as the trawl node through a spring. The spring is very stiff vertically and in the direction of trawling and it has no stiffness in the other degrees of freedom.

4.1.2 Trawl board nodes

The trawl boards in a twin trawl configuration is, just as for the clump weight, connected to the trawl vessel through warp lines. They are located far away from the point of interaction, and the connected warp lines will therefore have a negligible effect on the interaction. Because of this, they are not included in the model. The pull force from the vessel acting through these warp lines are modelled as a point load acting on the trawl board nodes instead. The force is scaled in the same manner as for the towing node, only altered by a 0.2 second lag to model the stretching of the sweep lines.

The trawl boards are modelled without mass and drag forces and are constrained against vertical motion and all rotations. They are also constrained against translation transverse to the direction

of trawling, i.e. in the global x-direction, up to T = 50 s. The constraint is meant to lift force from the trawl boards keeping the trawl bags open as the clump weight is accelerated. By allowing transverse translation of the trawl board nodes, they can follow the clump weight if it slides along the cable after impact.

4.1.3 Trawl bags

The trawl net node is connected to a body element representing the trawl bags. The body element have no mass in order exclude the possibility for compressive axial force in the sweep lines. The body element generate drag forces described by drag coefficients and have a small inertia about the z-axis as shown in Table 4.1. The trawl net node is constrained against vertical translation and all rotational degrees of freedom, and the connected sweep line are constrained to follow the translations of the trawl net node.

Table 4.1: Trawl net body element properties

Description	**Symbol**	**Value**	**Unit**
Drag coefficient, x-direction	C_{11}	37.0	m^2
Drag coefficient, y-direction	C_{22}	10.0	m^2
Dry mass, z-rotation	m_{66}	10.0	kgm^2

4.1.4 Warp line

According to DNVGL the length of the warp line is normally between 2.5 to 3.5 times the water depth (DNVGL 2017). The water depth is assumed to be 200 m and the warp line length 600 m with an initial vertical angle $\theta = 19.5°$.

The warp line model is split into two parts. The 40 meters of the line closest to the clump weight is split into shorter linear pipe elements of length 0.15 m while the rest of the warp line has 3.5 long linear pipe elements. The refined mesh close to the clump weight is in accordance with the original trawl gear model developed by Vegard Longva, which was intended for interaction with pipelines with free spans. The implication would be that the warp line came in contact with the pipeline before the clump weight would, resulting in the warplane needed to be fitted with contact elements and be able to be bent around the pipeline. As the effect of free spans are not studied in this thesis, the cable will not be in contact with the warp line.

A complete overview of the warp line model properties are shown in Table 4.2.

Table 4.2: Warp line model specifications

Description	**Symbol**	**Value**	**Unit**
Length	l_w	600	m
Diameter	d	19	mm
Axial stiffness	EA	58.34	MN
Bending stiffness	EI	4.0	kNm^2
Torsional stiffness	GJ	3.0	kNm^2
Dry mass	m_d	8.9	kg/m
Submerged mass	m_s	7.74	kg/m
Radial added mass coefficient	$C_{a,r}$	2.0	-
Tangential added mass coefficient	$C_{a,t}$	1.0	-
Radial drag coefficient	C_d, r	1.6	-
Tangential drag coefficient	$C_{d,t}$	0.1	-

4.1.5 Sweep lines

The sweep lines spanning between the clump weight and the trawl nets, and between the trawl net and the trawl boards are modelled with a single linear pipe element, each having a length of 80 meters and are stretched out with an horizontal angle of $\theta = 27.5°$. An overview of the sweep line properties are shown in Table 4.3.

Table 4.3: Sweep line model specifications

Description	Symbol	Value	Unit
Length	l_w	40	m
Diameter	d	12.5	mm
Axial stiffness	EA	52.83	MN
Bending stiffness	EI	4.0	kNm^2
Torsional stiffness	GJ	4.0	kNm^2
Dry mass	m_d	3.85	kg/m
Submerged mass	m_s	0.0	kg/m
Radial added mass coefficient	$C_{a,r}$	2.0	-
Tangential added mass coefficient	$C_{a,t}$	1.0	-
Radial drag coefficient	C_d, r	1.0	-
Tangential drag coefficient	$C_{d,t}$	0.0	-

4.1.6 Clump weight

The clump weight used for the simulations is a Thymorøn roller type, which previously have been used for trawl-pipeline interaction model tests. The clump weight SIMLA model is shown from the front and side in Figure 4.3. The roller barrel is modeled by eight linear pipe elements and is connected a frame of linear pipe elements with a smaller diameter. The remaining parts indicated with a green color 4.3 are modelled with body elements. The warp line is connected to the bracket in front of the clump weight, and the two sweep lines leading to the trawl net nodes are connected to the corners at the back. The mass, added mass and drag properties of the clump weight are modelled through two body elements connected to the barrel and frame with properties as described in Table 4.4. The length, diameter and thickness properties listed in the table are applied to the pipe elements, while the remainder of the properties are applied to the corresponding body elements. Coupling terms between translational and rotational degrees of freedoms are here neglected. The mass matrix terms m_{11},m_{22} and m_{33} in Equation 3.12 are all equal m_s, and since the mass matrix are diagonal, naturally, all the terms outside the diagonal are equal to zero.

Contact between the barrel and the sea bottom, and between the frame and sea bottom, are established through cont126 contact elements, while the contact between the remaining body parts are established though cont153 contact elements.

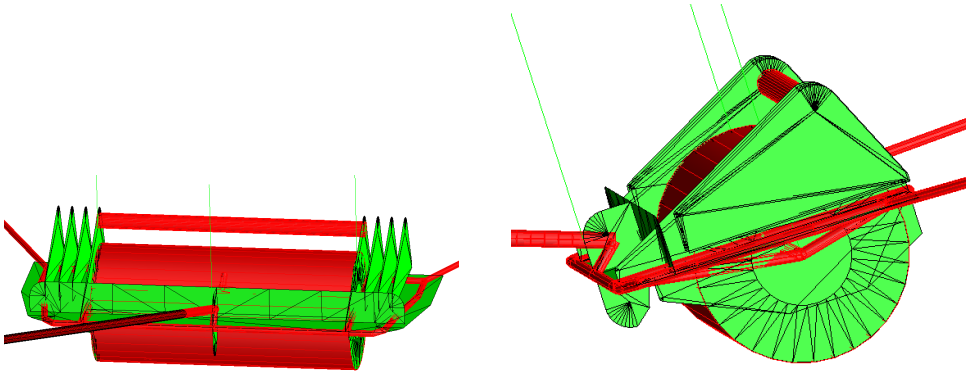

(a) Front view (b) Side view

Figure 4.3: Clump weight model

Table 4.4: Clump weight model specifications

Description	**Symbol**	**Barrel value**	**Frame value**	**Unit**
Length	l_{pipe}	1.7	Various	m
Diameter	D	770	20	mm
Steel thickness	t	20	1	mm
Axial stiffness	EA	200	200	GN
Bending stiffness	EI	20	20	GNm^2
Torsional stiffness	GJ	19	19	GNm^2
Submerged mass	m_s	4314	2115	kg
Dry mass	m_d	3524	2400	kg
Dry mass, x-rotation	m_{44}	1184	2649	kgm^2
Dry mass, y-rotation	m_{55}	382	316	kgm^2
Dry mass, z-rotation	m_{66}	1184	2662	kgm^2
Added mass coefficient, x-direction	$m_{a,11}$	0.558	0.0	m^3
Added mass coefficient, y-direction	$m_{a,22}$	0.0	0.0	m^3
Added mass coefficient, z-direction	$m_{a,33}$	0.558	0.0	m^3
Added mass coefficient, x-rotation	$m_{a,44}$	0.134	0.389	m^5
Added mass coefficient, y-rotation	$m_{a,55}$	0.0	0.048	m^5
Added mass coefficient, z-rotation	$m_{a,66}$	0.134	0.096	m^5
Drag coefficient, x-direction	C_{11}	1.034	0.0	m^2
Drag coefficient, y-direction	C_{22}	0.5	0.44	m^2
Drag coefficient, z-direction	C_{33}	1.034	0.0	m^2
Drag coefficient, x-rotation	C_{44}	0.229	1.873	m^5
Drag coefficient, y-rotation	C_{55}	0.05	0.129	m^5
Drag coefficient, z-rotation	C_{66}	0.229	0.456	m^5
COG eccentricity, x-direction	e_x	0.0	0.0	m
COG eccentricity, y-direction	e_y	0.0	0.0	m
COG eccentricity, z-direction	e_z	0.0	0.0	m

4.2 Subsea Cable

Specifications for a typical power cable was provided by my co-supervisor Erik Levold from Equinor. The provided specifications of the cable are listed in Table 4.5.

Table 4.5: Cable specifications from Equinor

Property	**Symbol**	**Value**	**Unit**
Diameter of cable	D	86	mm
Weight of cable in water	w_s	16.0	kg/m
Axial stiffness	EA	290	MN
Torsional stiffness	GJ	23	kNm^2
Bending stiffness	EI	2.3	kNm^2

Through conversations with Svein Sævik and Erik Levold it was decided that the provided cable specification need to be scaled up to about double the size to represent a realistic direct current export cable for use at the Norwegian continental shelf. As the dimensions of the layers as well as the lay angle of the fibers were not given in the original cable specification, these had to be assumed. Good compliance with regards to the provided axial, bending and torsional stiffness were obtained using:

- Two steel armour layers, with t = 3 mm and with fill factor $F_f = 0.9$
- Lay angle: $\alpha_l = 20°$
- Steel with E = 210 GPA and $\nu = 0.3$
- A single outer cable sheath with t = 10 mm and E = 4 GPa

As a power cable has the same type of of reinforcement, flexible pipeline theory can be applied to find the stiffness properties of the cable. Here the cable has been simplified to contain only the two steel armour layers and the outermost protective sheath. The axial stiffness based on these assumptions can be found using the formula:

$$EA = 2\pi \cdot R \cdot t_{tot} \cdot F_f \cdot E \cdot cos^2(\alpha_l)\ [cos^2(\alpha_l) - \nu_a\ sin^2(\alpha_l)] \tag{4.1}$$

Where ν_a is the apparent Poisson's ratio between the axial and radial strain (Sævik 2017a). It is here assumed that there are two steel layers and no torsion coupling.

Similarly, the torsional stiffness is found from the expression:

$$GJ = 2\pi \cdot E \cdot R^3 \cdot t_{tot} \cdot F_f \cdot sin^2(\alpha_l)cos^2(\alpha_l) \tag{4.2}$$

The bending stiffness of the cable consists of local bending stiffness of the steel wires, bending stiffness of the outer sheath, and friction between the cable layers. As one can expect large deformations of the cable, one can assume that the friction term can be neglected as the layers are sliding relative to each other (Sævik 2017a). Furthermore, it is assumed a linear elastic material behaviour, an assumption which is only valid if the bending radius larger than the locking radius.

$$\begin{aligned} EI_e = \ & E_c \cdot \frac{\pi}{4}[(R_c^o)^4 - (R_c^i)^4] + \frac{1}{2}\sum_{i=1}^{n_s} n_i[G_s J_s 4sin^2(\alpha_l) \\ & + EI\ cos^3(\alpha_l)cos^2(2\alpha_l) + EIcos(\alpha_l)(1 + 2sin^2(\alpha_l) + sin^4(\alpha_l)] \end{aligned} \tag{4.3}$$

Finally, the submerged weight can be found to be:

$$w_s = \sum_{j=1}^{n} = \rho_j \frac{\pi}{4}((R_j^o)^2 - (R_j^i)^2) \tag{4.4}$$

Where R_j^i and R_j^o are the inner and outer radius of layer j.

As the cable is to doubled in size the following assumptions have been made for the final cable properties:

- The total radius is doubled to $R_{tot} = 172$ mm
- Two steel armour layers, with t = 5 mm and with fill factor $F_f = 0.9$
- Lay angle $\alpha_l = 20°$
- Steel with E = 210 GPa and $\nu = 0.3$
- One single outer sheath with t = 20 mm and E = 4 GPa

Inserting the new dimensions into Equations (4.1) - (4.4) one obtain the new cable properties to be used in the analysis. These are listed in table 4.6.

Table 4.6: Final cable properties

Property	Symbol	Value	Unit
Diameter of cable	D	172	mm
Axial stiffness	EA	565	MN
Bending stiffness	EI	14.3	kNm^2
Torsional stiffness	GJ	314	kNm^2
Dry mass	m_d	88.8	kg/m
Submerged mass	m_s	34.5	kg/m
Radial added mass coefficient	$C_{a,r}$	2.0	-
Tangential added mass coefficient	$C_{a,t}$	1.0	-
Radial drag coefficient	C_d, r	0.7	-
Tangential drag coefficient	$C_{d,t}$	0.0	-

The cable is modelled with the use of linear pipe elements. This require the element length to be very refined near to the point of collision in order to correctly model the response.

4.3 Sea bottom

The sea bottom topography is defined using an input file with x,y and z coordinates. In this study, the sea bottom is chosen to be flat. There are however introduced small deviations from the water depth of 200 meters with up to 2 mm for each meter moving along the route. The small variation in the z coordinate enables the use of local maximas to efficiently establish contact points between cable and the sea floor.

The properties of the sea bottom are assigned using the COSURFPR command, which defines curve-linear routes using key points in the 2D plane. This is the standard way to determine a route in the industry as the maps have traditionally been i a 2D format. With this command, any odd numbers of routes can be specified which can be assigned separate soil properties. In this study three straight routes with the same soil properties are specified. One route is placed below the middle of the cable and two at the along the ends of the cable, all parallel to the direction of trawling.

In order to determine contact forces between the sea bottom and the power cable, and between the sea bottom and the clump weight material curves need to be established. It is necessary to establish material curves for the local vertical, axial, and transverse direction.

4.3.1 Vertical soil resistance

The vertical resistance of the soil is dependent on the penetration of the cable, which can vary over it's lifespan. A simple approximation can be to assume a linear relation between displacement and vertical force. The soils stiffness in the vertical direction is here set to be 50 KN/m for each meter of cable length. Naturally, the force displacement relation for negative penetrations will be zero. The same soil properties are used for both contact with the cable and for the clump weight roller.

4.3.2 Axial soil resistance

The axial pipe-soil response is dominated by coulomb friction and can be described by a friction factor, F_a/V. The friction factor is dependent on the type of soil and the material and roughness of the coating of the cable. The friction factor is here set to 0.3 and with a scaling factor to describe elastic-plastic soil behaviour. If one assume the soil to be undrained, i.e. there exist excess pore pressure around the pipe, the response scaling factor can be modelled with a bi-linear fit without a breakout peak. The scaling factor will therefore increase linearly until it reaches a mobilization distance x_{mob}, after which the scaling factor will be constantly equal one (**dnvgl˙dnvgl-rp-f114:˙2017**).

4.3.3 Lateral soil resistance

The lateral soil resistance of the cable consists of both coulomb friction and contact force from the berm that is generated as the cable penetrates the sea bottom. Similarly as for the axial soil interaction, the lateral soil interaction can be described using a fraction factor which is scaled based on the normal force between the soil and the cable. The force needed to move the cable through the berm is called the break out force and can be modelled by a single peak. The scaling factor can then be found by adding together a bi-linear elastic-plastic model showed in Figure 4.4 (a) with a peak representing til breakout force shown in Figure 4.4 (b). The combined scaling factor is dependent on the lateral displacement and is shown in Figure 4.5.

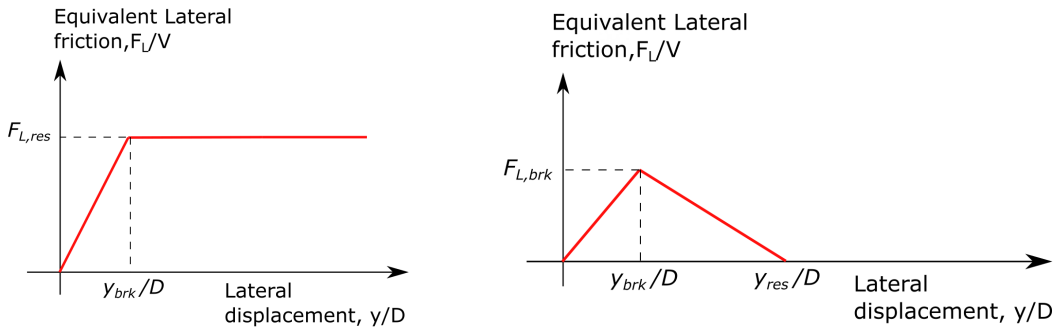

(a) Bi-linear curve describing the residual resistance

(b) Peak describing the break-out resistance

Figure 4.4: Peak and residual resistance

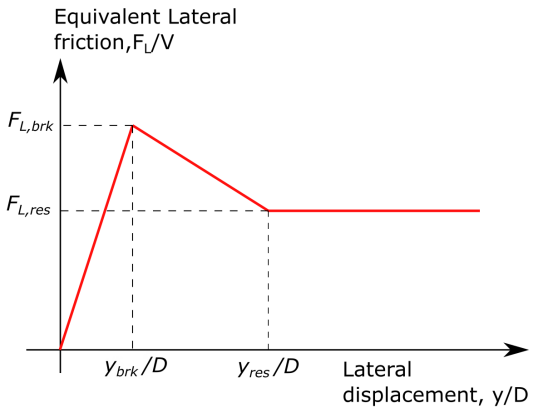

Figure 4.5: Resulting scaling factor for the equivalent lateral soil resistance

In Figure 4.4 and 4.5, $F_{L,brk}$ is the unit break force per unit length, $F_{L,res}$ is the residual unit force per unit length, y_{brk} is the lateral displacement leading to the cable breaking free of the berm and

y_{brk} is the lateral displacement, where the the scaling factor is reduced to it's residual value. V is the static vertical cable-soil force, D is the cable outer diameter including coating.

Guidance on determining the magnitude of the parameters used in Figure 4.5 can be found in DNVGL-RP-F114, which specify pipe-soil interaction for submarine pipelines. In this study, it is assumed that the cable-soil interaction is similar to pipe-soil interaction. The magnitudes used to scale the friction factor for the lateral soil interaction is shown in Table 4.7.

Table 4.7: Stress-displacement curve in the lateral direction

Displacement [m]	$\boldsymbol{F_L/V}$
0.0	0.0
0.02	1.5
0.05	1.0
1000.0	1.0

4.4 Estimation of damping

4.4.1 Structural damping

In a real structure there will arise damping forces when the structure is set in motion, which should be introduced to the model in order to obtain reasonable properties. A common method is to apply Rayleigh damping, which assume the damping to be linear dependent on the mass and stiffness matrix as shown in equation 4.5.

$$\boldsymbol{C} = \boldsymbol{C_0} + \alpha_1 \boldsymbol{M} + \alpha_2 \boldsymbol{K} \tag{4.5}$$

Where $\boldsymbol{C}$ is the damping matrix, $\boldsymbol{C_0}$ is the diagonal damping matrix, $\boldsymbol{K}$ is the stiffness matrix, $\boldsymbol{M}$ is the mass matrix and α_1 and α_2 are constants (Sævik 2017b).

Normally the mass damping contribution is low in comparison to the stiffness damping and one can assume the damping to only be dependent on the stiffness matrix such that $\alpha_1 = 0$. α_2 can then be found by using a typical value for the damping to solve Equation 4.6.

$$\xi = \frac{1}{2}(\frac{\alpha_1}{\omega} + \alpha_2 \omega) \tag{4.6}$$

Where ω is the frequency of the oscillation of the structure. (**langen˙dynamisk˙1999**)

Though conversation with Svein Sævik, who have a lot experience with modelling of slender structures, it was determined that a reasonable damping coefficient for the subsea cable is about $\xi = 0.05$. A typical pull-over duration for trawl interaction with a cable resting on the sea floor can be found to be 1 second which correspond to a quarter of a oscillation cycle, or a frequency of $\omega = \pi/2$. Inserting the values into Equation 4.6 results in $\alpha_2 = 0.06$.

4.4.2 Contact damping

The contact damping is based on the local eigenfrequency damping is and is applied between the sea bottom and the cable, between the sea bottom and the clump weight barrel. The critical damping for the contact elements can be found by the use of the formula:

$$C = 2\lambda\sqrt{(m + m_a) \cdot k_c} \tag{4.7}$$

where C is the damping coefficient, λ is the damping ratio, m is the unit length mass, m_a is the unit length added mass and k_c is the contact stiffness.

The contact damping were left unchanged from the model provided by Vegard Longva. Between the clump weight and the sea bottom, the applied contact damping is set to 17% of the critical

damping in the vertical direction, and the contact damping between the cable and the sea bottom is set to 41.6 % in the vertical direction. The applied contact stiffness is set as the vertical stiffness of the soil, and there is assumed to be no contact damping in the other DOFs. Due to the high damping and due to the inclusion of structural damping in the cable, no contact damping between the clump weight and the power cable is introduced.

4.5 Cable length sensitivity study

The length of the cable model need to have sufficient length to represent an infinitely long cable. As the cable have a low bending stiffness, most of the load applied to the cable from the clump weight will transformed into axial force. One can therefore expect there to arise large displacements before sufficient axial force has built up to counteract the trawling force. Global equilibrium require that the axial force will be balanced by the friction force between the cable elements and the sea bottom. In a sufficiently long cable model, all the axial force should therefore be absorbed by soil friction to ensure that there is no trawling forces acting at the ends of the cable model. As this will require an unreasonable long cable and hence also computational cost, springs are connected to the nodes at the end of the cable model. These are further connected to a fixed node and have a stiffness in the axial direction equal to:

$$k_{BC} = \sqrt{2 \cdot EA \cdot w_s \cdot g \cdot \mu_{axial}} \tag{4.8}$$

Where μ_{axial} is the axial friction factor.
The spring stiffness simulate the axial friction force of an infinitely long cable, which will balance out the remaining axial force in the cable ends. The stiffness transverse to the cable is harder to model with springs and the transverse action will therefore be governing the length of the cable.

Assuming a cable length of 3000 m, one can check if the shear force and transverse movement at the cable end are close to zero. Figure 4.6 show a plot of the shear force at the cable end against time for a perpendicular hit angle with a relative penetration of 63 mm and 10 kN pre-tension. One can observe a small peak in the shear force at T $\approx$ 62.0 s, about the same time where contact between the clump weight and cable is established, followed by some fluctuations most likely caused by moment ripples propagating through the cable. The maximum shear force that occur over the duration of the pull-over phase is approximately 300 kN. The transverse soil resistance model established in chapter 4.3.3 show that the force required to break out of the berm formed around the cable is equal to:

$$F_{L,brk} = 1.5 \cdot V = 1.5 \cdot 34.5 \ kg/m \cdot 9.81 \ m/s^2 \approx 508 \ kN/m \tag{4.9}$$

The shear force is hence lower than the break out force in the cable, and the transverse action on the ends of the cable is expected to be small.

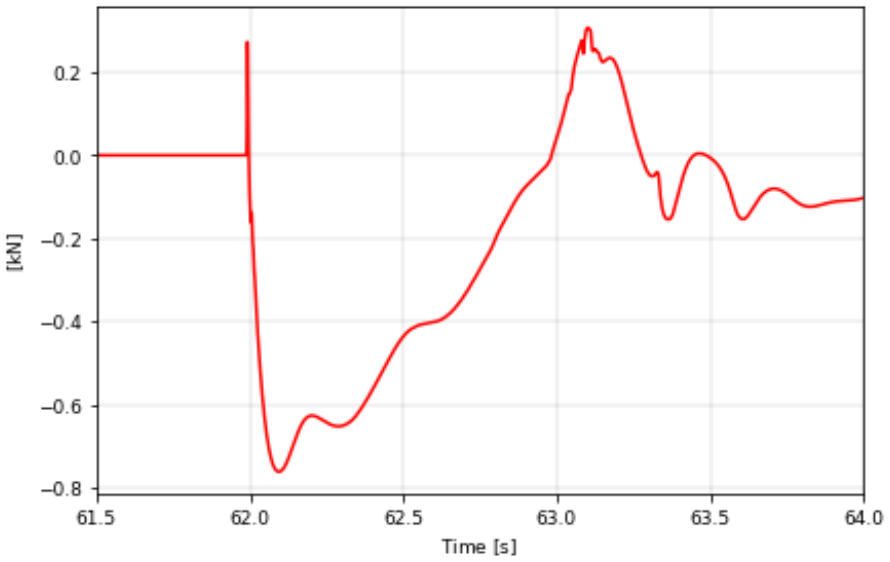

Figure 4.6: Element shear force at the end of the cable model

4.6 Mesh sensitivity study

This mesh sensitivity study were preformed as a part of the project work during the fall 2019. As there have been made several changes to the model since the study were preformed, the values of maximum axial force, maximum curvature, and maximum averaged pull-over force somewhat different form that which is obtained from the final model. Nevertheless, the behaviour of the final model is similar to the one used for the mesh convergence study and it is hence assumed that the required mesh size is the same.

In order to ensure sufficiently accuracy, it is necessary to investigate which mesh size is appropriate to achieve accurate results while keeping the computational cost to a minimum. By reducing the mesh size the results will be more accurate while the the computational cost will increase. A As the moment is the highest derivative that is of interest in the analysis, this will be the governing property of the system, and will be used to determined when the solution have converged. Table 4.8 show the moment about the z-axis at mid span of the cable, where it will be at it's maximum. The numbers are also made dimensionless and plotted as a percentage of the average in Figure 4.7. It is apparent that the result variations are quite small for mesh sizes equal or lower than the outer diameter of the cable. Therefore can one expect accurate results by setting the mesh size in the interaction area equal to the outer diameter for the cable.

Table 4.8: The relation between the mesh size and moment about the z-axis at mid span

Mesh size [-]	Largest moment [kNm]	Largest axial force [kN]	Avg. pull-over force [kN]
7 · OD	2.194	37.654	32.964
6 · OD	2.129	38.036	37.860
5 · OD	1.950	38.191	37.646
4 · OD	1.764	39.915	38.532
3 · OD	2.153	38.057	38.000
2.5 · OD	1.755	37.839	37.333
2 · OD	2.179	37.934	37.815
1.5 · OD	2.194	37.518	37.878
1.2 · OD	2.203	39.621	37.877
1 · OD	2.241	40.337	37.469
0.8 · OD	2.157	40.113	37.495
0.5 · OD	2.247	40.077	37.474
0.4 · OD	2.247	40.317	37.492
Average:	2.114	38.893	37.372

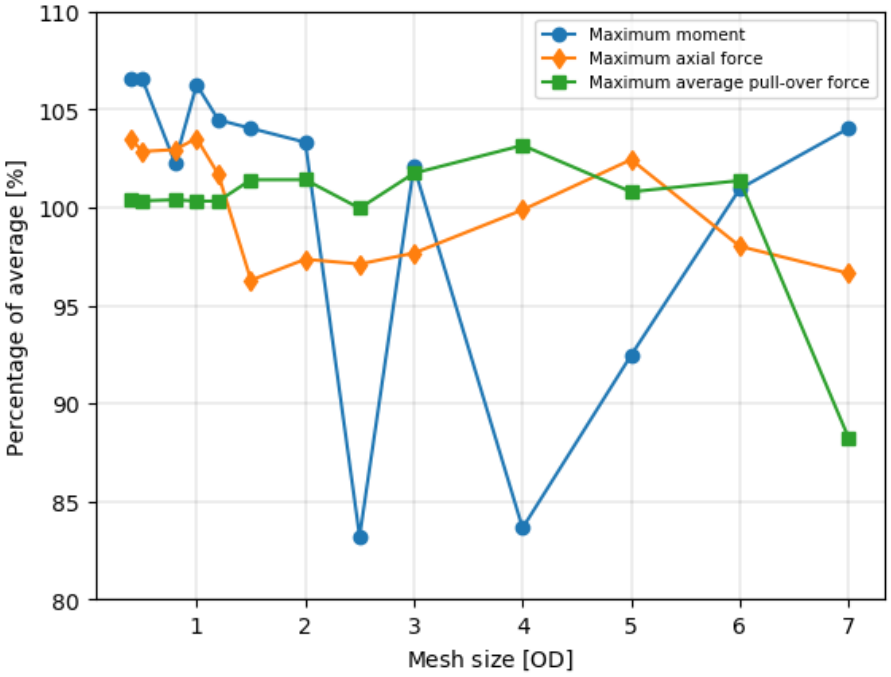

Figure 4.7: Mesh convergence

4.7 Simulation description

The simulations were split into three phases, represented by a separate input file. The three phases are as follows:

- Static on-bottom phase between T = 0.0 s to T = 0.2 s
- Dynamic acceleration phase between T = 2.0 s to T = 50.0 s
- Dynamic pull-over phase for T > 50.0

When a phase have been completed, the next is initiated by the use of a restart. The first phase focuses on establishing equilibrium between the gravity, buoyancy and contact forces with the sea

bottom. The analysis is set to be static to suppress any oscillations in the cable that can be caused by the small perturbations in the bottom surface. Further, the clump weight is accelerated up to a velocity of 2.4 m/s in the second phase, and the interaction between the cable and the clump weight occur in the third phase. The third phase vary as the time needed to cross the cable depends on the hit angle. For the cases where the clump weight is unable to cross, the third phase is terminated at T = 100 s, approximately 40 seconds after contact between the clump weight and cable has been established.
The convergence radius were set to 10^{-8} except for cases with 80° hit angle where the convergence radius had to be increased to $5 \cdot 10^{-4}$. This is further discussed in Chapter 5. Furthermore, the number of integration points over the cross section were set to be equal to 8.

The sensitivity studies to be preformed in this thesis include on the effect of hit angles, relative penetration between the clump weight and power cable, and the pretension in the cable. A case is defined as a unique combination of these parameters, resulting in 24 separate cases in total.

The hit angle is controlled placing the cable at an angle relative to the direction of trawling. Through conversations with Erik Levold at Equinor and my supervisor Svein sævik, it was decided that both very large and very small hit angles are of interest as the interactions may be significantly different from a perpendicular hit angle. The angles selected for the study include 90°, 80°, 40°, and 20°. Where 90° mean a perpendicular angle while 0° mean that the direction of trawling is parallel to the cable. As the clump weight model is symmetrical about the center line parallel to the warp line, it can be assumed that the interaction will be the same regardless if the cable is hit from the left or the right.

The vertical difference of the bottom of the roller barrel and the outer diameter of the cable, from now denoted as the relative penetration, is shown in Figure 4.8. The relative penetration is likely to be an important parameter for the interaction as it affect the distance the clump weight has be be lifted up in order to cross the cable.
The relative penetration that is caused through equilibrium between the weight of the clump weight model, drag forces when the clump weight is accelerated and the vertical contact force with the sea bottom were found to be 63 mm. In order to vary the vertical difference δ_{pen} , it is introduced an offset distance in the soil contact elements. Using a positive offset value to lift the whole cable above sea floor has been proven to be impossible with use of cont126 contact elements. To solve this, offset values are introduced contact elements both between the cable and the sea bottom and between the roller barrel and the sea bottom. The cable is therefore lowered further into the sea bottom to decrease δ_{pen} and the clump weight is lowered further to increase δ_{pen}. The introduced offset value used to change the relative penetration were chosen to be 0.05 m to introduce a significant difference in the penetration. Hence, the resulting values for δ_{pen} selected for the study include 13 mm, 63 mm, and 113 mm.

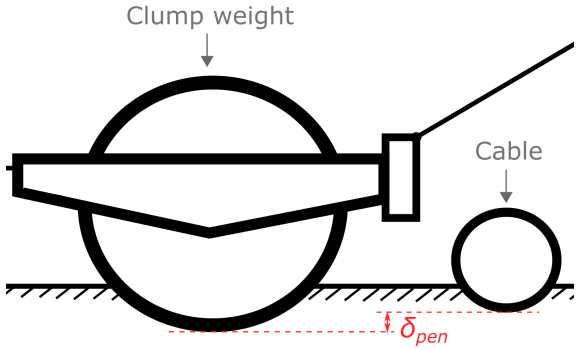

Figure 4.8: Relative vertical position at impact

During installation of a subsea cable, sufficient horizontal tension is need to ensure that the bending

radius of the cable does not fall below the design limit. This tension is preserved after installation by the axial friction between the soil and the cable sheath, and need to be taken into consideration in the SIMLA model. Based on the lay angle the bottom tension needed during installation can vary. Two different pretension cases, one with 10 KN and one with 1 kN is therefore selected. Based on the curvature limit found in chapter 2.3.3, κ_{lim}, the required bottom tension during installation can be estimated by the use of the formula for curvature at the touchdown point (TDP). The required bottom tension is found to be:

$$T_0 = \frac{w_s}{\kappa_{lim}} = \frac{34.5\ kg/m \cdot 9.81\ m/s^2}{0.45\ m^{-1}} = 752\ N \tag{4.10}$$

To ensure the bottom tension is large enough during installation, remotely operated vehicles (ROVs) are used to measure the distance from the TDP to the vessel. Because of the high uncertainty of the observation tools, a safety factor of 2-3 is applied to the required bottom tension. The most realistic case, the offshore power cable would have a pre-tension of approximately 2 kN. One can therefore expect the 1 kN case to have the most realistic behaviour.

5 Results and discussion

In this section the results from the simulations for the cases specified in chapter 4.7 carried out in SIMLA is presented. The reported properties focus on the power cable response, but the interaction between the clump weight and power cable is also described. The presented results include both horizontal and vertical pull-over force over time, axial force distribution over the length of the cable, displacement distribution in the direction of trawling and the curvature distribution. The data set used for the distributed axial force, displacement and curvature is the where the maximum of the respectively property occur.

The pull-over force is found by adding together all contact forces from the contact elements between the clump weight and power cable, where the horizontal force is the component in the direction of trawling. In order to smooth out occurring localized peaks, averaging over 100 time steps is used to estimate the pull-over forces. The vertical pull-over force is defined to be positive when directed upwards. The axial force is found as the local element force directed along the length of the element, the displacement from the global nodal displacement in the direction of trawling and the curvature is found by dividing the moment resultant from components about the local y- and z-axis divided by the bending stiffness of the cable. The moment component about the local x-axis is neglected as it is expected to be small in comparison of the ones about the y- and z-axis.

A full overview of the maximum values for all simulations can be found in Appendix A and screenshots for all hit angles in combination with δ_{pen} = 113 mm and 1 kN pre-tension can be found in Appendix B.

5.1 comparison with DNVGL-RP-F111

Figure 5.1 and Figure 5.2 show the horizontal and vertical pull-over forces respectively compared to the corresponding load pattern predicted by DNVGL-RP-F111. As indicated in the RP, only a perpendicular hit angle will be studied as it will be the most critical for design. Three different relative penetration cases are presented, which have an significant impact on both the maximum pull-over force magnitude and duration. The span height, H_{sp} is here assumed to be equal to the relative displacement δ_{pen} and the the cable displacement δ_p equal to the displacement found from the corresponding model SIMLA model. Table 5.1 show the maximum pull-over forces and durations.

Table 5.1: Comparison between DNVGL-RP-F111 and results from SIMLA

	DNVGL-RP-F111			**SIMLA model**		
$\boldsymbol{\delta_{pen}}$ $\boldsymbol{[mm]}$	$\boldsymbol{F_p}$ $\boldsymbol{[kN]}$	$\boldsymbol{F_z}$ $\boldsymbol{[kN]}$	$\boldsymbol{T_p}$ $\boldsymbol{[s]}$	$\boldsymbol{F_p}$ $\boldsymbol{[kN]}$	$\boldsymbol{F_z}$ $\boldsymbol{[kN]}$	$\boldsymbol{T_p}$ $\boldsymbol{[s]}$
13	213.5	40.8 or -42.6	2.7	37.7	-37.2	1.3
63	256.1	53.6 or -38.3	3.4	49.3	-41.9	2.0
113	293.1	64.7 or -34.6	3.8	53.4	-40.4	2.4

It is clear that DNVGL-RP-F111 overpredict load magnitude of the parallel pull-over force, with up to a 466 % increase for δ_{pen} = 13 mm. The duration is also overpredicted with up to 108 % for the same case. The season for this most likely lies in the low bending stiffness of the cable. It is stated in the RP that the document is applicable for rigid pipelines with diameters larger than 10", where the cable is flexible and have a diameter close to 7". It is clear that the cable falls outside the validity range of the RP and it is therefore not surprising that the results are not comparable.

The absolute value of the vertical pull-over force is overpredicted with 14.5 % by the RP for δ_{pen} = 13 mm, while it underpredics the force with -14.5 % for δ_{pen} = 113 mm. The reason is most likely cause by the free span value defined in the RP, which have been estimated as δ_{pen} for the SIMLA model. Due to the assumption of a free span one can expect the vertical force component to be lower when the span value is small as contact with the soil may be established, while for the SIMLA model the force will be increased with the relative penetration as the clump weight will force

is lower into the soil. One can therefore argue that the free span value should be set to zero when estimating the vertical force component to compare with the offset value used in the SIMLA model.

The vertical force component is strictly directed downwards based on the results from SIMLA. Naturally, the cable diameter is too small and vertical position not high enough to position itself higher than the centre of the clump weight. The clump weight will therefore not be able to generate an upward directed force. The positive force estimate are is therefore not relevant for this scope, but should be taken into account mainly if free spans are considered.

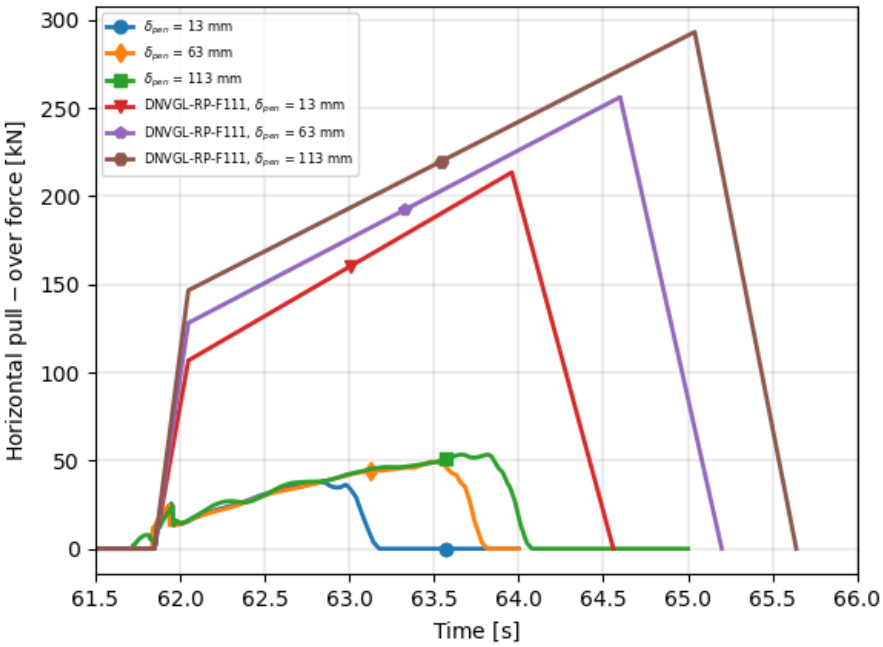

Figure 5.1: Horizontal pull-over force for a 90° hit angle and 10 kN pre-tension compared to DNVGL-RP-F111

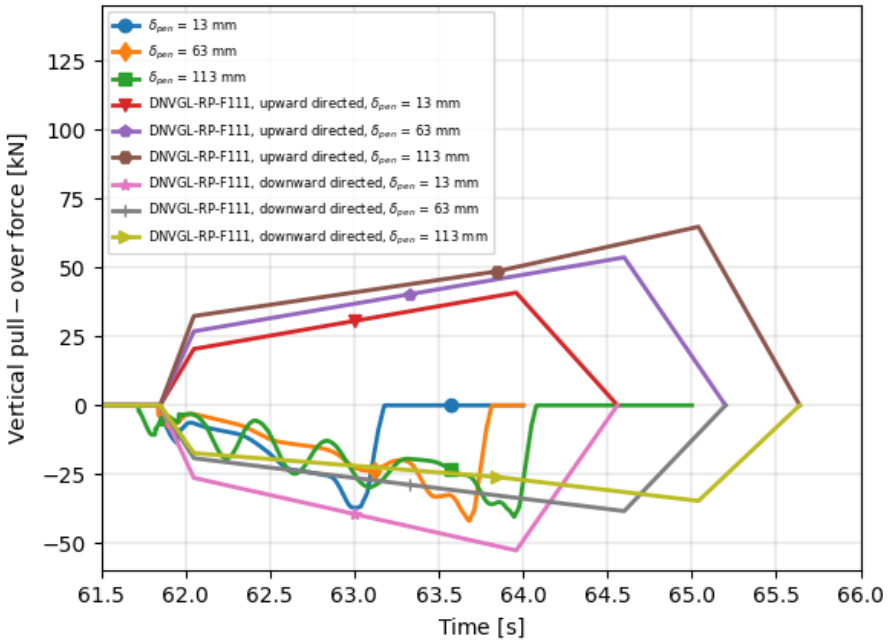

Figure 5.2: Vertical pull-over force for a 90° hit angle and 10 kN pre-tension compared to DNVGL-RP-F111

5.2 Effect of hit angle

The objective of this parameters study was to investigate the effect of the hit angle i.e. the angle between the power cable and the direction of trawling.

For a perpendicular hit angle, the clump weight is kept parallel to the power cable during the full duration of the pull-over phase. Because of the low bending stiffness of the cable, the resistance is initially low as the mid section of the cable is displaced from it's original position. As the cable gets further and further displaced, axial force in the cable builds up and offering the clump weight an increasing resistance. As the force builds up, the cable is pushed down in the soil while the clump weight is lifted and slipping occur between the two. Finally the cable bottom is forced beneath the barrel, contact ceases and the cable is dragged back due to the axial force.

For a hit angle of 80°, the left side of the roller barrel hit the cable first. Quickly after contact has been established, the clump weight start to tilt. The side which first hit the cable is lifted up while the other side is forced down into the soil as the cable is dragged along with the clump weight. When the tilt reach the critical point where one side is elevated above the top side of the cable, the contact point is quickly transferred along the barrel until the whole body is lifted above the cable.

The quick tilting motion of the clump weight caused by the 80° hit angle caused numerical issues. The time increment had to be reduced significantly and the convergence radius had to be increased to 5e-4 in order for the solution to converge. Furthermore, the number of steps used in the averaging of the pull-over force were increased from to 100 to 500 in order to reduce the jaggedness in the plot. Nevertheless, large spikes occur for some cases, such as for a hit angle of 80° combined with a relative penetration $\delta_{pen} = 113\ mm$ which is shown in Figure 5.14. This drastic loosening of the convergence radius and the large spikes in the forces make the validity of these results uncertain.

For hit angles 40° and 20°, the clump weight slides along the cable after impact. As the clump weight is sliding, the pull-over force builds up until the clump wight manage to cross in a similar manner as for a 80° hit angle. As the warp line pull force has a larger component perpendicular

to the cable for the 40° hit angle, the build up time is significantly shorter compared to that of a 20° hit angle. The combination of a 20° hit angle and a relative penetration of $\delta_{pen} = 113\ mm$ result in the horizontal pull-over force flattens out after a time and are not able to cross the cable as can be seen in Figure 5.18. The same occur if the hit angle is reduced to 10° for the studied penetration cases. In reality, small changes in the bottom topography or objects on the sea bottom may hinder the cable movement and lead to the clump weight inevitably will manage to cross the cable.
The sliding motion along the cable can damage the protective layer of the cable, especially if the edge of the clump weight barrel is sharp. If the cable is subjected to sliding repeatably, the integrity of the cable sheath may threatened and the inner layers can be exposed to the environment. Burying of the cable may therefore be necessary to ensure that this does not happen.

The trawl board nodes are not constrained against translation perpendicular to the trawl direction after T = 50 s as described in chapter 4.1.2. As the trawl nets generate drag forces which is transferred to the trawl board node through the sweep lines, there arise a force component transverse to the direction of trawling. As a consequence the trawl boards are pulled in towards the clump weigh after the translation degree of freedom transverse to the trawl direction is released.
The effect is especially prominent for the lower hit angles where pull-over duration is longer due to siding. The sliding motion also causes the clump weight to translate towards one of the trawl boards, causing the trawl net node to move over to the opposite side of the sweep line connection point. This effect will most likely increase the necessary pull-over force and the results will be on the conservative side. Nevertheless, the effect should be further studied.

5.2.1 Effect on pull-over force

Figures 5.3 and 5.4 show the time history of the horizontal and vertical pull-over load respectively. Table 5.2 show the maximum horizontal pull-over forces (MHF), maximum vertical pull-over force (MVF), time of occurrence, and percentage difference from the perpendicular hit angle for all hit angles combined with $\delta_{pen} = 63$ mm and 10 kN pre-tension.

The time of the impact occur earlier for the low hit angles as the side of the clump weight is closer to the cable after it is rotated. Upon impact between the clump weight and the cable, an force peak occur in the horizontal pull over force as shown in Figure 5.3. The magnitude of the peak is small compared to the maximum pull-over load, and is mainly of interest for checking the local integrity of the outer sheath, which is not part of the scope.
The the largest pull-over load occur when the direction of trawling is perpendicular to the cable, with a 36.7 % higher force than for a slightly lower 80° hit angle. The reason for this is that it requires more force to lift both sides over the cable simultaneously, than lifting up one side at the time. The 80° hit angle has a higher horizontal pull-over force while keeping a similar vertical pull-over force, and it has a much lower duration than the other cases.
Since a larger component of the pull-over force is perpendicular to the cable for higher-pull over angles it is natural that the 80° case build up horizontal force quicker than for the cases with lower hit angles. This, in combination with the lowering of the required force to cross with an oblique hit angle, result in a significantly shorter pull-over time compared to the other cases.

For hit angles 40°, and 20°, only the corner of the roller is in contact with the cable while sliding. This result in the maximum horizontal pull-over occurring at the just prior to the side of the clump weight reaches the top of the cable, followed by short time where the clump weight can rotate back about its vertical axis. As the clump weight turns, the component of the warp line force acting perpendicular to the cable increases, crating a new peak. This force peak yields the maximum pull-over force for a hit angle of 40°.

Providing that there only is a single point of contact, which is the case of most of the pull-over time for hit angles 40°, and 20°, the amount of contact force that is transferred into axial force increase with decreasing hit angle. This can be seen in Figure 5.6 where the maximum axial force is larger for a 20° hit angle than for a 40° hit angle. This explains why the horizontal pull-over

force is larger for 20° than for 40°.

Table 5.2: Maximum horizontal pull-over force and maximum vertical pull-over force for δ_{pen} = 63 mm and 10 kN pre-tension.

Hit angle	**Time [s]**	**MHF [kN]**	**ΔMVF**	**Time [s]**	**MVF [kN]**	**ΔMVF**
90°	63.5	49.3		63.7	41.9	
80°	62.7	31.2	-36.7 %	62.8	28.4	-32.3 %
40°	63.9	15.3	-69.0 %	63.9	28.7	-31.5 %
20°	69.1	18.6	-62.3 %	70.4	32.3	-22.9 %

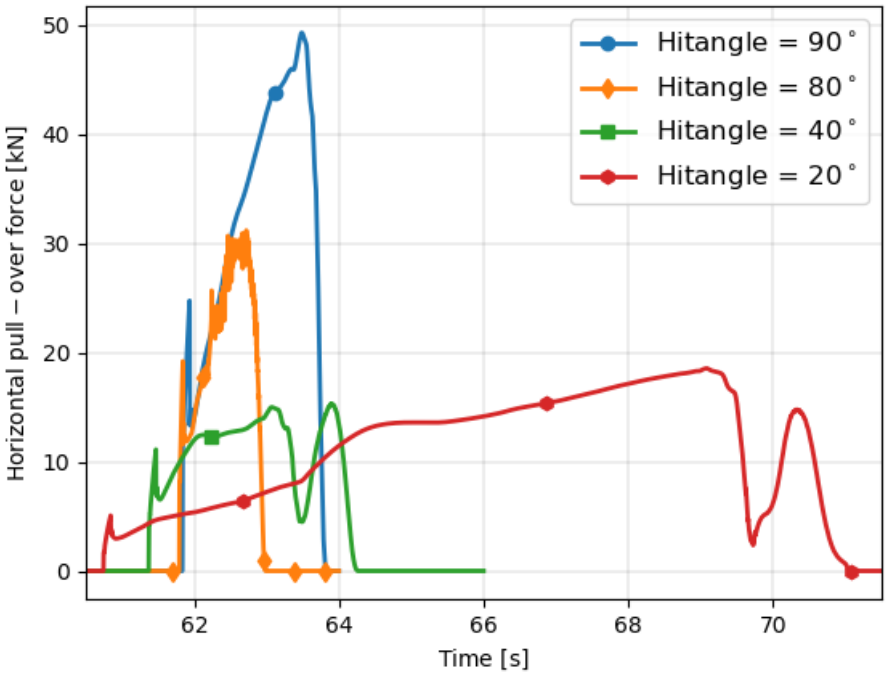

Figure 5.3: Horizontal pull-over force for δ_{pen} = 63 mm and 10 kN pretension

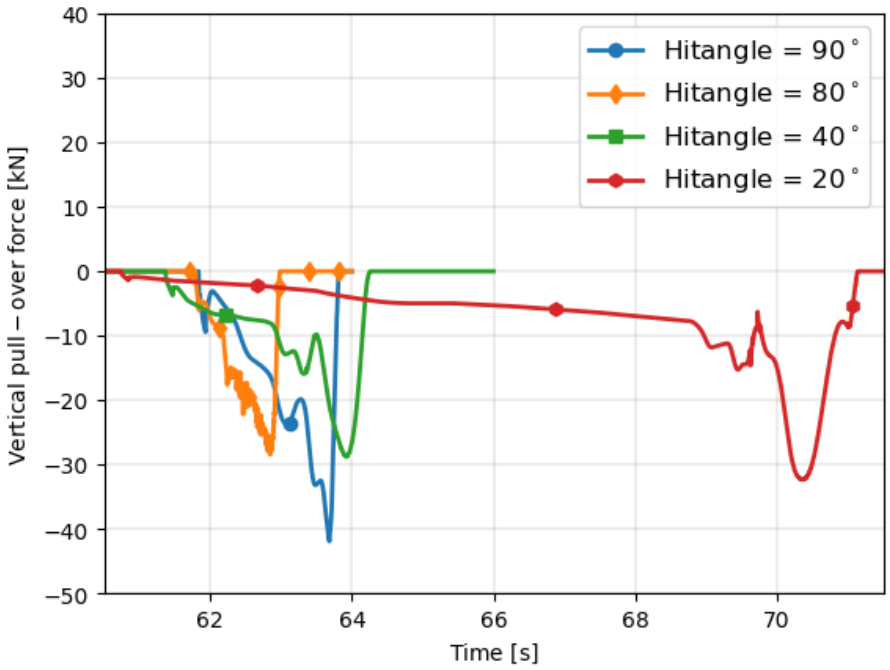

Figure 5.4: Vertical pull-over force for δ_{pen} = 63 mm and 10 kN pretension

5.2.2 Effect on axial force

Figure 5.6 show the axial force distribution over the length of the cable at the time where the maximum axial force occur, and Figure 5.5 show how the axial force is building up during the pull-over phase for a perpendicular hit angle. The maximum values, time of occurrence and the percentage deviation from the perpendicular case is shown in Table 5.3.

Just as for the pull-over load, the axial force builds up over time as the clump weight pushes the cable away from it's original position. As the forces acting along the cable increase, the friction force from the contact with the soil need to increase as well in order to maintain the equilibrium. Figure 5.5 show how the axial force spread over the length of the cable over time, activating friction force for a larger span of the cable while doing so. In addition, It can also be observed that the end force of the cable increases. This indicate that the cable model is not long enough to build up enough friction force to counteract the axial force. The springs at the ends of the cable, added to make up for the finite length of the cable, is therefore activated to absorb the residual axial force.

The largest axial force occur for a perpendicular hit angle, 45 % higher than the maximum axial force occurring for the 40° hit angle. The pull-over force is closely connected to the axial force as most of the contact force from the clump weight is transferred into axial force. As described previously, a more direct hit angle will require larger force to lift the clump weigh up over the cable, while a smaller hit angle will also reduce the amount of force that is directed perpendicular to the cable. This explains why the axial force for a 20° hit angle is larger than for 80° and 40°.

At mid span there is a jump in the axial force for the oblique trawl angles. Due the contact force from the clump weight is not directed perpendicular to the cable at mid span, and the force that is transferred to axial force will therefore be unequal distributed.

The axial force design limit which were found in chapter 2.1 shown in comparison to the occurring axial forces in Figure 5.7. It is clear that the occurring axial forces are much lower than which is required by the rules.

Table 5.3: Maximum axial force for δ_{pen} = 63 mm and 10 kN pre-tension

Hit angle	**Time [s]**	**MAF [kN]**	**ΔMAF**
90°	63.6	146.8	
80°	62.7	102.3	-30.3 %
40°	63.2	80.5	-45.2 %
20°	69.0	104.8	-28.6 %

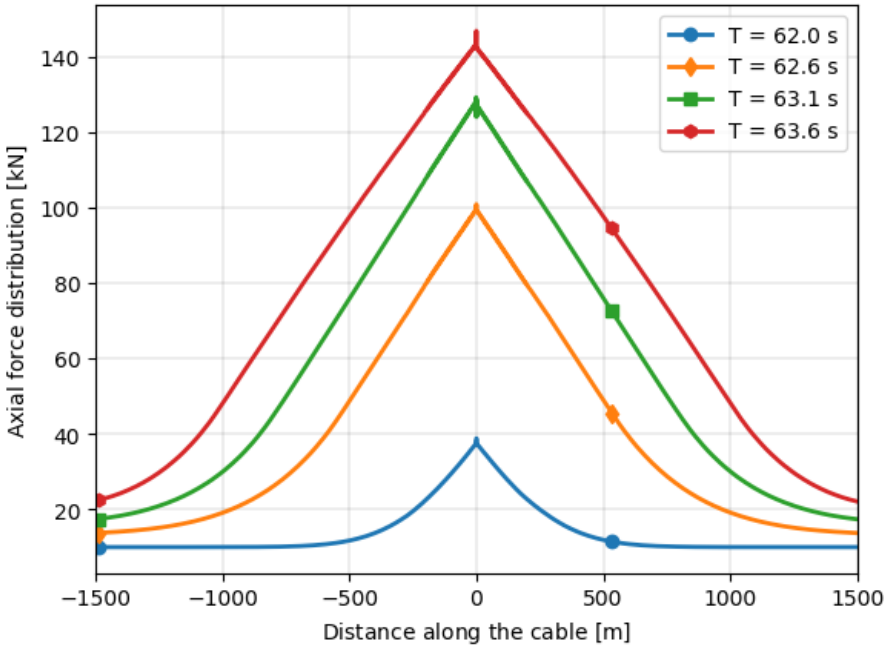

Figure 5.5: Axial force distribution history for a perpendicular hit angle, $\delta_{pen} = 63mm$, and 10 kN pre-tension

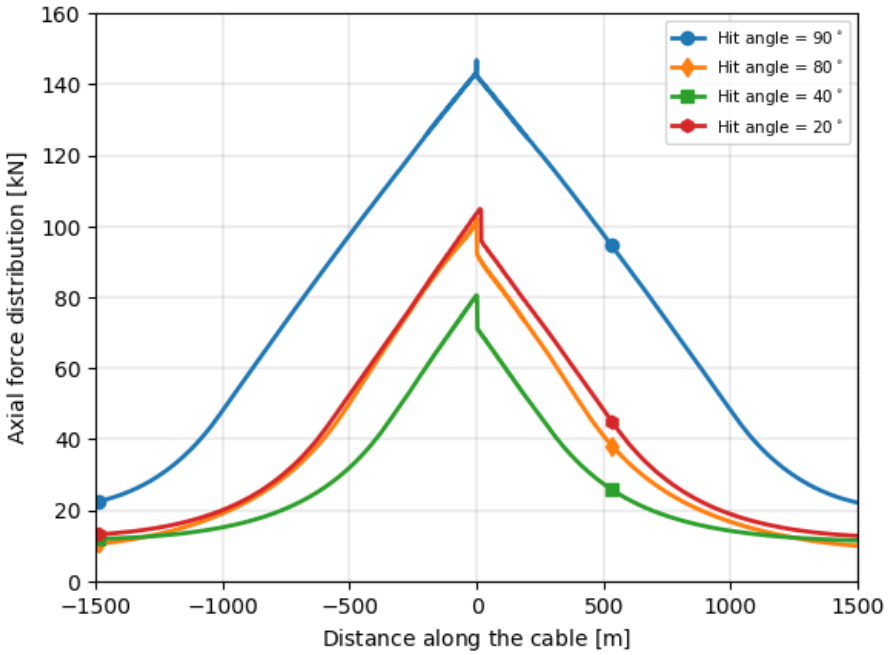

Figure 5.6: Axial force distribution for δ_{pen} = 63 mm and 10 kN pretension

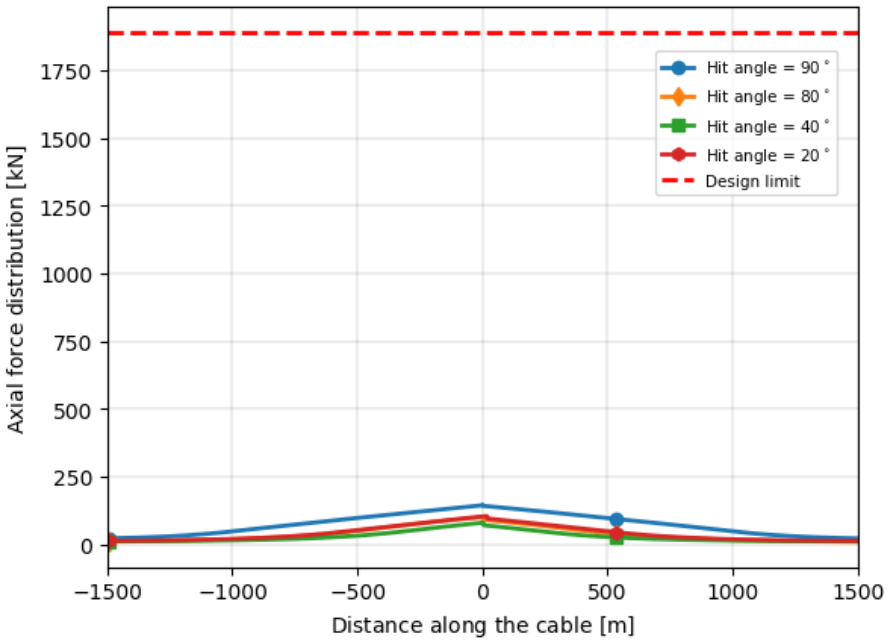

Figure 5.7: Axial force distribution for δ_{pen} = 63 mm and 10 kN pretension, including design limit

5.2.3 Effect on curvature

The curvature distribution at the time where the maximum curvature occur is showed in Figure 5.9, and the change in the curvature distribution for a perpendicular case is shown in Figure 5.8. Table 5.4 show the maximum curvature (MC), time of occurrence, and percentage difference from the perpendicular hit angle for all hit angles combined with δ_{pen} = 63 mm and 10 kN pre-tension.

It can be seen from Figure 5.8 that the curvature increases over time just as the pull-over force and the axial force, and reaches it maximum at the same time as the maximum pull-over force occur. At time 61.9, right after the impact between the clump weight and the cable, it travels a moment wave away from the point of impact due to the collision. At later time steps distribution stabilizes and the curvature is concentrated at the two peaks representing the contact points at the edges of the roller.

Figure 5.9 show that the position of the maximum varies depending on the hit angle. For hit angles 40° and 20°, the curvature peak is shifted along with the contact point between the clump weight and the cable. This is due to the sliding that occur for low hit angles. The maximum curvature occur for the perpendicular hit angle and decreases with decreasing hit angles, provided that the relative penetration is small enough for the clump weight to be able to cross the cable. This is further discussed in chapter 5.4.

The perpendicular hit angle have two peaks, one from each side of the clump weight barrel, while the other cases have a single peak due to the angle of the clump weight relative to the cable. The largest curvature occur at the contact point at the edge of the clump weight and the largest peak occur at the same time as the maximum horizontal pull-over force occur.

In theory, the two curvature peaks for the perpendicular hit angle should be equal in size due to the symmetry of the problem. However, due to the small variations in the z-coordinates along the sea bottom, the clump weight may rotate slightly over the duration of the pull-over. This can lead to small variations in the curvature about the centre of the cable, which explains the small variation in the peak values. The effect of the sea bottom on the curvature can also be seen in Figure 5.8 where small waves in the curvature can be observed at 61.8 s, before contact between the clump weight and the cable has been established.

Table 5.4: Maximum curvature for $\delta_{pen} = 63$ mm and 10 kN pre-tension

Hit angle	**Time [s]**	**MC** $[m^{-1}]$	**ΔMAF**
90°	63.5	0.311	
80°	62.1	0.299	-3.9 %
40°	63.9	0.235	-24.4 %
20°	70.5	0.230	-26.0 %

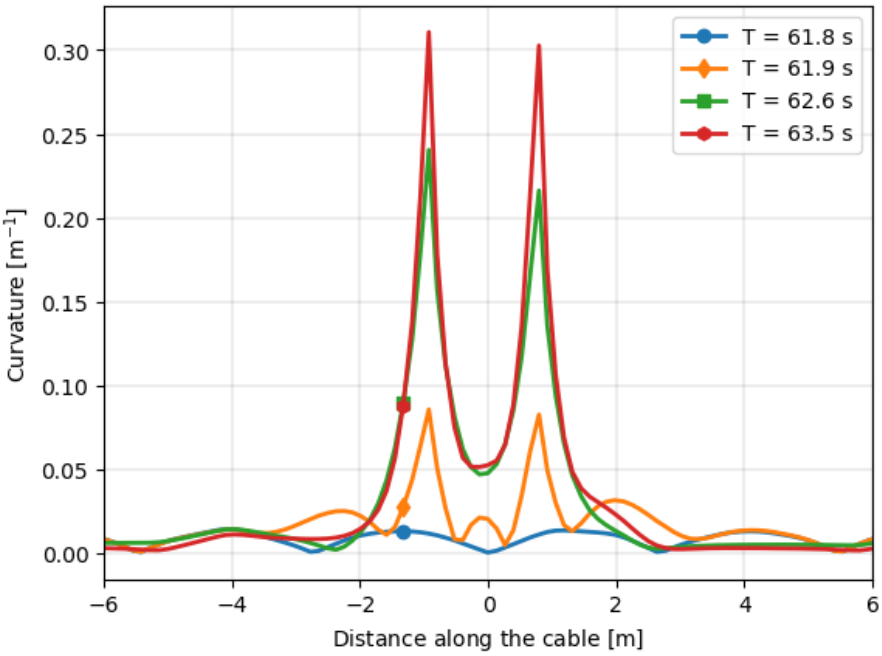

Figure 5.8: Curvature distribution history for a perpendicular hit angle, $\delta_{pen} = 63$ mm and 10 kN pre-tension

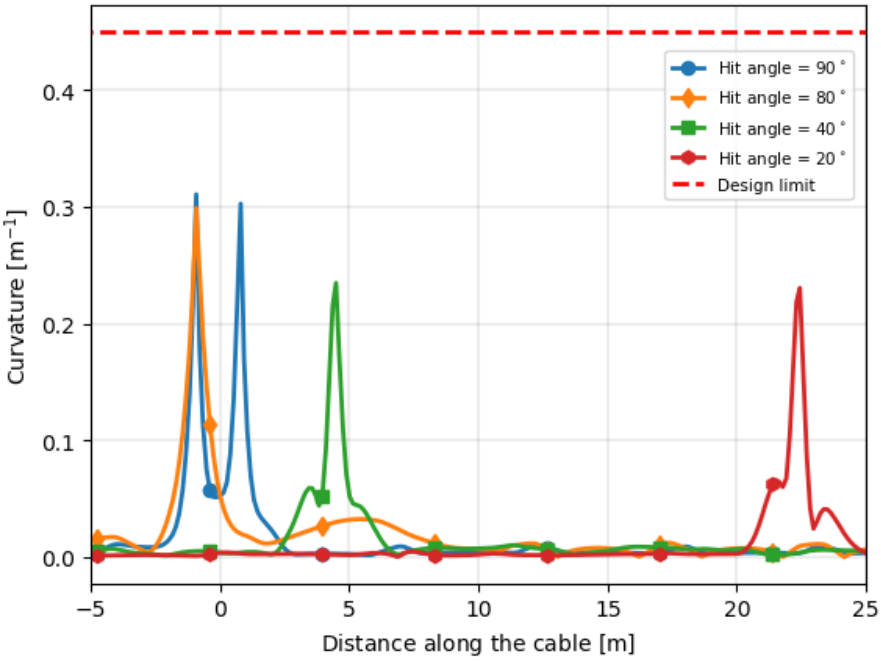

Figure 5.9: Curvature distribution for $\delta_{pen} = 63$ mm and 10 kN pre-tension, including design limit

5.2.4 Effect on displacement

The displacement distribution in the trawl direction at the time where maximum displacement occur is shown i Figure 5.11, and the change in the displacement of the displacement distribution is shown in Figure 5.10. Table 5.5 Maximum global displacement (MGD), time of occurrence, and percentage difference from a perpendicular hit angle for all hit angles combined with $\delta_{pen} = 63$

mm and 10 kN pre-tension.

It is apparent from Figure 5.10 the displacement of the cable is concentrated around the contact point the clump weight. This is due to the low bending stiffness of the cable, as well as break out force transverse to the cable direction included in the soil model. Nevertheless, the cable ends seem to move slightly in the transverse direction at the end of the pull-over phase. This indicate that the cable model should have been longer to ensure no transverse movement at the end of the cable model. The effect on the pull-over force is most likely negligible as the axial force is much greater than the shear force. However, the found values for the maximum displacement may be slightly too large as the soil force transverse to the cable should have been larger.
The largest displacement occur for a perpendicular hit angle and decreases with decreasing hit angles. Similar to the curvature, the maximum displacement is shifted for hit angles 40° and 20° because of the sliding of the clump weight. The duration of trawling is the most important factor for the reduction of displacement of hit angle 80°, which is lower than for the perpendicular angle. For angles 40° and 20° the sliding of the clump weight causes the area where the clump weight is acting to shift. The displacement is therefore distributed over a larger area while reducing the maximum magnitude at a single point.

Table 5.5: Maximum global displacement for δ_{pen} = 63 mm and 10 kN pre-tension

Hit angle	**Time [s]**	**MGD [m**	**ΔMAF**
90°	63.7	4.22	
80°	62.9	2.09	-50.5 %
40°	64.0	1.35	-68.0 %
20°	69.5	1.21	-71.3 %

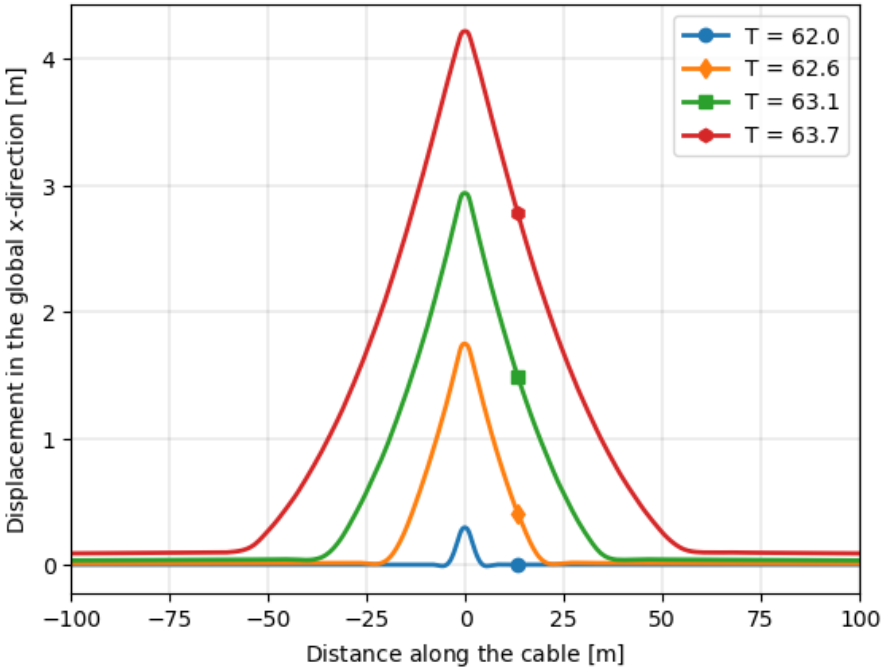

Figure 5.10: Displacement distribution history for a perpendicular hit angle, δ_{pen} = 63 mm, and 10 kN pre-tension

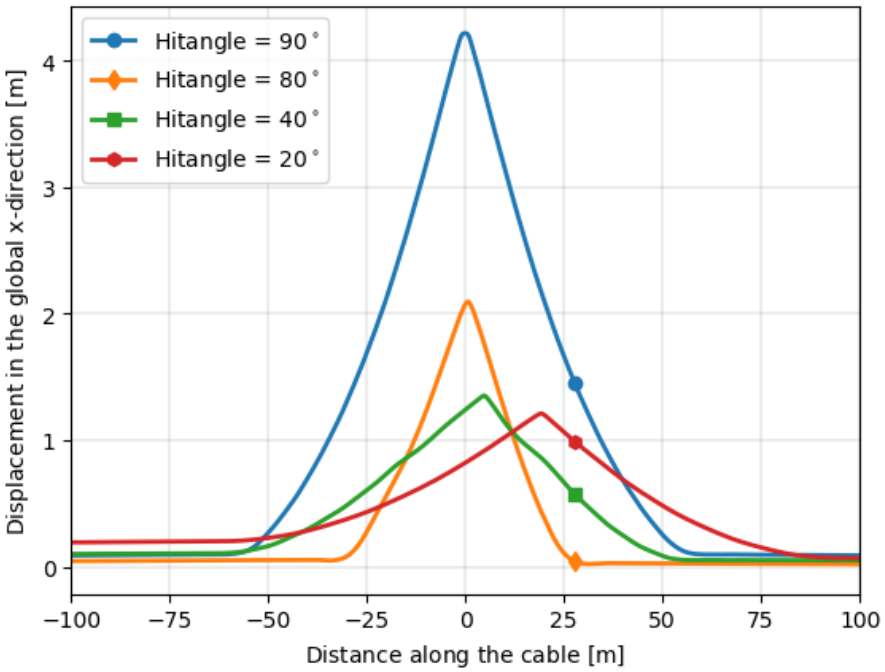

Figure 5.11: Displacement distribution for δ_{pen} = 63 mm and 10 kN pretension

5.3 Effect of relative penetration

The objective of this parameter study is to investigate the effect of the relative penetration, δ_{pen} between the power cable and the clump weight roller. The pretension for the presented plots are kept at 10 kN for all presented cases while the hit angle is varied to show the combined effect with the relative penetration.

5.3.1 Effect on pull-over force

Figure 5.12 and Figure 5.13 show the horizontal and vertical pull-over force respectively for a perpendicular hit angle and the three relative penetration cases. Similarly, Figure 5.14 and Figure 5.14 show the pull-over force for a 80° hit angle. Figure 5.16 and Figure 5.16 show the pull-over force for a 40° hit angle. Figure 5.18 and Figure 5.18 show the pull-over force for a 20° hit angle. The maximum horizontal force and maximum vertical force, time of occurrence and the percentage deviation for all hit angle and relative penetration cases are tabulated in Table 5.6.

As shown in Figure 5.12 it is apparent that both the duration and maximum magnitude of the horizontal pull-over force is increases with δ_{pen} for a perpendicular hit angle. The vertical pull-over force increases in a similar manner for hit angles 90°, 80°, and 40° with up to a 72 % increase for a perpendicular hit angle when the relative penetration is increased with 100 mm. The effect seem to be the opposite when the hit angle is reduced to 20° with a 7 % reduction between a δ_{pen} = 13 mm and δ_{pen} = 63 mm occur. When the relative penetration is increased up to 113 mm, the clump weight is no longer able to cross the cable and the vertical pull over force never reaches it maximum. The build up in horizontal pull-over follow the same pattern for all three relative penetration cases, thought for larger δ_{pen} the oscillations in the force are more prominent. The behaviour or the interaction also follows the same pattern as contact is only established between the clump wight barrel and the cable though the full duration of the pull-over phase. The reason for the increase in force and duration is mainly cased by the increase in the distance the clump wight has to be lifted above the cable.

Looking at Figure 5.14 and Figure 5.15 it is clear that the time history for the case with 80° hit angle is very jagged. The loosening of the convergence criterion for this case has made the solution

very unstable, causing large peaks is the pull-over force. This is especially prominent for δ_{pen} = 113 mm, where a local peak has a magnitude as high as 30 kN followed by a equally large trough. The irregularities are most likely caused by a contact loss followed by reattachment leading to large fluctuations in the contact force. The maximum value for this case occur at a large peak in the middle of the force build up, while for the rest of the cases the maximum pull-over force is at the very end of the pull-over phase. Consequently, the maximum values for this case is most likely too high and should be disregarded. The remaining results are very irregular as well and the only sure implication of the results is that the pull-over duration increase with the relative penetration.

For a 40° hit angle, the findings are very similar to those with the perpendicular hit angle. Figure 5.16 and Figure 5.17 show that the patterns are exactly the same except for the build up duration of the horizontal force. The impact of the relative displacement is large for the horizontal pull force, yielding a 56 % increase in the pull-over force for an increase of 100 mm in δpen. The effect on the vertical pull-over force is limited to only 10 % for the same increase in the relative displacement.
It can be seen that δ_{pen} a significant parameter for low hit angles. Figure 5.18 show that the three relative penetration cases follow the exact same build up in horizontal pull-over force. As for the previously discussed cases, the curve hit a critical point where the clump weight have managed to raise the contact point at the corner of the clump weight roller to the top of the power cable. This leads to a sudden drop in the contact force as the clump weight is sliding over the cable along the length of the roller barrel. However, for δ_{pen} = 113 mm, the slope of the pull-over curve decreases somewhat after T ≈ 71 s and the clump weight is unable to cross the power cable over the 100 s duration of the simulation. Rather than lifting itself up while sliding it is apparent from the visualization in Xpost that the clump weight is simply sliding along the cable with a stable bottom penetration. Figure 5.18 show that the pull-over is nevertheless growing slowly over time as it slides along the cable, and small oscillations in the pull-over force is observable after T ≈ 75 s. Because the clump weight slides out of the zone where the finest mesh is located, the accuracy of the solution is reduced significantly after T ≈ 71 s. This explains why there occur fluctuations in the pull-over force from this point of time and onward. As the pull-over force builds up over time it is possible that the clump weight is eventually able to build up sufficient force to cross the cable. On the other hand, based on the visual observations in Xpost there exist no signs that this may occur anytime soon after T = 86.0 s.

The combination of a 10° hit angle and δ_{pen} = 13 mm were also briefly studied to check if similar behaviour occur if the hit angle is reduced even further, but with a lower relative penetration. The results indicated that by reducing the hit angle even further, the clump weight is unable to cross even with very small relative penetrations.

Table 5.6: Maximum pull-over forces for 10 kN pre-tension

Hit angle	$\boldsymbol{\delta_{pen}}$	**Time [s]**	**MHF [kN]**	**ΔMVF**	**Time [s]**	**MVF [kN]**	**ΔMVF**
	13	62.8	37.7		63.0	37.2	
90°	63	63.5	49.3	+31.8 %	63.7	41.9	+12.6 %
	113	63.7	53.4	+41.6 %	63.9	40.4	+8.6 %
	13	62.3	32.1		62.3	27.3	
80°	63	62.7	31.2	−2.8 %	62.8	28.4	+4.0 %
	113	62.5	69.6	+116.8 %	62.5	40.4	+48.0 %
	13	62.2	12.8		62.9	28.0	
40°	63	63.9	15.3	+19.5 %	63.9	28.7	+2.5 %
	113	64.5	20.0	+56.3 %	64.5	30.7	+9.6 %
	13	66.7	15.5		67.8	26.0	
20°	63	69.1	18.6	+20.0 %	70.4	32.3	−6.9 %
	113	99.5	32.1	+107.1 %	99.5	11.7	−55.0 %

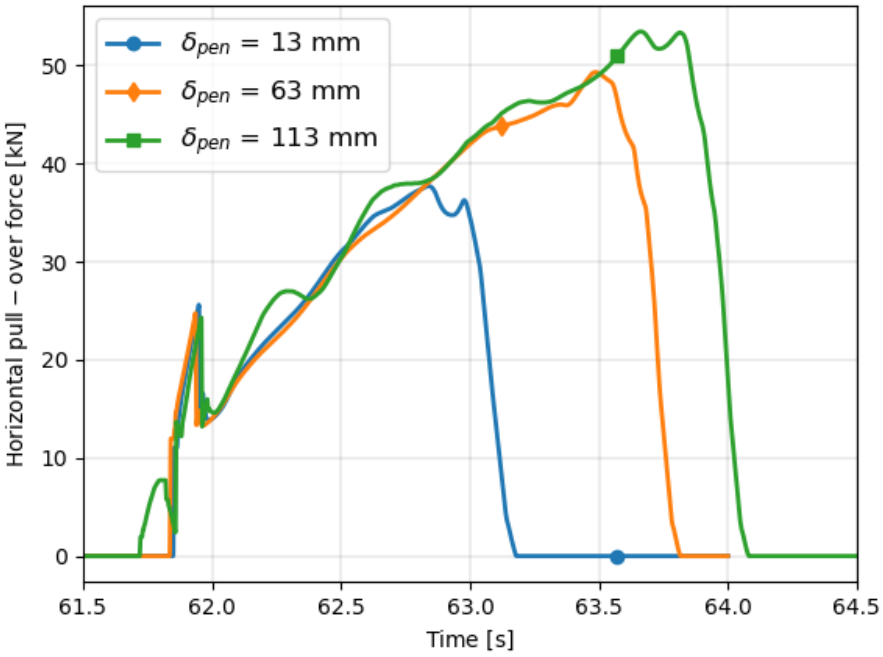

Figure 5.12: Horizontal pull-over force for 90° hit angle and 10 kN pretension

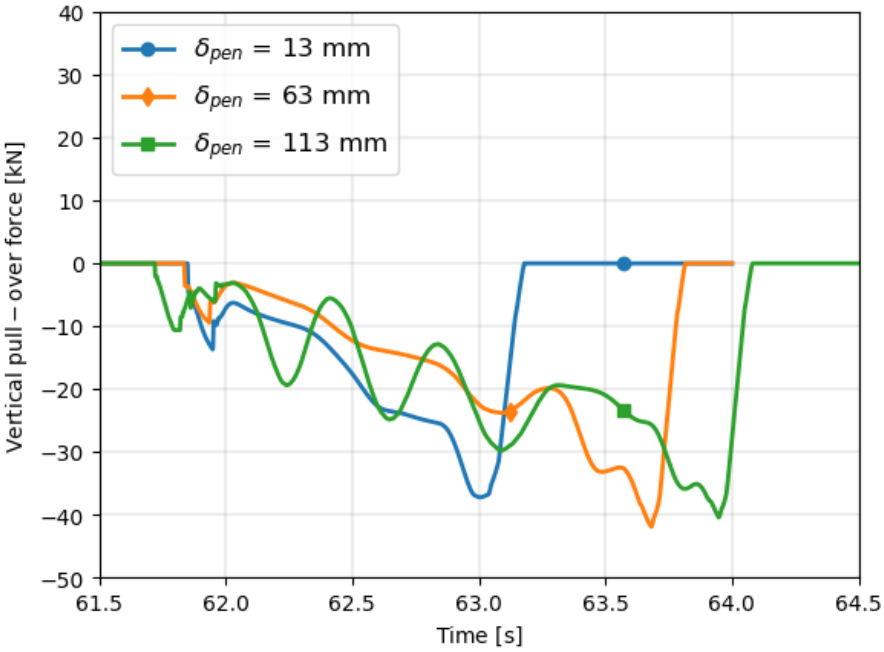

Figure 5.13: Vertical pull-over force for 90° hit angle and 10 kN pre-tension

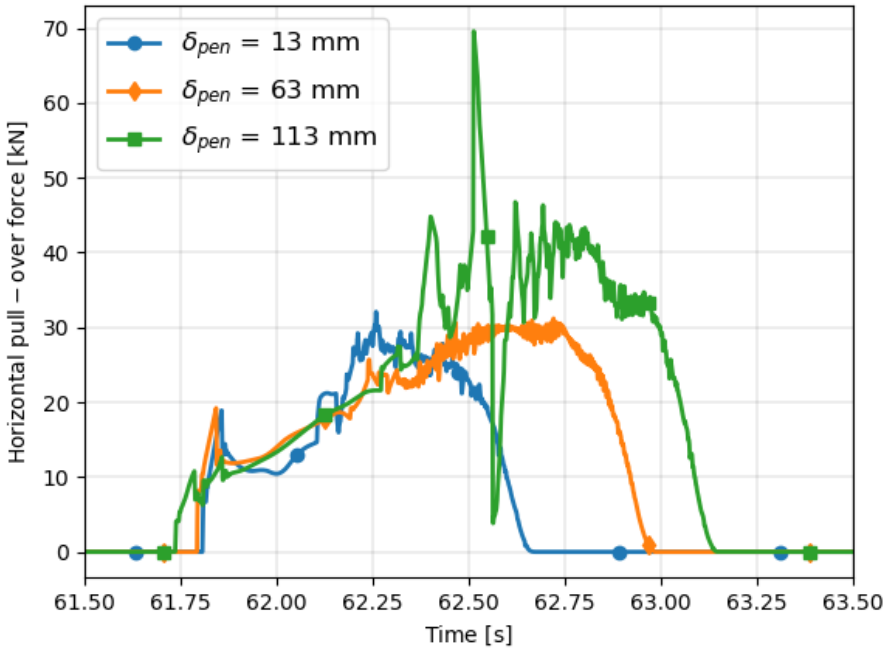

Figure 5.14: Horizontal pull-over force for 80° hit angle and 10 kN pretension

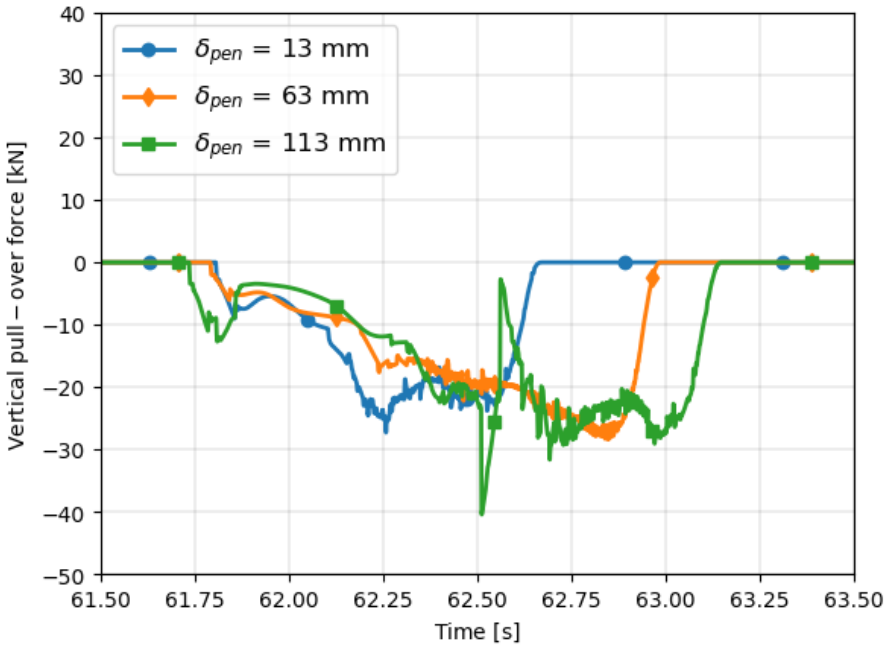

Figure 5.15: Vertical pull-over force for 80° hit angle and 10 kN pre-tension

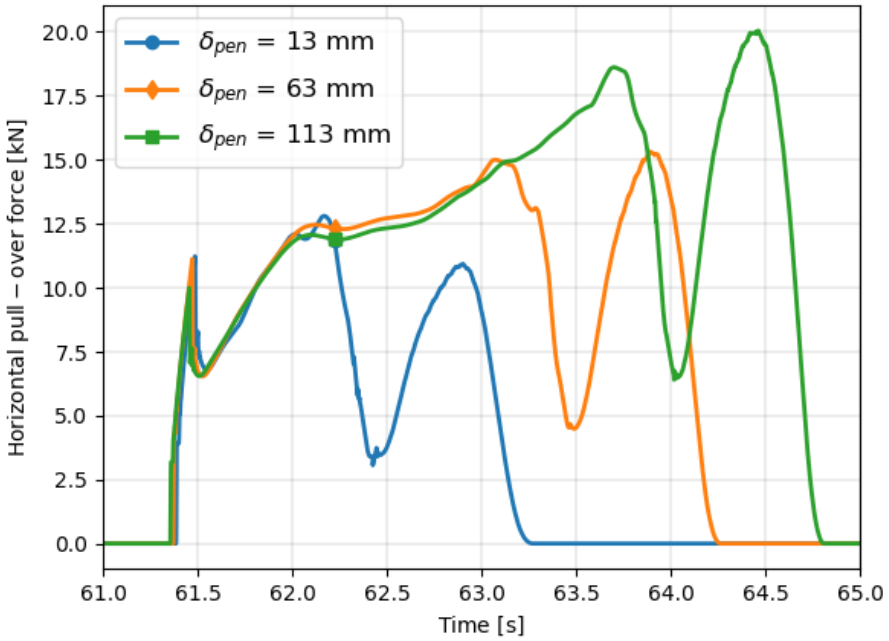

Figure 5.16: Horizontal pull-over force for 40° hit angle and 10 kN pre-tension

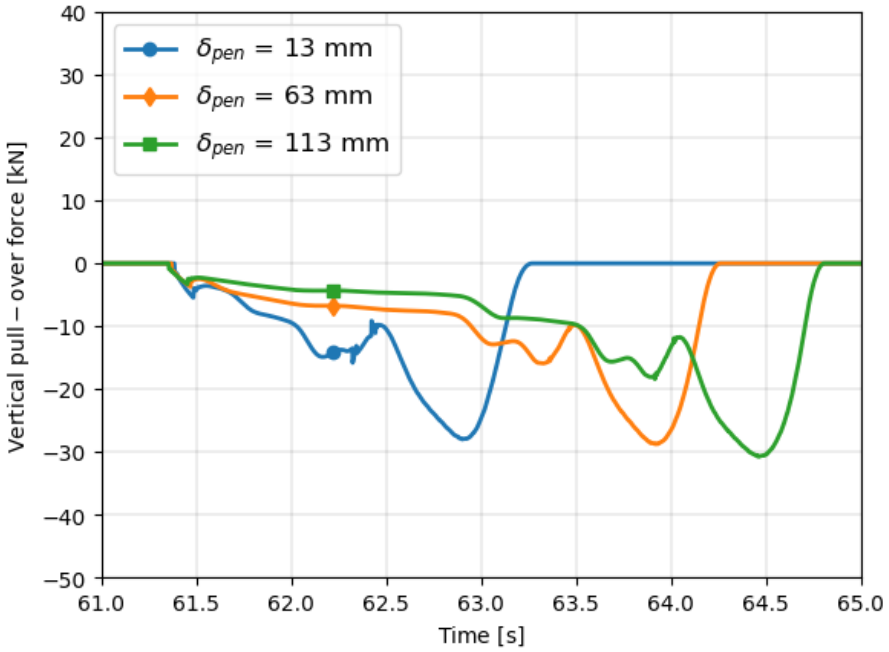

Figure 5.17: Vertical pull-over force for 40° hit angle and 10 kN pre-tension

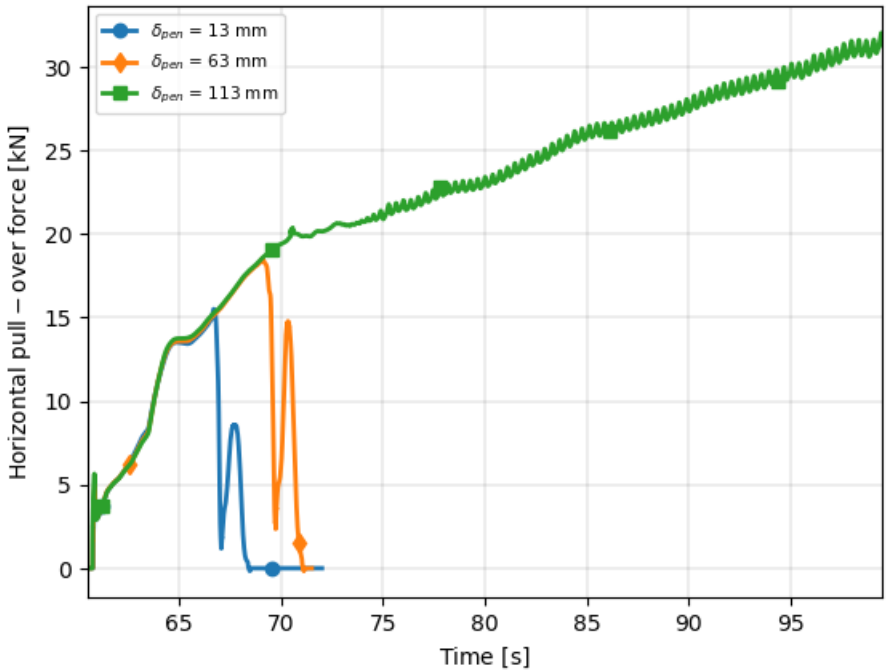

Figure 5.18: Horizontal pull-over force for 20° hit angle and 10 kN pre-tension

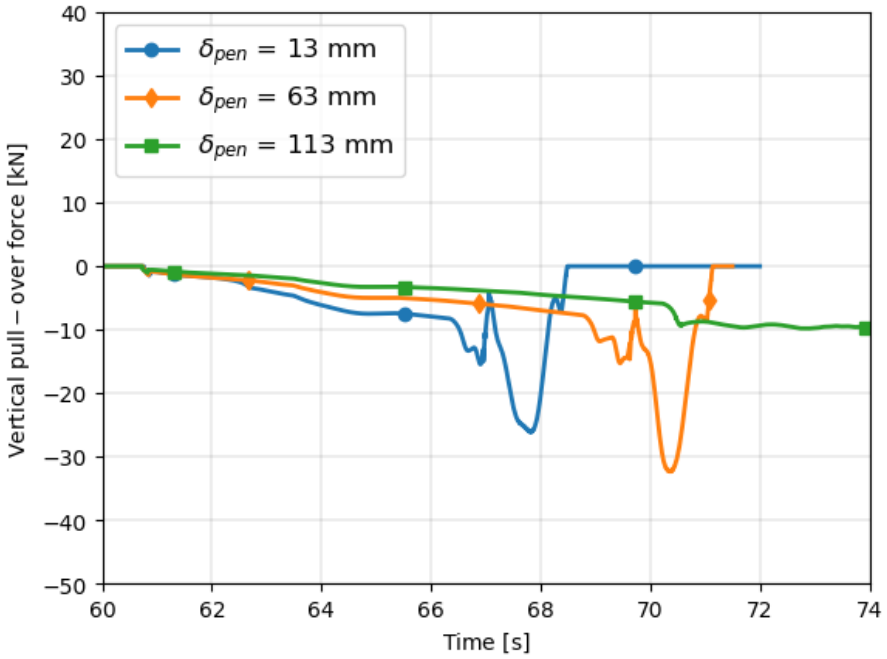

Figure 5.19: Vertical pull-over force for 20° hit angle and 10 kN pre-tension

5.3.2 Effect on axial force

Figure 5.21 show the axial force distribution for a perpendicular hit angle and the three relative penetration cases. Similarly, Figure 5.22, Figure 5.23, and Figure 5.24 show the axial force distribution for hit angles 80°, 40°, and 20° respectively. The maximum axial force, time of occurrence and corresponding percentage deviation for all hit angle and relative penetration cases are tabu-

lated in Table 5.7.

Just as for the pull-over force, the maximum axial force increase with the relative penetration for all hit angles. Because of the low bending stiffness of the cable, most of the contact force from the clump weight acting on the cable is transferred to axial force. Therefore, the same arguments apply as for the pull-over force. However, in comparison to the maximum pull-over force found for a 80° hit angle, the axial force does not have a unnatural high maximum high value. As contact and structural damping will mitigate some of the fluctuation in contact force, this difference is not unexpected.

The relative penetration also seem to have a greater impact for smaller hit angles, as the percentage increase in the axial force listed in Table 5.7 is larger for 80° and 40° than for a 90° hit angle. This is probably because of the unequal distribution of force transferred from the interaction with the clump weight. On the other hand, the maximum axial forces found for 10° has a lower increase between δ_{pen} = 13 mm and δ_{pen} = 63 mm compared to the other hit angles, and the increase between δ_{pen} = 63 mm and δ_{pen} = 133 mm is much higher. This is most probable due to the fact that the clump weight is unable to cross the pipeline for the latter case.

Figure 5.20 show the build up of axial force over time for the case of where the clump weight is unable to cross the cable. The axial force increase gradually all the way up to T = 86 s just as shown as for the horizontal pull-over force shown in Figure 5.18. The peak of the axial force is moved to the positive direction along the cable due to the sliding motion. The jump in the axial force at the contact point between the clump weight also grows over time in correlation with the increase in maximum axial force.

Table 5.7: Maximum axial force for 10 kN pre-tension

Hit angle	$\boldsymbol{\delta_{pen}}$	**Time [s]**	**MAF [kN]**	**ΔMAF**
	13	62.9	116.9	
90°	63	63.6	146.8	+25.6 %
	113	63.7	158.7	+35.8 %
	13	62.5	80.2	
80°	63	62.7	102.3	+27.6 %
	113	62.9	112.8	+40.6 %
	13	62.2	60.6	
40°	63	63.9	80.5	+32.8 %
	113	63.8	93.3	+54.0 %
	13	66.8	86.5	
20°	63	69.0	104.8	+21.2 %
	113	85.9	154.5	+78.6 %

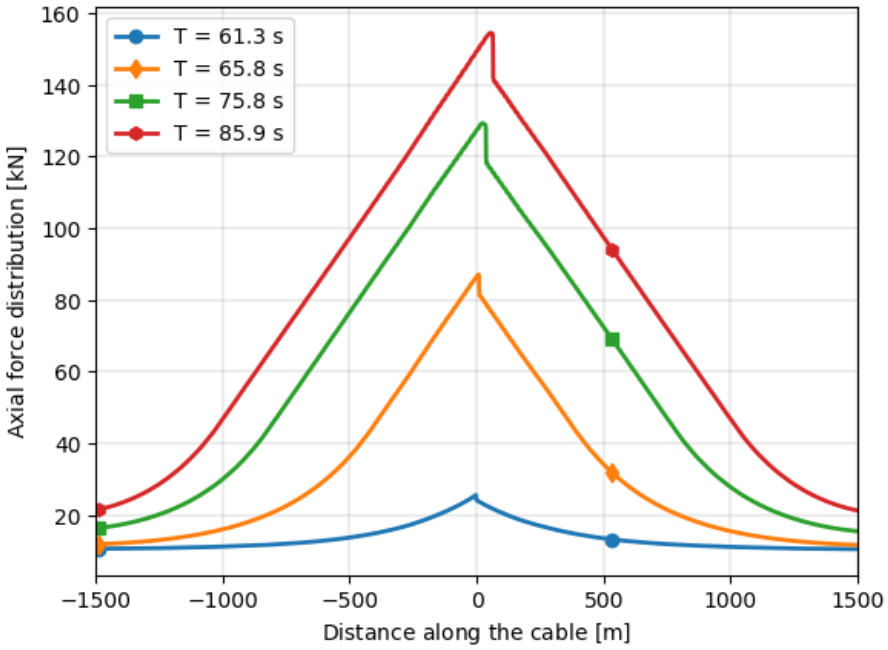

Figure 5.20: Axial force distribution history for a 20° hit angle, $\delta_{pen} = 113mm$, and 10 kN pre-tension

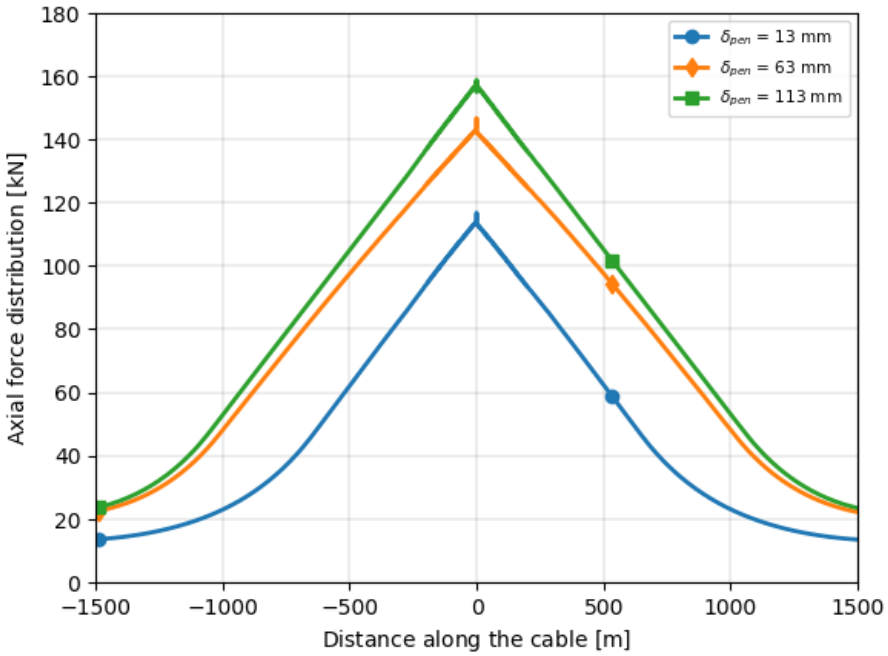

Figure 5.21: Axial force distribution 90° hit angle and 10 kN pre-tension

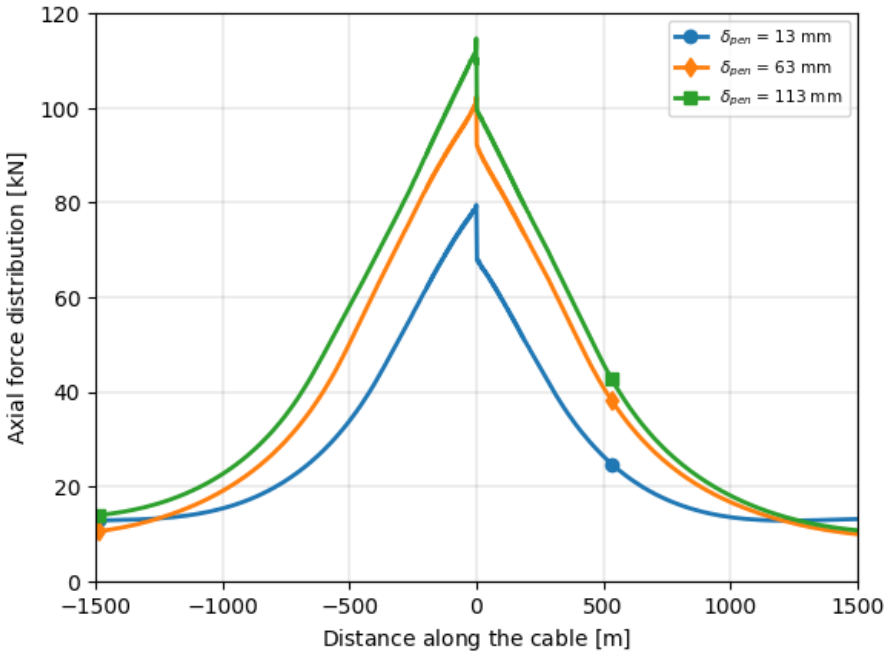

Figure 5.22: Axial force distribution 80° hit angle and 10 kN pre-tension

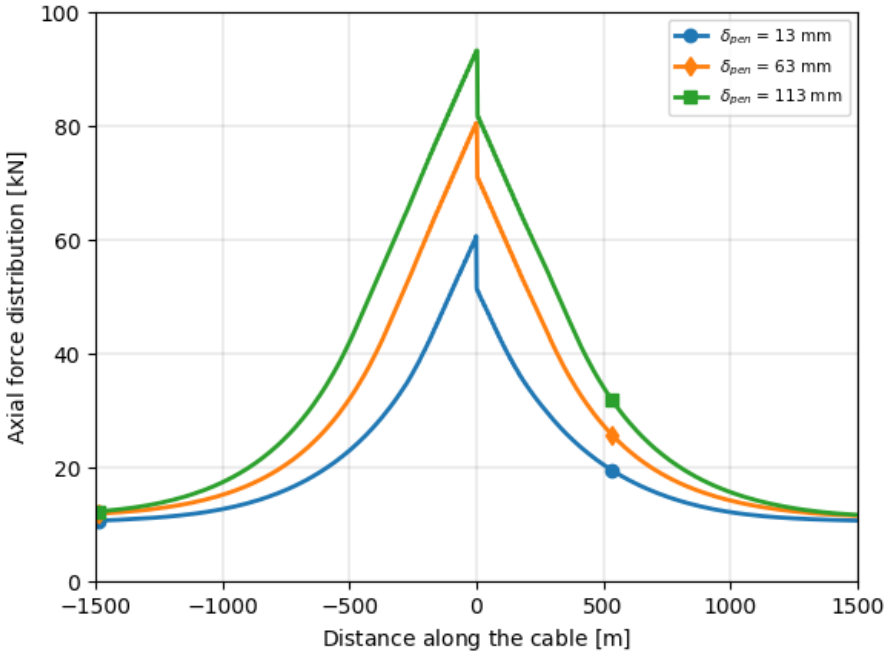

Figure 5.23: Axial force distribution 40° hit angle and 10 kN pre-tension

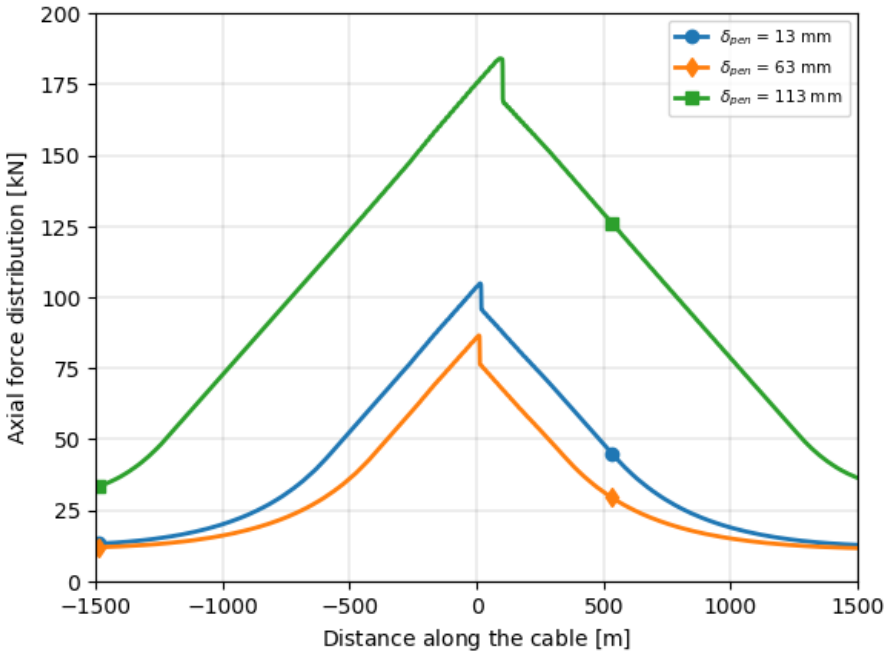

Figure 5.24: Axial force distribution 20° hit angle and 10 kN pre-tension

5.3.3 Effect on displacement

Figure 5.26 show the displacement distribution in the global y-direction for a perpendicular hit angle and the three relative penetration cases. Similarly, Figure 5.22, Figure 5.28, and Figure 5.29 show the displacement distribution for hit angles 80°, 40°, and 20° respectively. The maximum global displacement, time of occurrence and corresponding percentage deviation for all hit angle and relative penetration cases are tabulated in Table 5.8.

The relative displacement has a large impact on the maximum global displacement with up to a 151.4 % increase in the maximum displacement for for a 100 mm increase in relative penetration for a 40°. The relative penetration has in subsection 5.3.1 shown to increase the pull-over duration. Since the clump wight is kept in motion during the entire duration of the pull-over phase, the displacement will naturally be larger. The increase in maximum displacement seem to be the greatest for moderate hit angles, where the combination of a long pull-over duration is combined to a limited amount of sliding. For example, the clump weight slides over a considerable distance along the cable for the 20° hit angle, displacing a long section of the cable. The maximum displacement will as a result be less localized and therefore smaller in maximum magnitude.

The displacement distribution over time for the combined case of hit angle and penetration which render the clump weight unable to cross the cable is shown in Figure 5.25. The movement of the contact point over time due to the sliding motion is here clearly visible. Due to the increase in the maximum displacement over time it is apparent that the sliding motion must be at a slightly higher angle than the hit angle.

Table 5.8: Maximum displacement for 10 kN pre-tension

Hit angle	δ_{pen}	**Time [s]**	**MGD [kN]**	**ΔMGD**
90°	13	63.1	2.67	
	63	63.7	4.22	+58.1 %
	113	64.0	4.89	+83.1 %
80°	13	62.6	1.39	
	63	62.9	2.09	+50.4 %
	113	63.0	2.41	+73.4 %
40°	13	63.0	0.70	
	63	64.0	1.35	+92.9 %
	113	64.6	1.76	+151.4 %
20°	13	66.9	0.89	
	63	69.5	1.21	+35.9 %
	113	86.0	2.23	+150.6 %

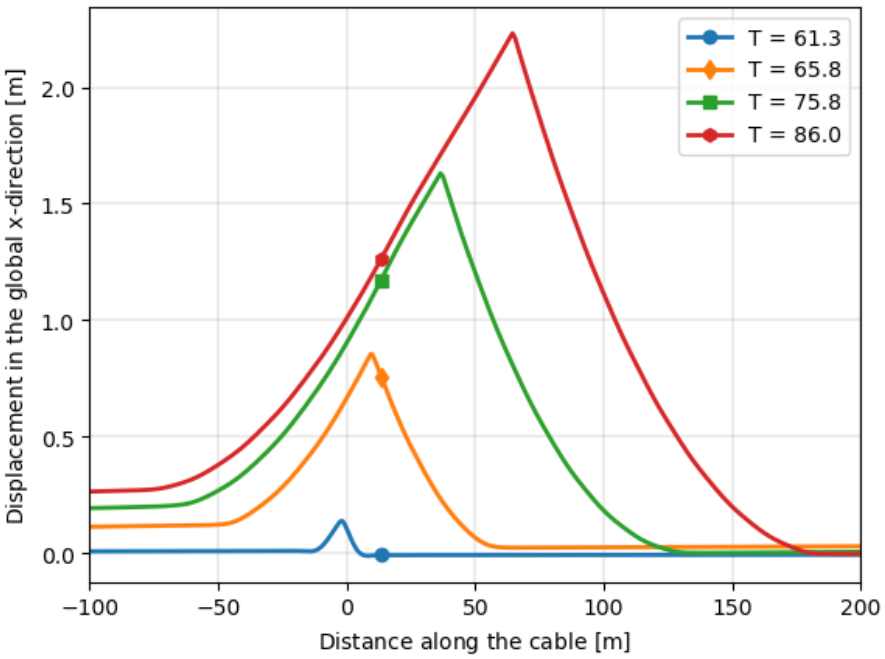

Figure 5.25: Displacement distribution over time for a 20° hit angle, δ_{pen} = 113 mm, and 10 kN pre-tension

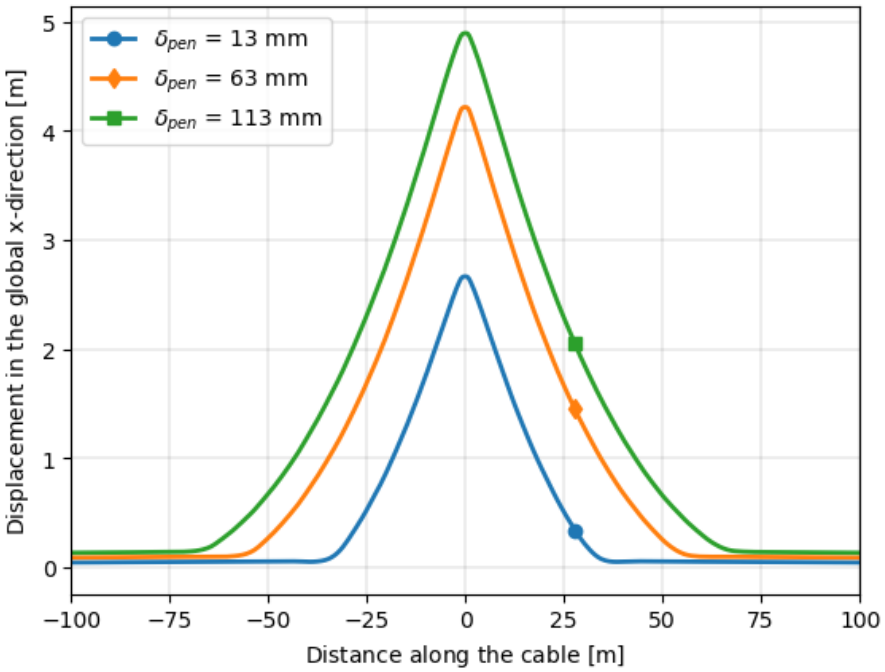

Figure 5.26: Displacement distribution for a 90° hit angle and 10 kN pre-tension

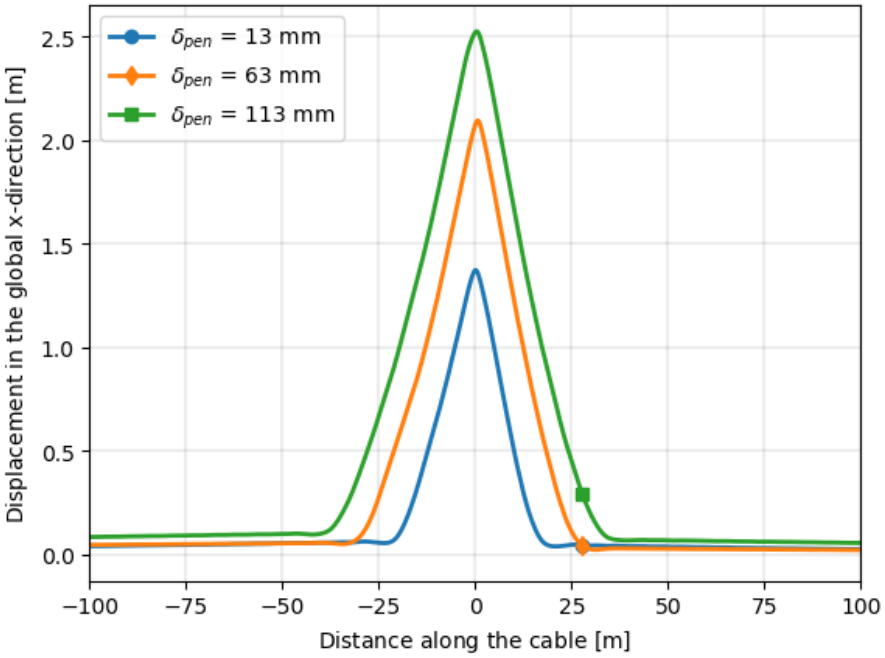

Figure 5.27: Displacement distribution for a 80° hit angle and 10 kN pre-tension

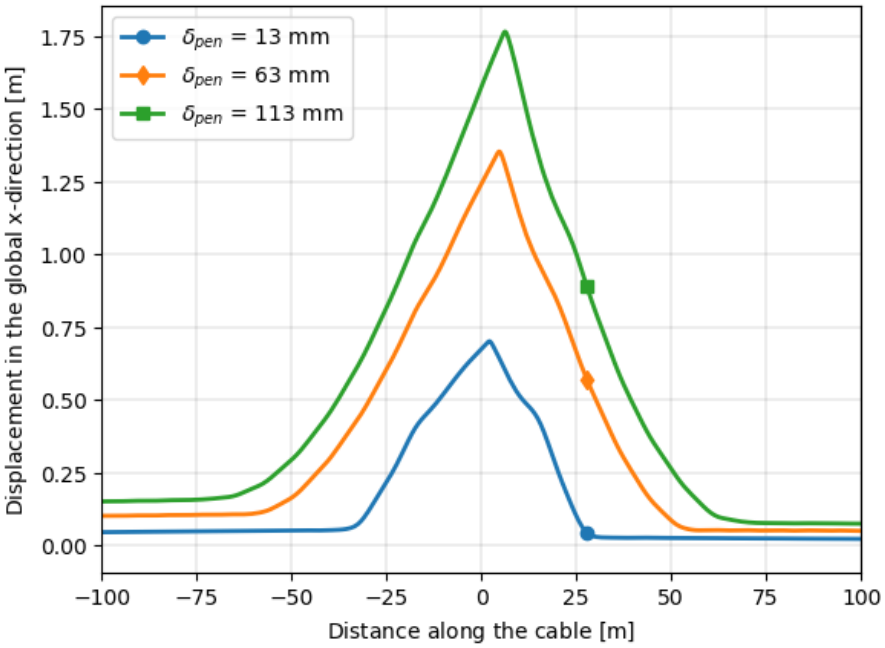

Figure 5.28: Displacement distribution for a 40° hit angle and 10 kN pre-tension

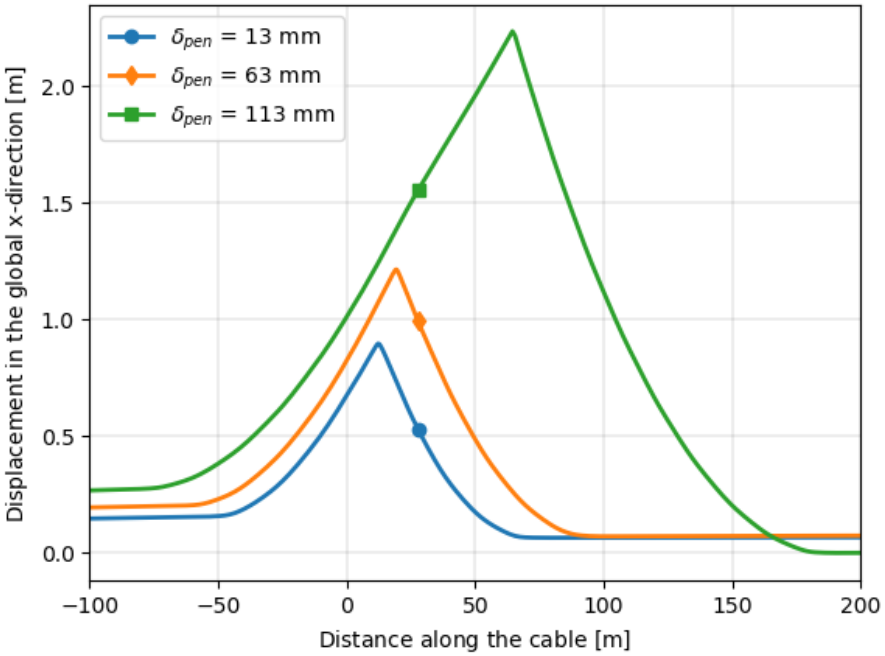

Figure 5.29: Displacement distribution for a 20° hit angle and 10 kN pre-tension

5.3.4 Effect on curvature

Figures 5.31 show the curvature distribution for a perpendicular hit angle and the three relative penetration cases. Similarly, Figure 5.32, Figure 5.33, and Figure 5.34 show the curvature distribution for hit angles 80°, 40°, and 20° respectively. The Maximum curvature, time of occurrence and corresponding percentage deviation for all hit angles and relative penetration cases are tabulated in Table 5.9.

The results show that the curvature increases with increasing relative penetration. The difference in curvature is small between δ = 13 mm and δ = 63 mm, while there is a significant difference when the relative penetration is increased to 113 mm. The difference is very prominent for the combination of a 20° hit angle and between a 13 mm and a 113 mm penetration, with a increase of 54 % in the curvature can be observed. In the latter case the clump weight is unable to cross the cable, and the curvature seem to build up as the clump weight is sliding along the cable. Even though the curvature is still far below the design limit, it is possible that the curvature may exceed it if the sliding motion continues.
Figure 5.30 show the distribution of curvature along the cable over time for the combined case of hit angle and relative penetration resulting in the clump weight is not able to cross the cable. One can see that the curvature start to flatten out up until T = 71.8 after which it suddenly drops. The drop is followed by a rapid increase with large fluctuation in the curvature levels, stabilizing again after T = 85.5 s. At time the drop occur the clump weight has slided far enough to reach the point along the distance of the cable where the mesh size starts its transitions from 0.172 m to 1 m. The solution found after T = 71.8 s is therefore much less accurate and the behaviour after this point is uncertain. Nevertheless, the pull-over force shown in Figure 5.18, which is much less sensitive to the mesh size, is increasing over time. One can therefore expect the curvature to increase as well. Even though the maximum curvature up to T = 100 s is still only 0.85 % of the design limit, further research with a smaller mesh size is needed to ensure that the limit is not exceeded.

Table 5.9: Maximum curvature for 10 kN pre-tension

Hit angle	$\boldsymbol{\delta_{pen}}$	**Time [s]**	**MC [kN]**	**ΔMC**
	13	63.0	0.275	
90°	63	63.5	0.311	+13.1 %
	113	63.8	0.322	+17.1 %
	13	62.1	0.287	
80°	63	62.1	0.299	+4.2 %
	113	62.2	0.349	+21.65 %
	13	62.2	0.207	
40°	63	63.9	0.235	+13.5 %
	113	64.5	0.274	+32.4 %
	13	66.7	0.211	
20°	63	70.5	0.230	+9.0 %
	113	99.1	0.358	+69.7 %

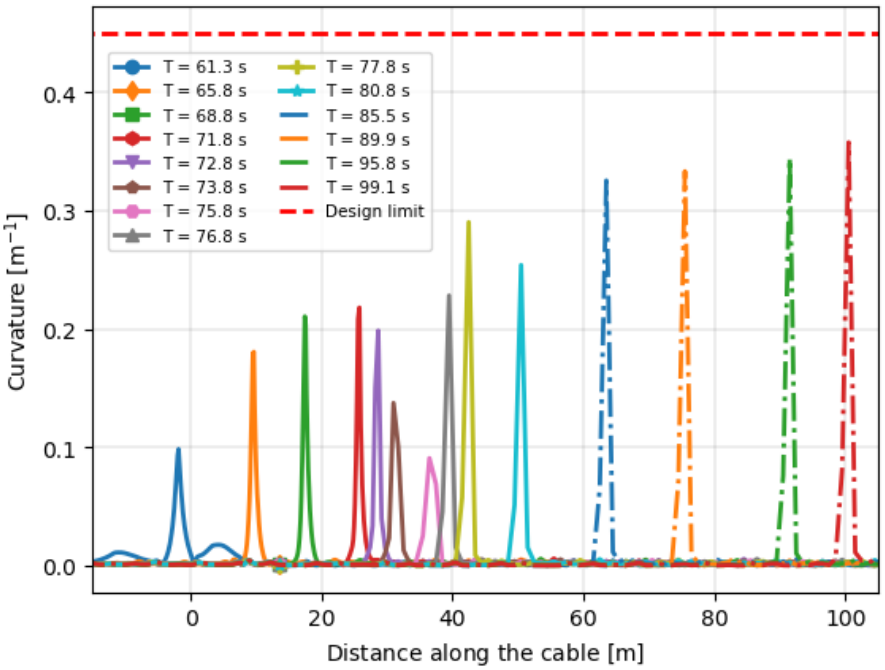

Figure 5.30: Curvature distribution over time for a 20° hit angle, δ_{pen} = 113 mm, and 10 kN pre-tension

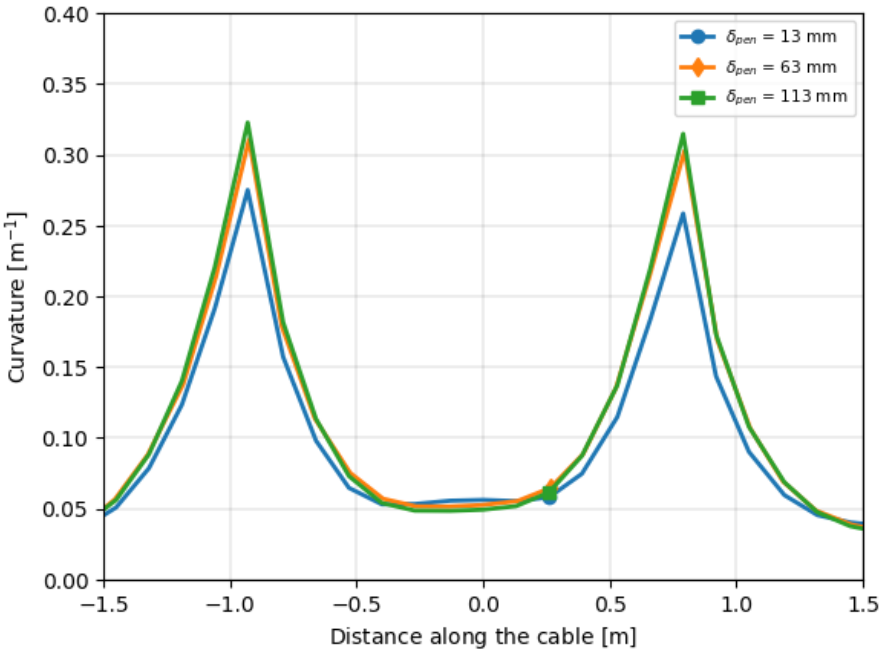

Figure 5.31: Curvature distribution for a 90° hit angle and 10 kN pre-tension

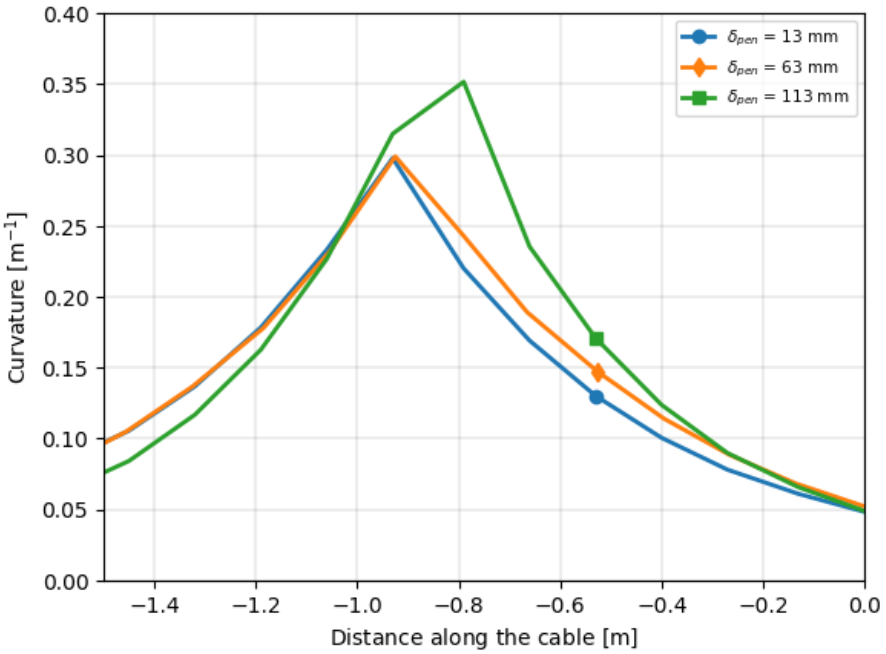

Figure 5.32: Curvature distribution for a 80° hit angle and 10 kN pre-tension

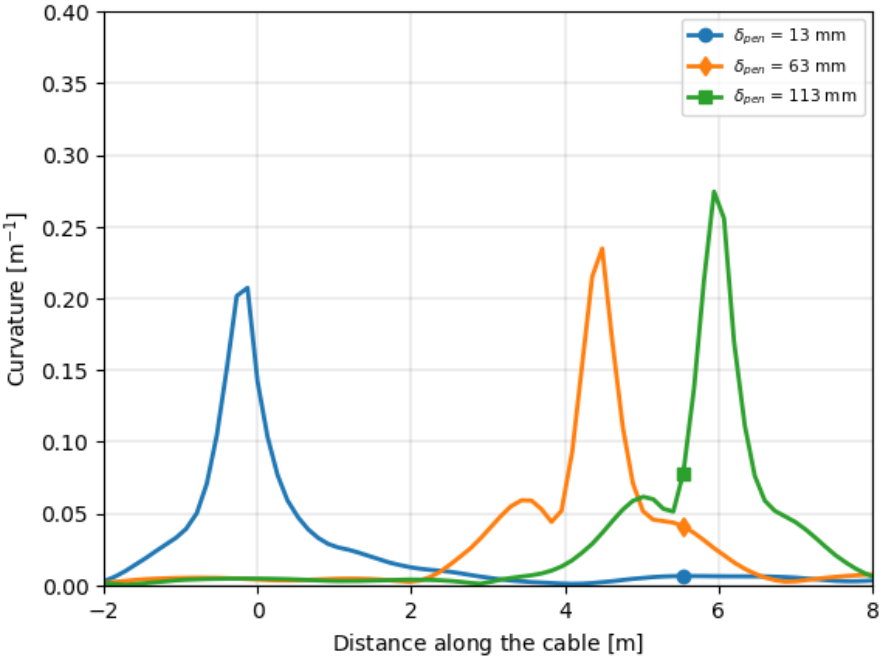

Figure 5.33: Curvature distribution for a 40° hit angle and 10 kN pre-tension

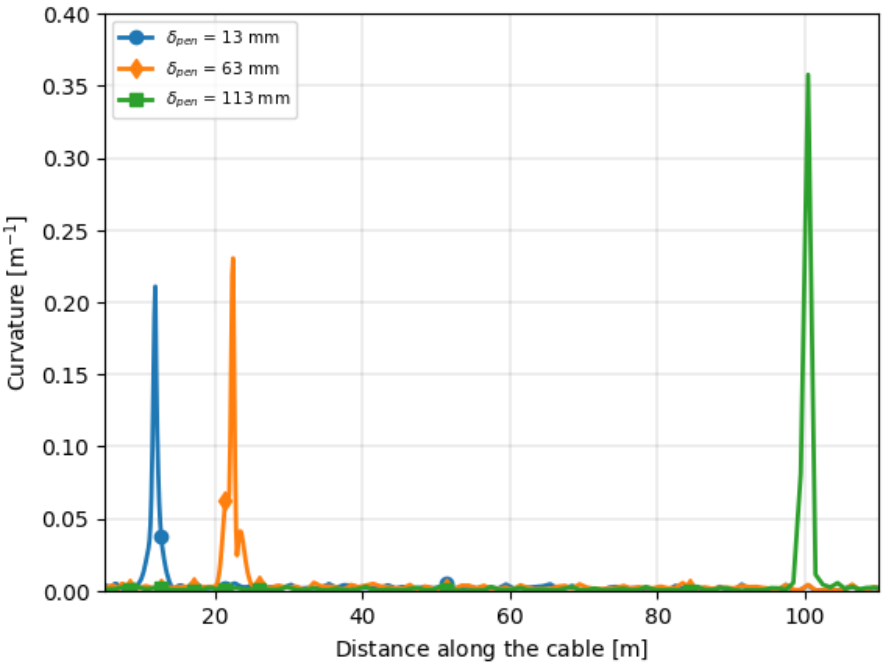

Figure 5.34: Curvature distribution for a 20° hit angle and 10 kN pre-tension

5.4 Effect of pretension

The goal of this sensitivity study is to investigate the effect of the pre-tenstion in the cable on the pull-over force, axial force, curvature and displacement.

5.4.1 Effect on pull-over force

Figure 5.35 and Figure 5.36 show the time history of the largest horizontal and vertical pull-over force respectively. Maximum horizontal force, time of occurrence and the percentage difference between the 10 kN case and the 1 kN case is tabulated in Table 5.10.

It is apparent that the pre-tension has a minor effect on the maximum pull-over force. By decreasing the pre-tension level from 10 kN to 1 kN, one can observe decrease approximately 1 % in the maximum pull-over force. For the vertical pull-over force a decrease of up to 2 % can be observed. The exception is the 80° case, where the maximum pull-over force is found to be 1.4 % higher for the 1 kN case. The validity of this finding is questionable, as the maximum horizontal force is increasing for the same increase in pre-tension. The convergence tolerance were raised significantly for this hit angle, resulting in a reduction in result accuracy, which may very well be higher than the 1.4 % deviation between the maximum pull-over force of the two pre-tension levels.

The increase in pretension will increase the stiffness of the cable initially, but will be more and more insignificant as the axial force builds up. The necessary pull force will hence be similar for the two pre-tension cases, as the resistance offered by the cable is not significantly increased.

Table 5.10: Maximum horizontal force difference between 10 kN and 1 kN pre-tension

Hit angle	Pre-tension	Time [s]	MHF [kN]	ΔMVF	Time [s]	MVF [kN]	ΔMVF
90°	10 kN	63.5	49.3	-0.8 %	63.7	41.9	-0.7 %
	1 kN	63.5	48.9		63.7	41.6	
80°	10 kN	62.7	31.2	-1.0 %	62.8	28.4	1.4 %
	1 kN	62.9	30.9		62.9	28.8	
40°	10 kN	63.9	15.3	0.0 %	63.9	28.7	-0.7 %
	1 kN	63.9	15.3		63.9	28.5	
20°	10 kN	69.1	18.6	-1.1 %	70.4	32.3	-1.8 %
	1 kN	69.2	18.4		70.5	31.7	

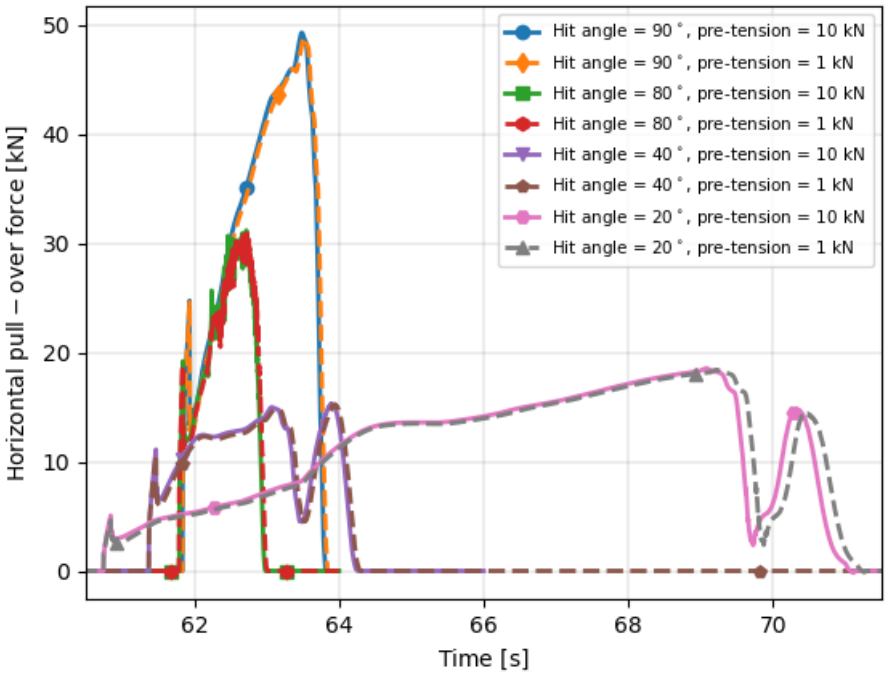

Figure 5.35: Horizontal pull-over force for $\delta_{pen} = 63$ mm

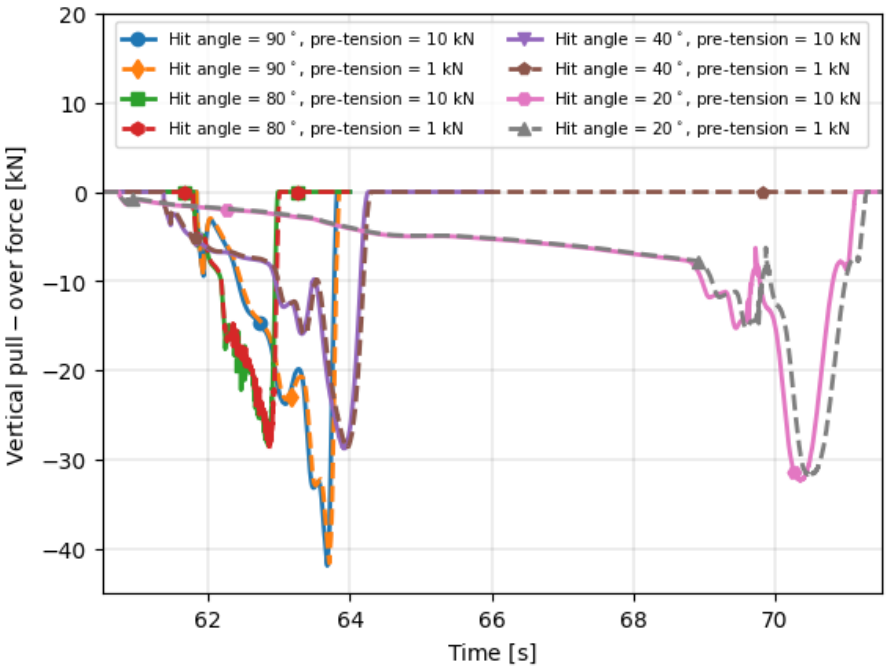

Figure 5.36: Vertical pull-over force for $\delta_{pen} = 63$ mm

5.4.2 Effect on axial force

Figure 5.37 show the the axial force distribution at mid span at the time where maximum axial force occur, and Table 5.37 show he maximum values, time of occurrence and the percentage difference between the 10 kN case and the 1 kN case.

Just as for the pull-over force, the maximum axial force is only slightly affected by the pre-tension. The difference in the maximum occurrence is somewhat less than the difference in the pre-tension, ranging from a 33% reduction for the 90° hit-angle up to a 56% reduction for the 20° hit angle. As the cable is displaced, the pre-tension will only yield a component of it's force in the trawling direction and the resistance offered will therefore also not be proportional to the pre-tension. It is hence not unexpected that the difference in maximal force is lower than for that of the pre-tension.

Table 5.11: Maximum axial force difference between 10 kN and 1 kN pre-tension.

Hit angle	**Pre-tension**	**Time [s]**	**MAF [kN]**	**ΔMAF**
90°	10 kN	63.6	146.8	-4.1 %
	1 kN	63.6	140.8	
80°	10 kN	62.7	102.3	-3.9 %
	1 kN	62.7	97.6	
40°	10 kN	63.2	80.5	-7.4 %
	1 kN	63.2	75.1	
20°	10 kN	69.0	104.8	-3.8 %
	1 kN	69.4	100.8	

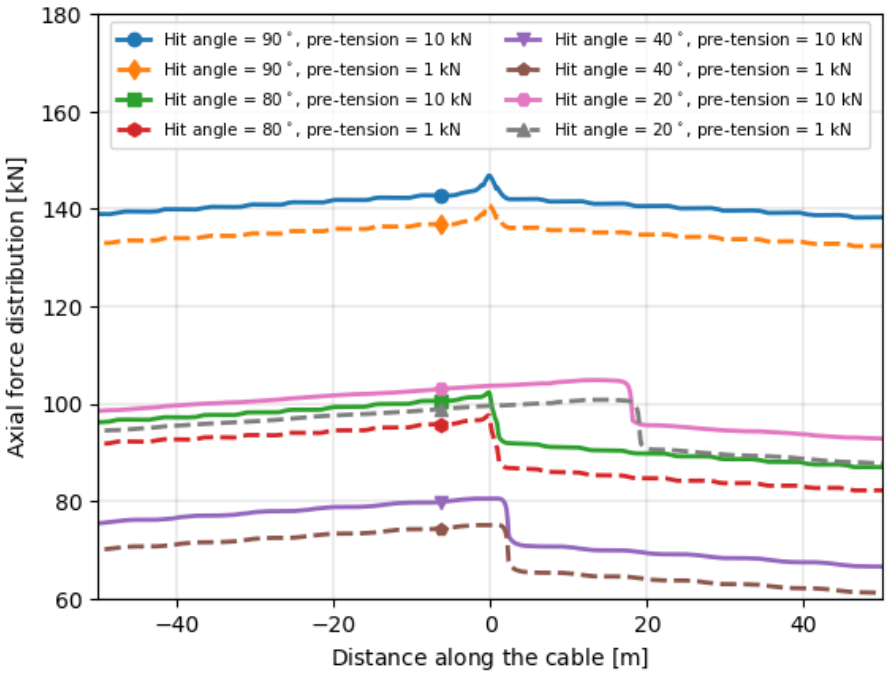

Figure 5.37: Axial force distribution for $\delta_{pen} = 63$ mm

5.4.3 Effect on curvature

Figure 5.38 and Figure 5.39 show the distribution of the curvature at the time where the maximum curvature occur for the two pre-tension cases. Table 5.12 show the magnitudes of the maximum curvatures, time of occurrence and corresponding percentage deviation between the 10 kN and the 1 kN pre-tension case. The results show that the maximum curvature is reduced by increasing the pre-tension in the cable and the effect seem to be greater for lower hit angles. The increase in tension in the cable will effectively increase the bending stiffness of the cable and naturally the curvature will be lower for larger values of pre-tension.

Table 5.12: Curvature difference between 10 kN and 1 kN pre-tension

Hit angle	**Pre-tension**	**Time [s]**	**MC [m^{-1}]**	**ΔMC**
90°	10 kN	63.5	0.311	1.0 %
	1 kN	63.6	0.314	
80°	10 kN	62.1	0.299	1.3%
	1 kN	62.2	0.303	
40°	10 kN	63.9	0.235	4.3 %
	1 kN	64.0	0.245	
20°	10 kN	70.5	0.230	8.7 %
	1 kN	70.5	0.250	

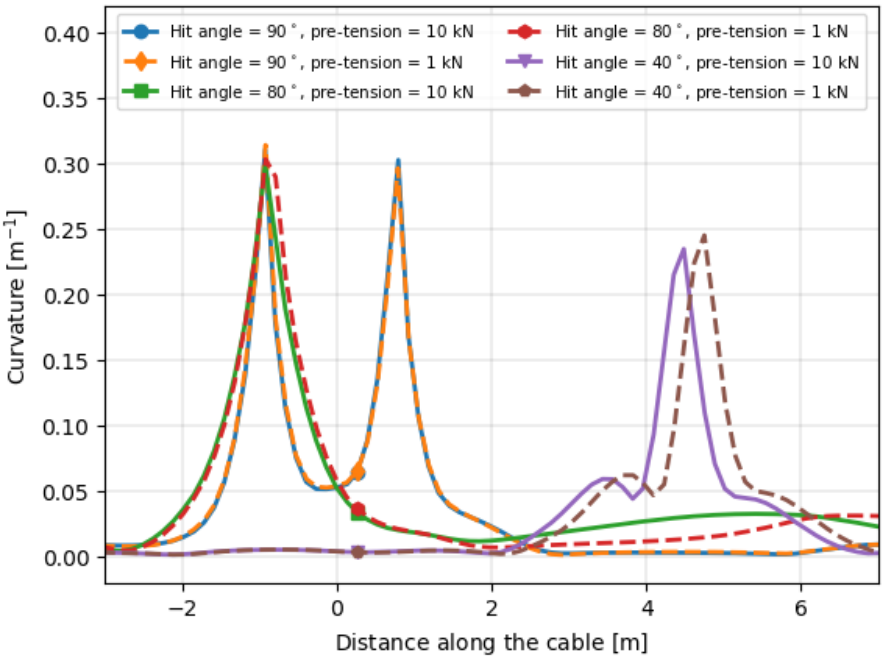

Figure 5.38: Curvature distribution for hit angles 90°, 80° and 40° with $\delta_{pen} = 63$ mm

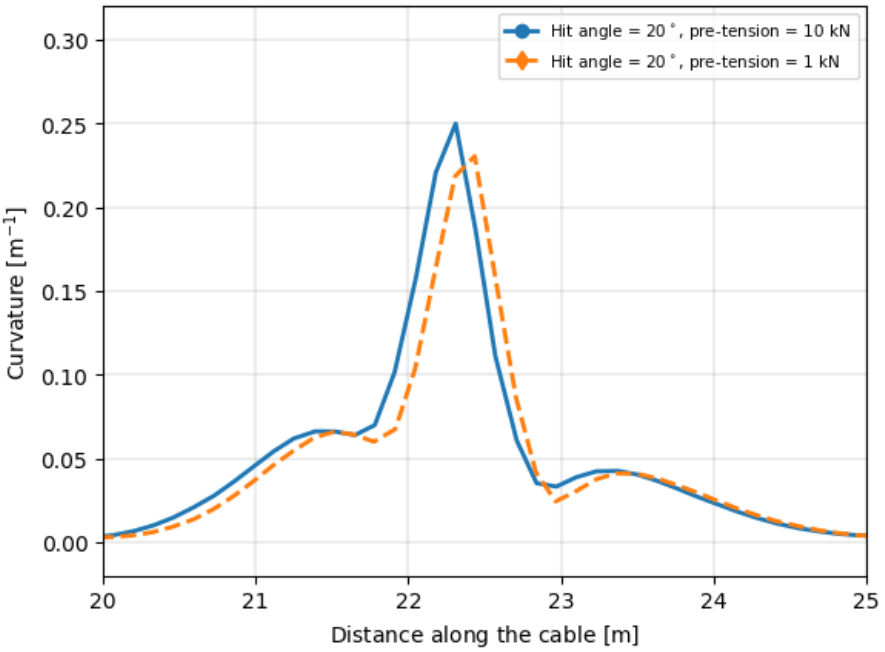

Figure 5.39: Curvature distribution for a 20° hit angle and $\delta_{pen} = 63$ mm

5.4.4 Effect on displacement

Figure 5.40 show the cable displacement distribution in the global y-direction at mid span. Table 5.13 show the values for maximum global displacement, time of occurrence and corresponding percentage deviation between the 10 kN and the 1 kN pre-tension case.

The results show that the displacement increases by decreasing the pre-tension in the cable with

a small amount. As the pre-tension increase the effective bending stiffness, the displacement is distributed over a wider distance over the cable and therefore be less localized at the contact point between the cable and the clump weight.

Table 5.13: Maximum displacement difference between 10 kN and 1 kN pre-tension

Hit angle	**Pre-tension**	**Time** [s]	**MGD** [m]	**ΔMGD**
90°	10 kN	63.7	4.22	1.7 %
	1 kN	63.8	4.29	
80°	10 kN	62.9	2.09	1.9 %
	1 kN	62.9	2.13	
40°	10 kN	64.0	1.35	3.7 %
	1 kN	64.1	1.40	
20°	10 kN	69.5	1.21	3.3 %
	1 kN	69.5	1.25	

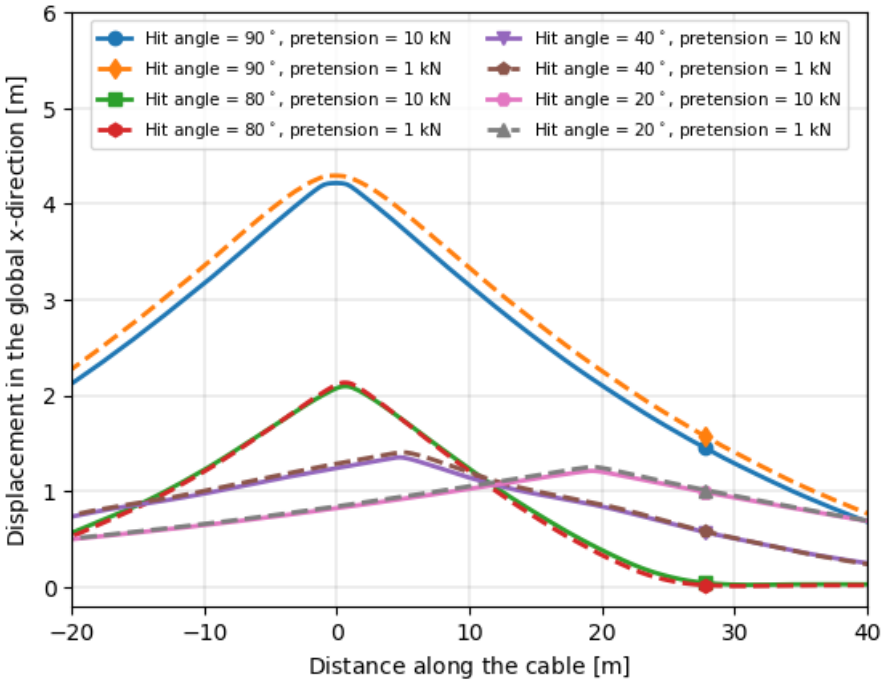

Figure 5.40: Displacement distribution for $\delta_{pen} = 63$ mm

6 Conclusion

6.1 DNVGL-RP-F111 applied on cable trawling

The results presented in chapter 5.1 show that the horizontal pull over force predicted by DNVGL-RP-F111 is much greater than the pull-over force obtained using the SIMLA model. The difference were largest for a 13 mm relative penetration where the predicted horizontal force by the RP were found to be more than four times higher than the one found through simulations. The duration of the pull-over phase were also found to be only half the duration estimated for the RP for δ_{pen} and about two third of the estimated duration for $\delta_{pen} = 113$ mm. One can therefore conclude that DNVGL-RP-F111 can not be used to predict pull-over forces resulting from interaction between clump weights and offshore power cables.

6.2 Effect of hit angle

It has been shown in chapter 5.2 that the maximum pull-over force, maximum axial force, maximum cable curvature and maximum global displacement are largest for a perpendicular hit angle. The pull-over force were significantly larger than the other hit angles, provided the clump weight were able to cross the cable, with a maximum up to 69 % larger than that of a 40° hit angle. The force were found to be lowest for moderate hit angles, and increase again for low hit angles due to the sliding motion of the clump weight. The same were found for in the axial force, where the maximum occurrence were 45 % higher for a perpendicular case than for a 40° hit angle. The maximum global displacement were found to decrease with the hit angle, with up to a 71.3 % reduction between a perpendicular and a 20° hit angle. Changing from a perpendicular hit angle to a 20° hit angle reduced the curvature with 26 %, when the relative penetration were 63 mm. The duration of the pull-over phase were decreased significantly when the hit angle were changed from a perpendicular one to one with a slightly lower angle. Due to sliding, the pull-over duration increased again when the hit angle is reduced down to 40° or lower.

The combination of hit angles of 20° and below in combination with relative penetration of 113 mm has shown to be critical for interaction as the clump weight is unable to cross the power cable in the first 40 seconds after contact. The result is a continuous sliding motion with gradually increasing horizontal pull-over force, axial force and curvature. Due to the longevity of the simulation however, the accuracy of the solution is significantly reduced. Firstly, the clump weight slides far enough over the duration of the simulation to leave the section of the cable where the mesh is sufficiently refined. In addition, the large displacements of the trawl board nodes transverse to the direction of trawling in the simulation may cause the interaction forces to be nonphysical. Even though the maximum pull-over force, maximum axial force and maximum curvature seem to be higher for this configuration than the other cases of the scope, the accuracy of the simulation results need to be improved before this can be stated with certainty.

6.3 Effect of relative penetration

Chapter 5.3 have shown that the horizontal pull-over force, axial force, curvature and global displacement increases with the relative penetration. The effect on the pull-over force varies greatly with the hit angle, ranging from a 41.6 % increase between a 13 mm and 133 mm relative penetration for a perpendicular case, to hindering the clump weight to cross altogether for a combination of $\delta_{pen} = 113$ mm and a 20° hit angle. The effect on the vertical pull-over force is relatively small, where the greatest increase is found to be 13 % for a change from $\delta_{pen} = 13$ mm to $\delta_{pen} = 63$ mm for a perpendicular hit angle.

The maximum axial force, displacement and curvature are found to consistently increase with the relative penetration regardless of the hit angle. The effect on the displacement is significant with a increase of up to 151 % between δ_{pen} =13 mm and δ_{pen} =113 mm for a 40° hit angle. The curvature experience an increase of up to 32.4 % by raising δ_{pen} from 13 mm to 113 mm for a 40 % hit angle. For a 20 % hit angle the increase from $\delta_{pen} = 63$ mm to $\delta_{pen} = 133$ mm raises

the resistance to the point were the clump weight is unable to cross and a 67 % increase in the curvature in the first 40 s after collision.

6.4 Effect of pre-tension

It has been shown in chapter 5.4 that the pretension have a small to no effect on the pull-over force for all hit angles. By decreasing the pre-tension from 10 kN to 1 kN one can observe up to a 1 % decrease in the horizontal pull-over force and up to a 2 % decrease in the vertical pull-over force. The maximum axial force is decreased by up to 7 % and maximum global displacement were raised by up to 4 % for a 40° hit angle. The most significant effect from the reduction of pre-tension were on the curvature for small hit angles, where one could observe a 9 % increase in the maximum curvature when the hit angle were set to 20°. The effect on the curvature were found to be significantly lower for larger hit angles, with only a 1 % increase for a perpendicular case.

6.5 Design check

The most critical axial forces and curvatures found for a combination of hit angle, relative penetration and pre-tension still enabling the clump weight to cross the power cable were 159 kN and 0.349 m^{-1} respectively. This corresponds to 8.4 % and 71.1 % of the design limits found for the axial force and curvature respectively, which means that the response is within safe bounds.

The largest maximum axial force and maximum curvature occurring for the cases where the clump weight is unable to cross were found to be 180 kN and 0.362 m^{-1} respectively. The maximum magnitude is slightly larger than for that of the most critical perpendicular hit angle, but the validity of the results are uncertain. Nevertheless, the response is still within the safe bounds specified by the rules during during the first 40 seconds after contact between the clump weight and cable has been established.

The sliding motion occurring for cases where low hit angles and large relative penetration are combined can also be critical for the outer sheath of the cable due to friction. As the contact point is concentrated at the edge of the roller barrel for low hit angles, it seem probable that the siding can damage the cable sheath if the edge is sharp. Preventive measures like rock dumping or burial will be necessary if it can be proven that the sliding threaten the integrity of the outer protective layer.

7 Further work

The lift force produced by the trawl boards is not modelled in the SIMLA model after T = 50.0 s, resulting in the trawl bags to close on impact. The effect will probably lead to conservative results as the drag force is more concentrated behind the clump weight. Nevertheless, the effect should be further studied especially for small hit angles where the pull-over phase duration is long.

Based on the result found in section 5.2, both the pull-over force and cable curvature seem to continuously increase over time if the clump weight is unable to cross the cable. Further work may include studying simulations where the clump weight slides along the cable over longer durations. Hopefully, one can with this determine if the clump weight eventually manage to cross the cable, or weather the maximum curvature continue to increase beyond the design limit.

The integrity of the cable sheath during sliding may be critical for the cable survival, and should be investigated. Weather the cable sheath can endure the scraping of the clump weight roller should be physically tested. If it can be proven that the cable is able to survive the sliding repeatedly for the number of occurrences that can be expected throughout its lifetime, there may not be necessary to take preventive actions like burial.

The bottom topography may have a significant impact the response of the cable, especially for the cases where the trawl gear is unable to cross. Irregularities from the bottom or other movement constraints can be sufficient to stop the sliding so that the clump weight may cross. The effect on soil types and the resulting contact damping in contact with the sea bottom may also be of interest for further study.

References

API (2014). *Specification for Unbonded Flexible Pipe; Fourth Edition; Effective Date: November 4, 2014*. URL: https://compass.astm.org/DIGITAL_LIBRARY/3PC/0b883834-cf6e-4cbd-ab22-2ac961bab35c.htm (visited on 06/08/2020).

Berg Johansen, Ingrid (2012). "Clump-weight trawl gear interaction with submarine pipelines". bibtex[referencetype=mastersthesis]. PhD thesis. NTNU.

DNV (2011). *DNV-RP-H103: Modelling and Analysis of Marine Operations*.

DNVGL (June 2016). *DNVGL-ST-0359: Subsea power cables for wind power plants*.

— (2017). *DNVGL-RP-F111: Interference Between Trawl Gear and Pipelines*.

Equinor (June 11, 2018). *Ser elektrifiseringsmuligheter på norsk sokkel*. Library Catalog: www.equinor.com. URL: https://www.equinor.com/no/news/11jun2018-electrification.html (visited on 04/20/2020).

— (Aug. 4, 2020a). *Hywind Tampen approved by Norwegian authorities*. Hywind Tampen approved by Norwegian authorities. Library Catalog: www.equinor.com. URL: https://www.equinor.com/en/news/2020-04-08-hywind-tampen-approved.html (visited on 04/20/2020).

— (2020b). *Renewables and low-carbon solutions in Equinor - equinor.com*. Library Catalog: www.equinor.com. URL: https://www.equinor.com/en/what-we-do/renewables.html (visited on 05/24/2020).

Fyrileiv, Olav, Dag O Askheim, Richard Verley, and Hanne Rolsdorph (Oct. 2, 2008). "Pipeline-Trawl Interaction: Effect of Trawl Clump Weights". In: 25th International Conference on Offshore Mechanics and Arctic Engineering. American Society of Mechanical Engineers Digital Collection, pp. 95–102. DOI: 10.1115/OMAE2006-92128. URL: https://asmedigitalcollection.asme.org/OMAE/proceedings/OMAE2006/47497/95/317409 (visited on 05/01/2020).

Georgios, Stamatiou (Sept. 2010). "Techno-Economical Analysis of DC Collection Grid Offshore Wind Parks". bibtex[referencetype=mastersthesis]. PhD thesis. UK: University of Nottingham.

Karlsen, Ludvig and Edel Simonsen (1989). *Redskapsteknologi i fiske*. Accession Number: 998940165804702202 Publication Title: Norbok Source: NO-OsNB Type: book. Oslo: Universitetsforlaget. 206 pp. ISBN: 978-82-00-43175-6. URL: https://urn.nb.no/URN:NBN:no-nb_digibok_2014061706127 (visited on 03/13/2020).

Krogstadmo, Truls Wanvik (2019). "Reduction of trawl impact loads on pipelines resting exposed on the seabed". bibtex[referencetype=mastersthesis]. PhD thesis. NTNU. URL: https://ntnuopen.ntnu.no/ntnu-xmlui/handle/11250/2622972 (visited on 12/16/2019).

Longva, Vegard (2010). "Simulation of Trawl Loads on Subsea Pipelines". Mastter Theis.

Longva, Vegard, Svein Sævik, Erik Levold, and Håvar Ilstad (Dec. 1, 2013). "Dynamic simulation of subsea pipeline and trawl board pull-over interaction". In: *Marine Structures* 34, pp. 156–184. ISSN: 0951-8339. DOI: 10.1016/j.marstruc.2013.09.004. URL: http://www.sciencedirect.com/science/article/pii/S0951833913000695.

Maaløø, Kristian (2011). "Clump-weight Trawl Gear Interaction with Submarine Pipelines". bibtex[referencetype=mastersthesis]. PhD thesis. NTNU.

Mathisen, Kjell Magne (1990). "Large displacement analysis of flexible and rigid systems considering displacement-dependent loads and nonlinear constraints". PhD thesis. NTNU.

Moan, Torgeir (Sept. 2003). *Finite Element Modelling and Analysis of Marine Structures*.

Møller, Martin Troels (2009). "Simulation of Interference between Trawl Gear and Pipelines". Master Theis.

Mountassir, Othmane El and Charlotte Strang-Moran (Sept. 2018). "Subsea Power Cable Trends". In: URL: https://www.researchgate.net/publication/332344488_Subsea_Power_Cable_Trends (visited on 04/20/2020).

Nations, United (Dec. 12, 2015). *The paris agreement*. URL: https://treaties.un.org/pages/ViewDetails.aspx?src=TREATY&mtdsg_no=XXVII-7-d&chapter=27&clang=_en.

Sævik, Svein (Feb. 2017a). *Lecture Notes in Offshore Pipeline Technology*.

— (Feb. 6, 2017b). *SIMLA - Theory Manual, 2017 edition*.

— (Apr. 18, 2019). *SIMLA Version 3.16.0 User Manual*.

Statnett (2014). *NorNed Submarine Cable*. Library Catalog: slideplayer.com. URL: https://slideplayer.com/slide/1633238/ (visited on 05/26/2020).

Worzyk, Thomas (2009). "Submarine Power Cables and Their Design Elements". In: *Submarine Power Cables: Design, Installation, Repair, Environmental Aspects*. Ed. by Thomas Worzyk. Power Systems. Berlin, Heidelberg: Springer, pp. 9–50. ISBN: 978-3-642-01270-9. DOI: 10.1007/978-3-642-01270-9_2. URL: https://doi.org/10.1007/978-3-642-01270-9_2 (visited on 05/26/2020).

Appendix A Overview of results

Hit angle	δ_{pen}	Pre-tension	Max. averaged horizontal pull-over force	Max. averaged vertical pull-over force	Max. axial force	Max. curvature	Max. displacement
90°	13 mm	10 kN	37.7 kN	- 37.2 kN	117 kN	0.275 m^{-1}	2.67 m
		1 kN	37.4 kN	- 37.0 kN	111 kN	0.272 m^{-1}	2.71 m
	63 mm	10 kN	49.3 kN	- 41.9 kN	147 kN	0.311 m^{-1}	4.22 m
		1 kN	48.9 kN	- 41.6 kN	141 kN	0.314 m^{-1}	4.29 m
	113 mm	10 kN	53.4 kN	-40.4 kN	159 kN	0.323 m^{-1}	4.89 m
		1 kN	54.2 kN	-40.3 kN	153 kN	0.323 m^{-1}	4.97 m
80°	13 mm	10 kN	32.1 kN	- 27.3 kN	80.2 kN	0.287 m^{-1}	1.39 m
		1 kN	28.0 kN	- 26.9 kN	77.6 kN	0.302 m^{-1}	1.42 m
	63 mm	10 kN	32.2 kN	- 28.4 kN	102 kN	0.299 m^{-1}	2.09 m
		1 kN	30.9 kN	- 28.8 kN	97.6 kN	0.303 m^{-1}	2.13 m
	113 mm	10 kN	69.6 kN	- 40.4 kN	113 kN	0.325 m^{-1}	2.41 m
		1 kN	46.7 kN	- 27.5 kN	109 kN	0.352 m^{-1}	2.54 m
40°	13 mm	10 kN	12.8 kN	- 28.0 kN	60.6 kN	0.207 m^{-1}	0.70 m
		1 kN	12.6 kN	- 28.0 kN	55.9 kN	0.214 m^{-1}	0.74 m
	63 mm	10 kN	20.0 kN	- 30.7 kN	80.5 kN	0.235 m^{-1}	1.35 m
		1 kN	15.3 kN	- 28.5 kN	75.1 kN	0.245 m^{-1}	1.40 m
	113 mm	10 kN	15.3 kN	- 28.7 kN	93.3 kN	0.274 m^{-1}	1.76 m
		1 kN	20.0 kN	- 30.6 kN	109 kN	0.284 m^{-1}	1.82 m
20°	13 mm	10 kN	15.5 kN	- 26.0 kN	86.5 kN	0.211 m^{-1}	0.89 m
		1 kN	15.5 kN	- 26.1 kN	81.9 kN	0.211 m^{-1}	0.93 m
	63 mm	10 kN	18.6 kN	- 32.3 kN	105 kN	0.230 m^{-1}	1.21 m
		1 kN	18.4 kN	- 31.7 kN	101 kN	0.250 m^{-1}	1.25 m
	113 mm	10 kN	32.1 kN	- 11.7 kN	155 kN	0.325 m^{-1}	3.02 m
		1 kN	32.0 kN	- 11.7 kN	180 kN	0.361 m^{-1}	3.09 m

Appendix B Simulation screenshots

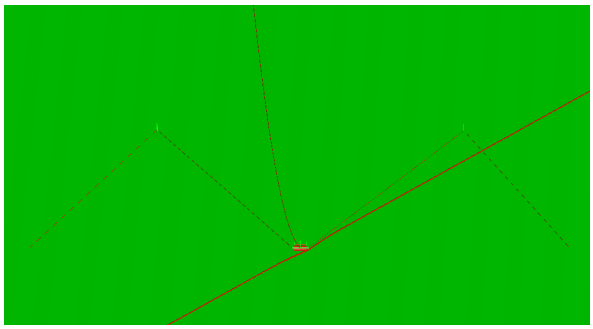

(a) T = 61.6 s

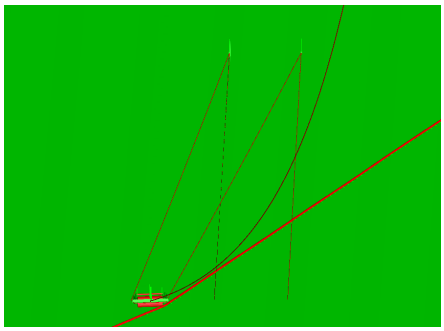

(b) T = 100 s

Figure B.1: 20° hit angle, δ_{pen} = 113 mm, and 1 kN pre-tension

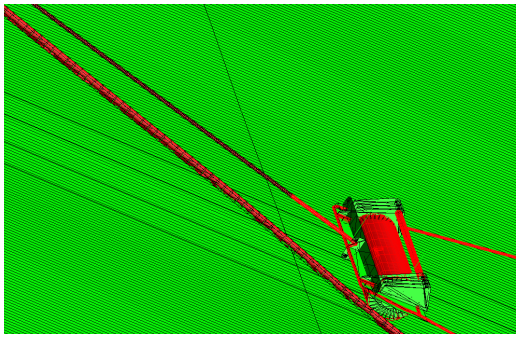

(a) T = 61.5 s

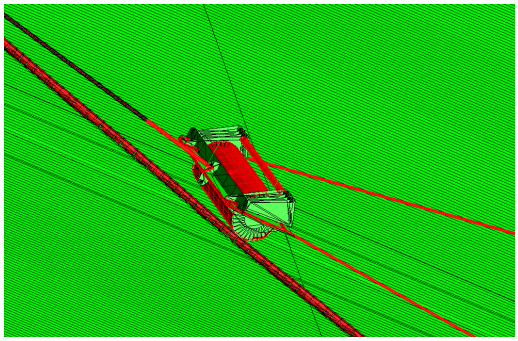

(b) T = 62.5 s

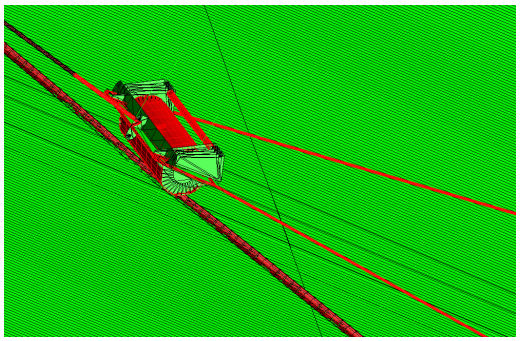

(c) T = 63.0 s

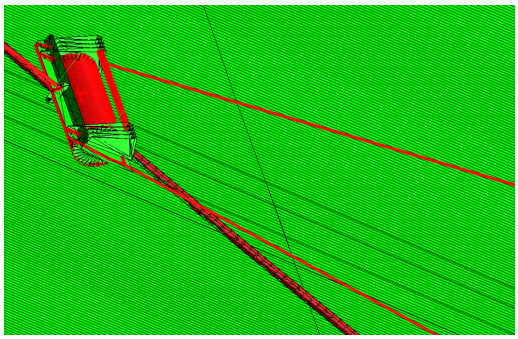

(d) T = 63.5 s

Figure B.2: 40° hit angle, δ_{pen} = 113 mm, and 1 kN pre-tension

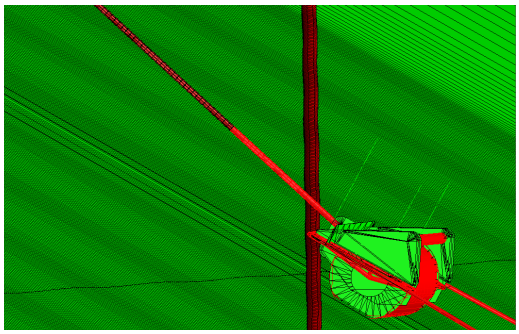

(a) T = 62.0 s

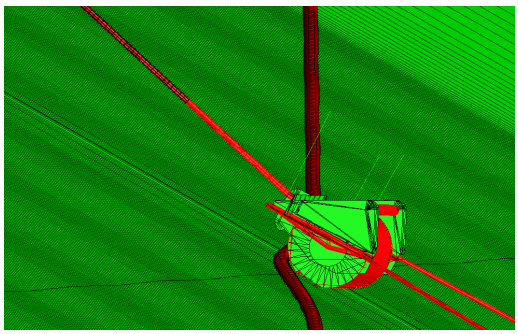

(b) T = 62.5 s

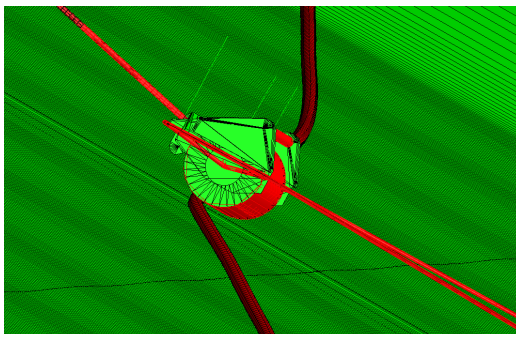

(c) T = 63.0 s

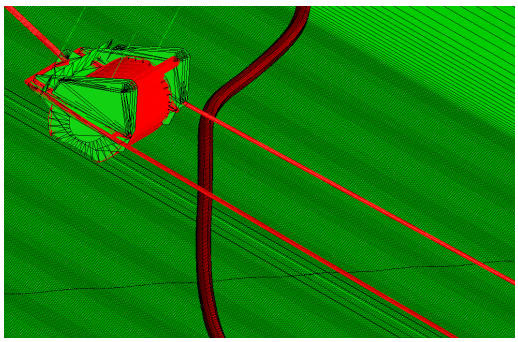

(d) T = 63.5 s

Figure B.3: 80° hit angle, δ_{pen} = 113 mm, and 1 kN pre-tension

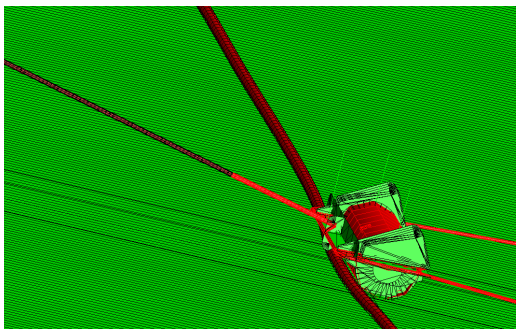

(a) T = 62.0 s

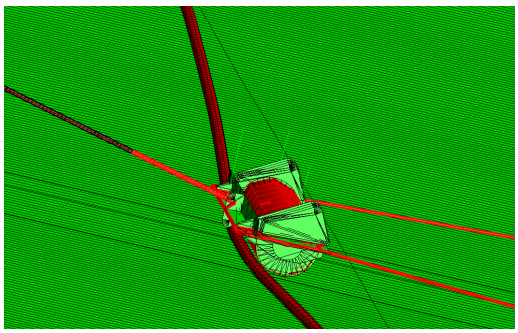

(b) T = 62.5 s

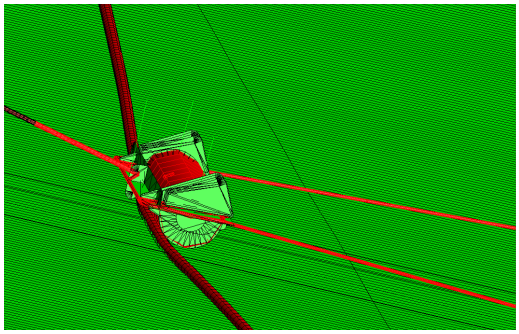

(c) T = 63.0 s

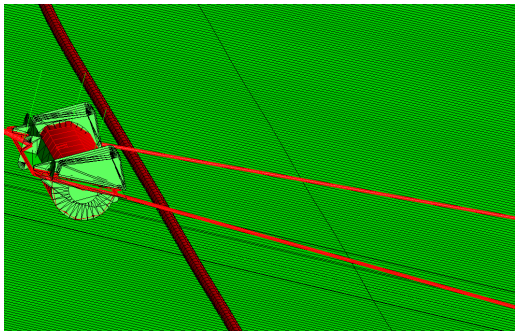

(d) T = 63.5 s

Figure B.4: 90° hit angle, δ_{pen} = 113 mm, and 1 kN pre-tension

NTNU

Norwegian University of
Science and Technology